

Metalloproteins: Structure Determination (HADH), Inhibition (P4H), and
Biomimetic Systems (P-1[Ru(NO)(Cl)])

By

Timothy M. Reed

Submitted to the Department of Chemistry and the Faculty of the Graduate
School of the University of Kansas in partial fulfillment of the requirements for
the degree of Doctor of Philosophy.

Committee Members*

Dr. Minae Mure
Chairperson

Dr. Andrew Borovik *

Dr. Paul Hanson *

Dr. Richard Schowen *

Dr. Emily Scott *

Date defended: Dec. 8th 2008

The Dissertation Committee for Timothy M. Reed certifies that this is the approved version of the following dissertation

Metalloproteins: Structure Determination (HADH), Inhibition (P4H), and Biomimetic Systems (P-1[Ru(NO)(Cl)])

Dissertation Committee:

Dr. Minae Mure
Chairperson

Committee Members*

Dr. Andrew Borovik *

Dr. Paul Hanson *

Dr. Richard Schowen *

Dr. Emily Scott *

Date defended: Dec. 8th 2008

Abstract

Timothy Michael Reed

Department of Chemistry, University of Kansas

Histamine dehydrogenase from *Nocardioides simplex* (HADH) is a flavoprotein that converts histamine to imidazole acetaldehyde and is highly specific for histamine. Chapter one describes the development of overexpression and purification a recombinant form of HADH (rHADH) and its basic biochemical characterization. Chapter two describes X-ray structure determination of rHADH. Diffraction data were collected to 2.7 Å resolution with 99.7% completeness. The histamine binding motif of HADH are very similar to those in the other histamine binding proteins.

Prolyl-4-hydroxylase (P4H) belongs to a family of α ketoglutarate-dependent non-heme iron oxygenases. Selective inhibitors of P4H can be potential therapeutics for fibrosis. Chapter three discusses the design of inhibitors that target P4H in the ER using the signal peptide KDEL, which is specific to the ER. Phenanthroline-GKDEL demonstrates a 100-fold increase in potency in inhibiting P4H produced in the cultured human fibroblast cells versus isolated enzyme. Fluorescent microscopy using a fluorescently tagged inhibitor demonstrates uptake of the phen-E(EDANS)VKDEL inhibitor into the ER.

Nitric oxide (NO) is an important signaling molecule in the body, and the site-specific timed release NO could be utilized in the treatment of various medical conditions. Chapter four discusses the photorelease of NO from a ruthenium salen complex immobilized within a porous material. This material transfers NO to myoglobin within 20 minutes. NO is released from this material in the presence of light; however, during periods of darkness, the release of NO was not observed. This is the first system where NO is photoreleased from an immobilized polymer support.

Acknowledgements

In the time that I have spent at KU and in my journey through graduate school, I have many people to thank. I would first like to thank my family who are so proud of me and have supported my work from the beginning. My parents have made numerous trips up to Lawrence to visit me and help me. Either moving me around or just walking up and down Mass Street, they were there for me. My brother, who I would visit in Tulsa or he would come up and visit me in Lawrence, we would always have a great time together. I am very proud of the man that he is becoming. I always enjoyed talking with my sister. She had a great way of making me smile and laugh. I love my family very much and appreciate all their help and support. I would also like to thank the 20s30s group of Grace EPC. They were my home away from home. I remember numerous holidays and weekend activities with them. They were always supportive and constantly praying for me. Their encouragement and wisdom would always help comfort me whenever I needed it.

I would also like to thank the individuals that helped train and develop my skills as a scientist. I was always appreciative of Dr. Limburg and the training and respect he gave me as a scientist. As a fourth year student, he gave me the freedom and respect usually given to post-doctoral students. His mentorship and guidance gave me the confidence and preparation I need to begin the next phase of my life. He was always willing to discuss results and made sure that I was prepared for anything that came my way. Dr. Limburg and Dr. Mure also formed my interest for chemical biology, which is the field of my new position. I would also like to thank Dr. Mure for all of her help and guidance through the HADH project. Discussion included all three of us discussing the implications of recent data. She also worked very hard on editing my dissertation and making sure that I was ready for my defense. I would also like to thank Andy for his training and guidance in my first few years of graduate school. I always admired his emphasis on good science and good presentation of one's science. His words of wisdom also ring in my ear. I remember times when I hear Andy's voice "the worst experiment you can do is not to do it at all" right before a big experiment. I thank all of my advisors for the training and preparation they gave me for the continuation of my scientific career, whatever it may be.

In my x-ray crystallography collaboration, I would like to thank Dr. Scott and all her hard work in solving the crystal structure of HADH. Her time, dedication, and sacrifice meant a lot for me. Dr. Schowen also demonstrated the same character by helping me with my P4H chapter and my slide presentation. I learned a great deal of science from them. I would also like to thank Dr. Hanson for his time and commitment to my defense committee.

The group members of all three labs were an incredible support. I made some great friends, who I wish the best in their career as they leave graduate school.

Table of Contents

	page
Abstract	iii
Acknowledgements	iv
List of Figures	vii
List of Schemes	xii
List of Tables	xiii
List of Equations	xiv
List of Abbreviation	xv
Chapter 1	
Introduction	1
Expression, Purification and Characterization of Histamine Dehydrogenase	2
Materials and Methods	47
Results	51
Discussion	59
Conclusion	61
Chapter 2	
Crystal Structure Determination of Histamine Dehydrogenase from <i>Nocardioides Simplex</i>	67
Materials and Methods	69
Results	71
Discussion	96
Conclusion	116

Chapter 3	Targeting the Endoplasmic Reticulum for Inhibition of Collagen Production by Prolyl 4-Hydroxylase	121
	Materials and Methods	142
	Results	155
	Discussion	172
	Conclusion	176
Chapter 4	Photolytic Release of Nitric Oxide from an Immobilized Ruthenium Complex	181
	Materials and Methods	191
	Results and Discussion	195
	Conclusion	202
Conclusion		206
Appendix		210

List of Figures

	page
Figure 1.1. Biogenic amines and polyamines	3
Figure 1.2. Structures of A) 6-S-Cysteinyl-flavin mononucleotide and B) [4Fe-4S] iron sulfur cluster found in TMADH, DMADH, and HADH	6
Figure 1.3. Sequence Alignment of HADH and TMADH	7
Figure 1.4. UV/Vis Spectrum of oxidized and reduced forms of A) HADH and B) TMADH	8
Figure 1.5. EPR Spectrum of A) HADH and B) TMADH	9
Figure 1.6. The plot of pH dependence on k_{cat}/K_m and k_{cat} for the oxidation of histamine by HADH.	12
Figure 1.7. Possible mechanism for C-H bond cleavage in flavoproteins A) polar nucleophilic attack B) electron transfer C) hydride transfer	16
Figure 1.8. TMADH aromatic bowl	31
Figure 1.9. Basic residues in TMADH that may contribute to the observed ionization	31
Figure 1.10. Proposed mechanism for TMADH for 0/2 and 1/3 cycle	46
Figure 1.11. Sequence Alignment of native-HADH with rHADH	55
Figure 1.12. Optimization of HADH expression in Terrific Broth.	56
Figure 1.13. SDS-PAGE showing each stage of purification A) DEAE B) Butyl-Sepharose C) Size exclusion chromatography	56

Figure 1.14. UV/Vis spectra of fractions collected after A) DEAE B) butyl-Sepharose C) size exclusion column.	57
Figure 1.15. HADH coupled Assay with histamine	59
Figure 2.1. Screening hits for Emerald Biosciences Crystal Kit #1	73
Figure 2.2. Homemade solution of Emerald Biosciences Crystal Kit	73
Figure 2.3. Hampton Research Crystal Screen Kit 1 #39	74
Figure 2.4. Hampton Research Crystal Screen Kit 1 #39	76
Figure 2.5. Mass spectrum (MALDI-TOF) of A) unsubstituted rHADH and B) SeMet incorporated rHADH.	78
Figure 2.6. Mass spectra (MALDI-TOF) of A) unsubstituted rHADH B) SeMet incorporated rHADH.	79
Figure 2.7. X-ray diffraction pattern of SeMet-rHADH at SSRL	81
Figure 2.8. Overview of rHADH structure.	84
Figure 2.9. Individual domains of each subunit in rHADH.	85
Figure 2.10. HADH large domain rainbow colored demonstrating the TIM barrel	87
Figure 2.11. HADH subunit overlaid with TMADH.	89
Figure 2.12. The prosthetic groups, 6-S-Cys-FMN and [4Fe-4S], in HADH are involved in the oxidation of histamine	91
Figure 2.13. Butterfly bend structure of 6-S-Cys-FMN.	93
Figure 2.14. Putative histamine binding site in rHADH.	95
Figure 2.15. Model study on histamine binding in the active site of rHADH.	96
Figure 2.16. Data collection of HADH crystal hanging out of the loop	100

Figure 2.17. The spatial arrangement of Arginine in HADH and TMADH suggests similar mechanism of 6-S-Cys-FMN biogenesis	103
Figure 2.18. Conserved Tyr in the Active Site Contributes to the Spin-interaction States of HADH and TMADH	105
Figure 2.19. Proposed Oxidation of Histamine by HADH	111
Figure 2.20. Proposed Electron Transfer of HADH	114
Figure 3.1. Damage to the tissue elicits a cascade immune response	123
Figure 3.2. Proposed catalytic cycle of human type I prolyl 4-hydroxylase	127
Figure 3.3. Mechanism of retrieval of the KDEL-signal peptide secreted proteins is the binding of the tetrapeptide sequence to the KDEL receptor located in the Golgi apparatus	136
Figure 3.4. Structure of Inhibitors A) Phen-2-GKDEL B)Phen-2-E(EDANS)VKDEL	157
Figure 3.5. Dipsi spectrum of phen-2-GKDEL on Bruker 500 MHz NMR	158
Figure 3.6. Dipsi spectrum of phen-2-E(EDANS)VKDEL on Bruker 500 MHz NMR	159
Figure 3.7. Fluorescence imaging of HFF incubated with A) phen-E(EDANS)VKDEL B) ER tracker.	161
Figure 3.8. Co-localization and intensity correlation analysis of A) phen-E(EDANS)VKDEL and B) ER Tracker	163
Figure 3.9. IC ₅₀ curve of phen-GKDE inhibition of the recombinant human-P4H.	164
Figure 3.10. Collagen production by HFF cells with no inhibitor (red boxes) and phen-GKDEL (green diamonds).	166

Figure 3.11. The chemical structure of the dye that covalently links to collagen types I through V in the Sircol Assay.	167
Figure 3.12. Sircol assay of pepsin digested collagen from HFF cells.	168
Figure 3.13. IC ₅₀ curve of phen-2-GKDEL (green diamonds) with pepsin digested collagen.	168
Figure 3.14. IC ₅₀ curve of inhibition of recombinant human-P4H with phen.	169
Figure 3.15. Inhibition of collagen with 0.2 mM phen-GKDEL (green diamonds), 0.2 mM phen (blue circles), and no inhibitor control (red boxes).	171
Figure 3.16. IC ₅₀ curve of phen (blue circles) and phen-GKDEL (green diamonds) with pepsin digested collagen.	172
Figure 3.17. phen-5-GKDEL inhibitor, with the phenanthroline couple to the N terminus at the 5 position	176
Figure 4.1. NO donors drugs approved for medical use	182
Figure 4.2. Structures and time release of selective diazeniumdiolates	184
Figure 4.3. Photochemical release of NO from ruthenium salen complex	187
Figure 4.4. The process of template copolymerization	189
Figure 4.5. The storage and release of NO from P-1[Co ^{II}].	190
Figure 4.6. EPR spectra (77K) for P-1[Ru(NO)(Cl)] (dashed line) and P-1[Ru ^{III} 1(Cl)] (solid line).	198
Figure 4.7. Mb peak at 435 nm shifts to 420 nm upon the binding of NO from P-1 [Ru(NO)(Cl)]. Mb concentration 3.0 mM in 50 mM phosphate buffer, pH 7.2.	199

Figure 4.8. Time release curve of P-1[Ru(NO)(Cl) with continuous release (black dots) and stop time release (red dots). Stop time release is demonstrated with continuous irradiation (solid line) and no irradiation (dashed line).	200
Figure 4.9. Detection of NO through nitrite concentration by the Griess Reaction	201
Figure A.1. Dose dependent indirect ELISA detecting collagen production with a concentration range of 100 mM to 0.01 mM in the presence of phen (blue circles) and in the presence of phen-GKDEL (green diamonds)	210
Figure A.2. Dose dependent indirect ELISA of collagen production with a concentration range of 100 mM to 0.01 mM for phen (blue circles) and phen-2-GKDEL (green diamonds)	211

List of Schemes

	page
Scheme 1.1. Proposed mechanism of HADH under single reaction	8
Scheme 1.2 Proposed mechanism for formation of 6-OH-FMN (R2 = hydroxyl) or 6-S-cysteinyl FMN (R2=cysteine)	28
Scheme 1.3. Control of rate of reduction of FMN by protonation of substrate	34
Scheme 1.4. Proposed oxidation reaction mechanism for TMADH.	36
Scheme 3.1. The solid phase synthesis of the GKDEL retention signal	153
Scheme 4.1. Synthesis of [Ru ¹ (NO)(Cl)], P- 1 [Ru(NO)(Cl)], and P- 1 [Ru(Cl)]. AIBN = azobisisobutyronitrile, DCB = 1,2- dichlorobenzene	193

List of Tables

	Page
Table 1.1. Substrate specificity of HADH	11
Table 1.2. Redox potentials of the cofactor	19
Table 1.3. rHADH and native HADH comparison	58
Table 2.1. X-ray data collection statistics for SeMet-rHADH. Values in parentheses are for the last shell	80
Table 2.2. Refinement Statistics	82
Table 3.1. The deleterious effects of fibrosis on human population	121
Table 3.2. IC ₅₀ values for the inhibition of P4H by N-oxalylglycine and its derivatives against isolated P4H enzyme and in vitro with chick-tendon cells	129
Table 3.3. Inhibition of avian P4H by pyridine-2,5-dicarboxylate and its derivatives.	131
Table 3.4. Inhibition of isolated P4H and HFF cells by phenanthroline derivatives.	134
Table 3.5. Quantitative analysis of the co-localization of ER tracker Red and phen-2-E(EDANS)VKDEL as performed with Image J plugin JACoP	162

List of Equations

	page
Equation 1.1. HADH oxidative deamination of histamine to imidazole acetaldehyde	7
Equation 3.1. Pearson's coefficient	148
Equation 3.2. Overlap coefficient	148
Equation 3.3. k_1 and k_2 coefficients	148
Equation 3.4. M_1 & M_2 coefficient	148
Equation 3.5. IC_{50} curve	151

List of Abbreviations

AIBN	azodiisobutyronitrile
DMA	Dimethylamine
DMADH	Dimethylamine Dehydrogenase
EB	Emerald Biosciences
EGF	Epidermal growth factor
ELISA	Enzyme Linked ImmunoSorbent Assay
ER	Endoplasmic Reticulum
ETF	Electron Transferring Flavoprotein
FMN	Flavin Mononucleotide
HADH	Histamine Dehydrogenase
HBP	Histamine Binding Protein
HFF	Human fibroblast cells
HR	Hampton Research
Hyp	Hydroxylproline
IL6	Interleukin-6
KDEL	human retention signal peptide for the ER consists of four amino acids, lysine, aspartic acid, glutamic acid, and leucine
L1	Interleukin-1
MADH	Methylamine Dehydrogenase
NLS	Nuclear localization signals
NO	Nitric Oxide
NONOates	Diazeniumdiolates
NOS	Nitric Oxide Synthase
P4H	prolyl 4-hydroxylase
PDGF	Platelet-derived growth factor
PDI	protein disulfide isomerase
Phen	1,10 phenanthroline
Phen-2-GKDEL	1,10 Phenanthroline-2-Glycine-Lysine-Aspartic Acid-Glutamic-Acid-Leucine
Phen-2-E(EDANS)VKDEL	1,10 Phenanthroline-2-Glutamic acid - γ - [2 - (1 - sulfonyl - 5 - naphthyl) - aminoethylamide]-Valine-Lysine-Aspartic Acid-Glutamic-Acid-Leucine
SeMet	Selenium Methionine
TGF- β	Transforming growth factor beta
TMA	Trimethylamine
TMADH	Trimethylamine Dehydrogenase
TNF- α	Tumor necrosis factor alpha
TGN	trans-Golgi network
SNP	Sodium Nitroprusside
H ₂ 1	Bis[2-hydroxy-4-(4-vinylbenzyloxy)benzaldehyde]ethylenediimine

Chapter 1

Introduction

Metalloproteins are proteins with cofactors that involve a metal center and are involved various important roles in biological system.¹ The list of roles and functions of metalloproteins is exhaustive but includes the following: oxygen transport (iron-hemoglobin),² the reduction and oxidation of toxic radical species (manganese-superoxide dismutase),³ or stereospecific reactions (cobalt-glutamate mutase).⁴ Understanding the structure and function of these metalloproteins often begins with the x-ray crystallographic structure of the enzyme. There are close to 44,000 protein x-ray crystallographic structures in the Protein Data Bank.⁵ The 3-D crystal structures provide information about the metalloprotein's active site, including important metal-coordinating residues, location, and void space. Metalloproteins are also important targets for drug design due to their importance in biological processes. The design of inhibitors that chelate of metal centers in metalloproteins could be used for various illness including cancer, arthritis, and fibrosis.⁶⁻⁸ The study and understanding of the structure and function of metalloproteins provides inspiration into design of materials and devices.⁹ Metalloproteins found in nature contain ideal chemical properties such as sight isolation, stereospecific reactions, formation of highly reactive species, and catalyzed reactions all at ambient temperature and

pressure. Scientist and engineers look to these processes to improve systems and provide inspiration towards the new design of materials and devices.

Expression, Purification and Characterization of Histamine Dehydrogenase

1.1. Background

1.1.1. Physiological Importance of Histamine

Histamine is an important biogenic amine (Figure 1.1) that performs various physiological roles in allergic reaction, cell proliferation and as a neurotransmitter.¹⁰ Histamine is stored in the granules of mast cells, which are located near the nose, mouth, and blood vessels and function in the immune response at potential sites of injury.^{2,3} Histamine is also located in the histaminergic neurons within the brain, where it functions as a neurotransmitter.¹¹ In the stomach, histamine regulates the release of gastric acid, which is stored in enterochromaffin-like cells.¹² Between regulating the immune response and stomach acid secretion, the roles histamine plays in the body are vital for homeostasis. The physiological binding of histamine within the human histamine receptors continues to gain understanding.¹³⁻¹⁵ The structures of human histamine receptors have not yet been determined.

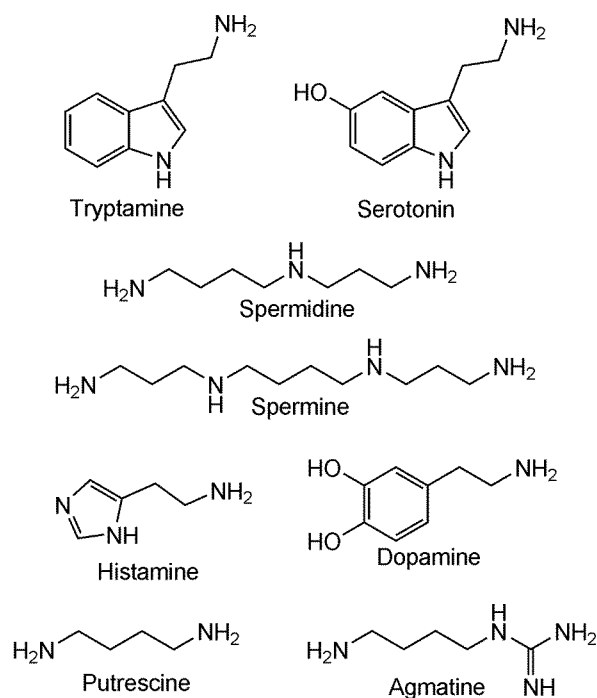


Figure 1.1. Biogenic amines and polyamines¹⁰

In the absence of this information, histamine binding proteins, which are selective towards histamine as a substrate provide an understanding of the physiological binding of histamine.¹⁶ Elevated histamine levels in humans have been linked to several deleterious conditions, including gastric disorders, mastocytosis, and cancer.¹⁰ The high levels of histamine that accumulate in fish as it begins to spoil cause scombroid food poisoning, leading to symptoms of headache and diarrhea.¹⁷ The development of a histamine sensor has been sought-after for food-safety regulations as well as understanding histamine's role in cancer.¹⁸⁻²⁰

1.1.2. Histamine Dehydrogenase Background

Histamine dehydrogenase (HADH) was first discovered by the Yorifuji group by screening the extracts of bacteria grown on histamine as a sole nitrogen source.²¹ The extract of a soil bacterium, *Nocardioides Simplex*, was able to metabolize histamine. Subsequently, the enzyme was isolated and annotated as HADH. HADH is a homodimer, where each subunit was found to be 84 KDa. Early studies suggested a narrow range of substrate selectivity. In addition to histamine, only putrescine was oxidized by HADH.²² HADH was originally thought to contain the tryptophan tryptophyl (TTQ) cofactor found in methylamine dehydrogenase²² because of the similarity in the UV/vis absorbance spectrum and the positive staining in the quinone-dependent redox cycling.²²

There are two major families of amine-oxidizing enzymes: quinoproteins¹³⁻¹⁵ and flavoproteins.²³ Quinoproteins are a class of enzymes that contain covalently-linked quinones as their cofactors, derived either from a tyrosine or tryptophan residue.^{14,16-18} Interestingly, amine oxidases (copper amine oxidases and lysyl oxidases) contain tyrosine-derived quinone cofactors and amine dehydrogenases (methylamine dehydrogenase, aromatic amine dehydrogenase, butylamine dehydrogenase) contain tryptophan-derived quinone cofactors. Flavoproteins are subdivided into oxidases or dehydrogenases and contain flavin adenine dinucleotide (FAD) or flavin mononucleotide (FMN) as redox active cofactors.²³ FAD-dependent

monoamine oxidase, is vital in the metabolism of the neurotransmitters serotonin, dopamine and norepinephrine.^{19,20} Trimethylamine dehydrogenase (TMADH)²¹ catalyzes the demethylation of trimethylamine to formaldehyde and dimethylamine. FMN-dependent dehydrogenases are trimethylamine dehydrogenase (TMADH) and dimethylamine dehydrogenase (DMADH) where the C6-isoalloxazine ring of the 6-S-Cys-FMN is crosslinked through the thioether bond of a Cys residue.^{7,12} These enzymes also have an [4Fe-4S] cluster, which is involved in the redox active cycle by transporting electrons (Figure 1.2).^{7,12} Limburg et al. further characterized the biochemical properties of HADH in order to define whether HADH is a TTQ-dependent amine dehydrogenase.²⁴

Limburg et al. cloned the 2.1 kb gene coding the full-length HADH from the genomic DNA of *N. simplex*.²⁴ A BLAST search uncovered sequence identity with several flavoproteins such as trimethylamine dehydrogenase (TMADH) (40% identity, 56% similarity) and dimethylamine dehydrogenase (DMADH) (37% identity and 51% similarity).²⁴ The crystal structure of TMADH has been determined to 2.2 Å, and it is known to contain the redox active cofactors 6-S-Cys-FMN (6-S-Cys-FMN) and an [4Fe-4S] cluster.²² Sequence analysis revealed the Cys residue in TMADH involved in the covalent cross-link of FMN to yield 6-S-Cys-FMN is conserved in HADH (Figure 1.3).²⁴ HADH also has the C(2X)C(2X)C(11-12X)C motif that is

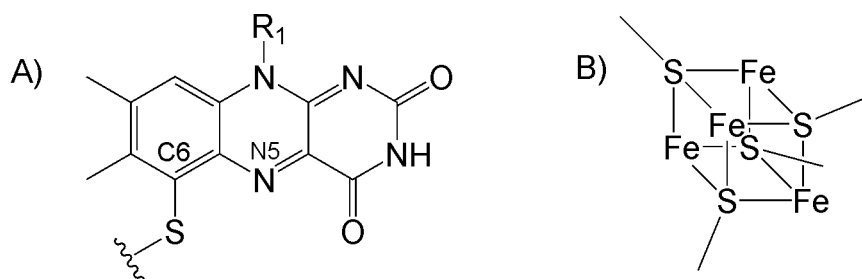
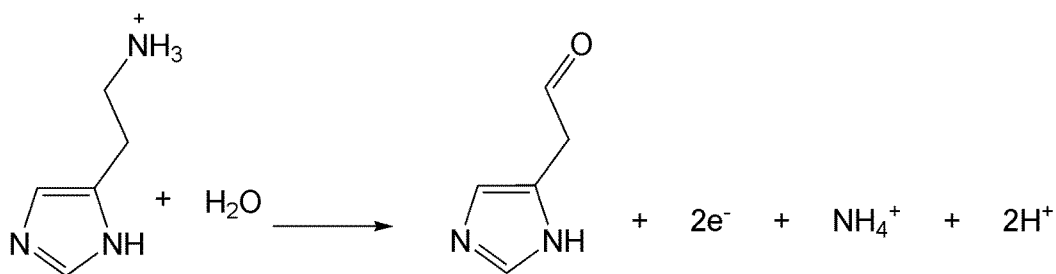


Figure 1.2. Structures of A) 6-S-Cysteinyl-flavin mononucleotide and B) [4Fe-4S] iron sulfur cluster found in TMADH, DMADH, and HADH^{7,12}

characteristic of proteins with an [4Fe-4S]. In this motif, 2X and 11-12X represent residues in between the cysteines that are coordinated to the iron-sulfur cluster.²⁴ These results strongly suggest that HADH belongs to the same family as TMADH with 6-S-Cys-FMN and an [4Fe-4S] cluster as the redox-active cofactors.²⁴

HADH catalyzes the oxidative deamination of histamine to imidazole acetaldehyde (Equation 1.1). Reduction of HADH occurs with addition of excess histamine, and the enzyme undergoes single turnover (Scheme 1.1).²⁴ Histamine binds to the active site and reacts with 6-S-Cys-FMN. Histamine is oxidized to imidazole acetaldehyde concomitant with the 2e⁻-reduction of 6-S-Cys-FMN(6-S-Cys-FMN_R). After another molecule of histamine binds to the active site, the disproportionation reaction between the 6-S-Cys-FMN_R and [Fe₄-S₄] cluster occurs to produce the semiquinone form of 6-S-Cys-FMN and one electron reduced [Fe₄-S₄]. The semiquinone of 6-S-Cys-FMN in HADH shows a UV/Vis spectrum with an absorbance maximum at 362 nm (Figure 1.4). TMADH undergoes the same reaction under single turnover



Equation 1.1.

Conserved cysteine crosslinks with FMN \rightarrow 6-S-cysteinyl FMN

HADH	FYQVP <u>H</u> CNGMGYR
TMADH	FYQVP <u>H</u> CIGAGSD

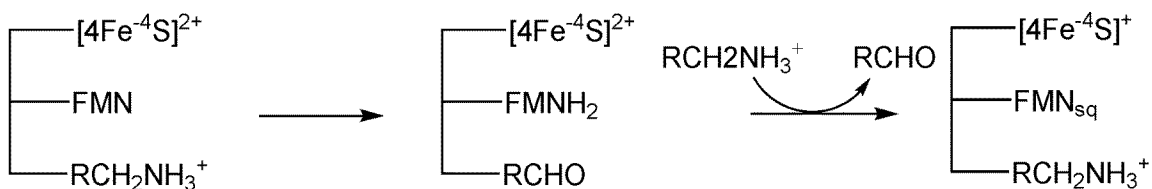
Four conserved cysteines are ligands to [4Fe-4S]

HADH	RE <u>C</u> IG <u>C</u> NI <u>C</u> VS-GDLTMSPIR <u>C</u> TQNPS
TMADH	RV <u>C</u> IG <u>C</u> NV <u>C</u> ISRWEIGGPPMI <u>C</u> TQNAT

Figure 1.3. Sequence Alignment of HADH and TMADH²⁴

conditions, with the flavin semiquinone absorbance at 366 nm.^{23,24}

Comparison of the UV/Vis spectra of HADH_{ox} and HADH_{red}, with TMADH_{ox} and TMADH_{red} reveals almost identical spectral characteristics.²⁴



Scheme 1.1. Proposed reaction mechanism of HADH under single reaction. Once substrate binds there is disproportionation between 6-S-Cys-FMNH₂ and [4Fe-4S]²⁺ with the flavin oxidized to the semiquinone and the [4Fe-4S]²⁺ in the +1 state²⁴

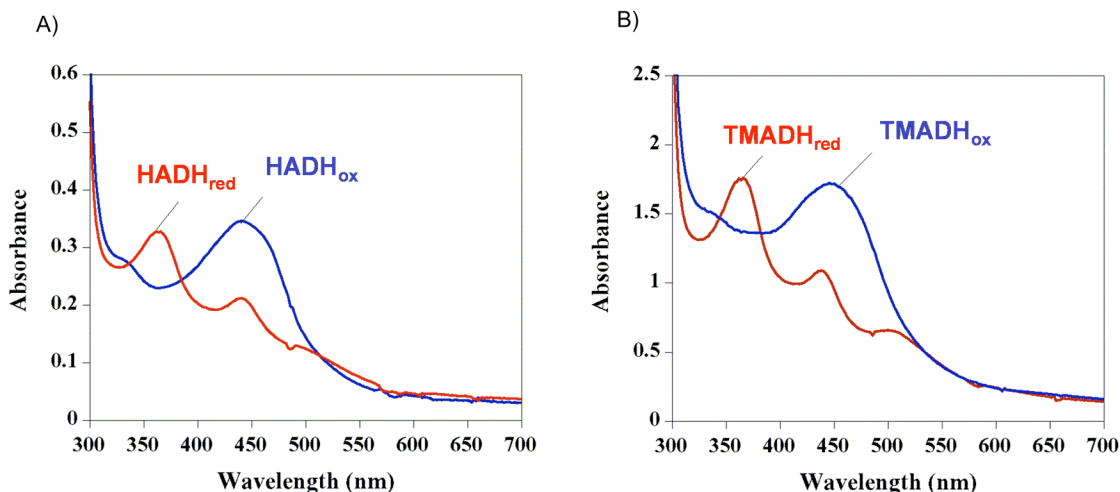


Figure 1.4. UV/Vis Spectrum of oxidized and reduced forms of A) HADH and B) TMADH²⁴

The EPR spectra of the unpaired electrons on the [4Fe-4S] cluster and the semiquinone of both enzymes gave further evidence of the similarities in redox active cofactors (Figure 1.5).²⁴ The electrons on the semiquinone and [4Fe-4S]⁺ couple antiferromagnetically, which causes strong, specific EPR features. HADH_{red} has an EPR signal at $g = 2.00$ and features at $g = 2.15$ and 1.88 (Figure 1.5A).²⁴ This $g = 2.00$ was believed to arise from the radical

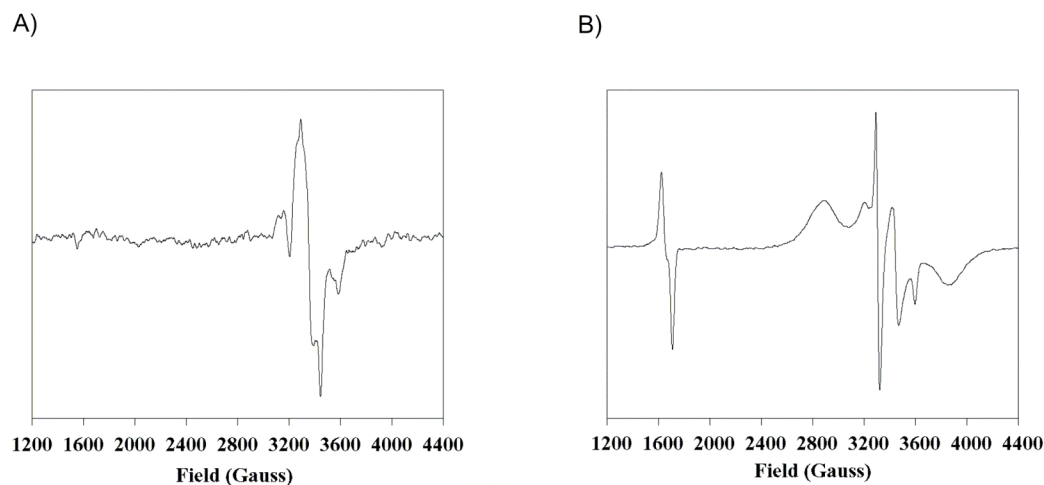


Figure 1.5. EPR Spectrum of A) reduced HADH and B) reduced TMADH²⁴

on the semiquinone, while the electron on the $[4\text{Fe-4S}]^+$ demonstrates features at $g = 2.15$, $g = 2.00$, and $g = 1.88$. TMADH_{red} also has a strong EPR signal, with the semiquinone and $[4\text{Fe-4S}]^+$ peaks at similar values (Figure 1.5B).^{7,25} Unlike HADH_{red}, TMADH_{red} gives a half-field signal, which is due to the coupling of electrons on the $[4\text{Fe-4S}]^+$ and the 6-S-Cys-FMN semiquinone. The EPR spectrum for HADH_{red} does not contain a half-field signal, which suggests that environment of the two cofactors might be different.²⁴ The spatial position of the cofactors or the arrangement of amino acids around the cofactors could affect the spin coupling of the electrons.²⁴ This could affect the coupling of the two unpaired electrons, as the distance between the two electrons in HADH may be too far for spin-spin interactions. Overall, comparison of the sequence analysis and spectroscopic data

demonstrates similarities between TMADH and HADH, again supporting the presence of the 6-S-Cys-FMN and iron-sulfur containing active site, but with possible difference in environment between the two redox sites.²⁴

1.1.3. Substrate Specificity of HADH

HADH is only able to oxidize a narrow range of amines, as demonstrated in Table 1.1.⁷ HADH does not oxidize trimethylamine (TMA) or dimethylamine (DMA), even with the high sequence identity of HADH with TMADH and DMADH. The biogenic amines dopamine and tyramine are also not substrates for HADH. The products of amino acid metabolism (histamine, agmatine, and putrescine) are all substrates, with histamine demonstrating the highest catalytic efficiency [$k_{\text{cat}}/K_{\text{m}}=2.1 (\pm 0.4) \times 10^5 \text{ M}^{-1} \text{ s}^{-1}$] and lowest K_{m} value ($31 \pm 11 \text{ }\mu\text{M}$). HADH demonstrates substrate inhibition at high concentrations of histamine or agmatine. As will be discussed further in the text, the substrate inhibition is thought to arise from a stable complexation of substrate with 6-S-Cys-FMN_{sq}-[4Fe-4S]⁺, analogous that observed in TMADH.²⁵ The selectivity of HADH for histamine provides evidence for its potential use in a histamine biosensor.

1.1.4. pH Effect on $k_{\text{cat}}/K_{\text{m}}$ and k_{cat}

Limburg et al. determined the pH dependence of $k_{\text{cat}}/K_{\text{m}}$ and k_{cat} .²⁴ The graph of $k_{\text{cat}}/K_{\text{m}}$ vs. pH was best fit with a double ionization ($\text{p}K_{\text{a}} = 5.6 \pm 0.3$,

Substrate	k_{cat} (s⁻¹)	K_m (μM)	k_{cat}/K_m (M⁻¹s⁻¹)
Histamine	6.6 ± 2.3	31 ± 11	213000 ± 37000
Agmatine	2.2 ± 0.1	37 ± 6	59800 ± 6000
Putrescine	1.9 ± 0.1	1280 ± 240	1480 ± 190
Trimethylamine	-	-	-
Methylamine	-	-	-

Table 1.1. Substrate specificity of HADH²⁴

$pK_a = 5.4 \pm 0.2$) with the fastest rate observed at pH below 6.0 (Figure 1.6).²⁴

The pK_a for imidazole in solution is 6.04 and most likely contributes to one of the ionizations, which suggests the mono-protonated form of histamine binds to the active site. The effect of ionizations in k_{cat}/K_m also suggested involvement of amino acid residues in substrate binding or stability, as observed with TMADH.²⁶ Two possible residues are Glu79 and Asp358, as they can provide ionic interactions to stabilize the positively charged amino group of histamine.^{7,30} pH values above 9.3 were not linear enough to obtain kinetic data, so it was not able to determined if the deprotonated amine (pK_a

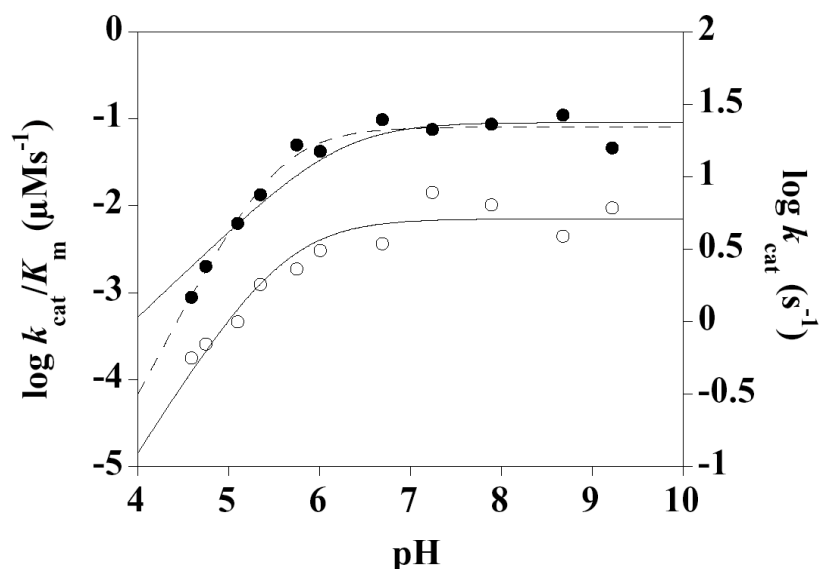


Figure 1.6. The plot of pH dependence on k_{cat}/K_m and k_{cat} . The solid dots represent the values of pH dependence on k_{cat}/K_m . The graph fits best to a double ionization ($pK_a = 5.6 \pm 0.3$, $pK_a = 5.4 \pm 0.2$) represented by the dashed opposed to the solid line that represents the a single ionization ($pK_a = 6.2 \pm 0.2$). The open circles represent the effect of pH on k_{cat} . The graph first best to a single ionization ($pK_a = 5.6 \pm 0.1$)²⁴

9.75) affected the rate. The neutral amines have been proposed to be the reactive species for MAO and TMADH.^{27 28} A single ionization ($pK_a = 5.6 \pm 0.1$) has also been observed for k_{cat} , but this could be attributed to the electron acceptor DCPIP ($pK_a = 5.8$) or an amino acid residue found in the active site.²⁴ Further studies such as site-directed mutation of Glu79 and Asp358 as well as using agmatine as a substrate were proposed to assign the pK_a s.²⁴

1.1.5. Deuterium Isotope Effect

The mechanism of C-H bond cleavage for flavoproteins has still much been debated. Efforts to understand the mechanism of histamine oxidation by HADH were recently undertaken by Limburg et al. by examining the isotope effect.²⁴ Studies with deuterated histamine demonstrated a partial rate limiting step with C-H bond cleavage with a $^D(k_{cat}/K_m)$ of 7.0 (± 1.8) under subsaturating concentrations. Under saturation conditions, the rate-determining step seems to involve the electron transfer step, analogous to TMADH.²⁵ This observed isotopic effect for HADH is close to the semi-classical maximum. This involves the H-tunneling and transfer that occur through the energy barrier separating reactant from product; therefore, it falls below the classical transition state. This process has been observed for copper amine oxidase from bovine serum.²⁹ Tunneling has also been suggested for TMADH, as a temperature-dependant KIE was seen at high pH values.²⁸ Scrutton et al. also observed a large kinetic isotopic effect for TMADH and purposed a nucleophilic addition for substrate oxidation.²⁸ Correlation of KIE of HADH and TMADH suggested a similar mechanism of substrate oxidation of HADH.²⁴

The understanding of the structure and function of HADH would benefit from the development of a recombinant expression of HADH. This will provide large quantity of enzyme for crystallography and sensor development. Spectroscopic and mechanistic studies including mutant protein would also benefit from an overexpression system of HADH. Solving the crystal

structure of HADH will aid towards the fundamental understanding how histamine binds in this enzyme. Understanding the binding motif in HADH, could provide understanding towards the binding of histamine in the human histamine receptor. This could possibly aid in the design of antihistamines.¹⁶ The crystal structure will also provide further interpretation and understanding of Limburg et al. research on C-H bond cleavage and substrate binding. The C-H bond cleavage mechanism is still unclear for many flavoproteins.³⁰ Further kinetic studies and substrate co-crystallization of HADH could potentially lead to understanding of C-H bond cleavage in HADH and flavoproteins. Also, with HADH's selectivity for histamine as a substrate, development of a biosensor for histamine will further help in understanding of this biogenic amine and move towards regulating histamine levels in humans and fish products.

1.1.6. C-H Bond Cleavage in Flavoproteins

The mechanism of C-H bond cleavage in flavoproteins is not fully understood. Techniques such as KIE, quantitative structure-activity relationships (QSAR), and radical and substrate inhibitors have been employed to understand the mechanism of C-H bond cleavage in monoamine oxidase (MAO),³²⁻³⁴ TMADH,^{28,31} and D-amino acid oxidase (DAAO).³¹ The three different mechanisms shown below have been proposed:

- 1) polar nucleophilic attack
- 2) electron transfer

3) hydride transfer

Figure 1.7 demonstrates these possible mechanisms of substrate oxidation.

9,32

1.1.6.1 Polar Nucleophilic Attack

The polar nucleophilic attack follows the mechanism described in Figure 1.7A. The free amine attacks the isoalloxazine ring at the C4a position. This is followed by proton abstraction at the C α position. Oxidation of substrate forms the imine, which is then hydrolyzed to the product aldehyde and ammonium ion. The reactivity of the flavin was confirmed by model^{36,37} and computation studies²² of the isoalloxazine ring. Further QSAR studies of MAOA were performed with *para*- and *meta*-substituted benzylamines.³² These studies demonstrate that the negative charge build-up at the benzyl carbon position, suggesting a proton abstraction mechanism as the mode of C-H bond cleavage. The results of mutagenesis and substrate inhibition studies on TMADH support polar nucleophilic attack, which will be discussed later on in the chapter.

1.1.6.2. Electron Transfer

The electron transfer mechanism involves the single electron transfer (SET) from the lone pair of the amine nitrogen to the flavin to yield an aminyl radical cation and flavin semiquinone (Figure 1.7B).³³ SET has been observed in electrochemical and chemical oxidation of amines, with the possibility of occurring in flavoproteins.³³ Radical formation in the active site

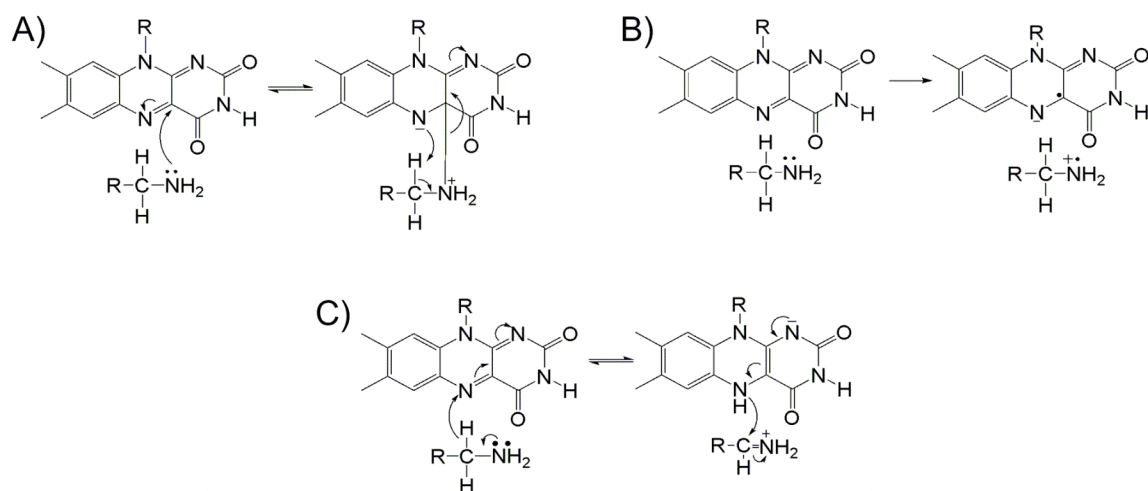


Figure 1.7. Possible mechanism for C-H bond cleavage in flavoproteins A) polar nucleophilic attack B) electron transfer C) hydride transfer^{9,32}

is also supported by highly reactive inhibitors, which upon radical formation in the active site, perform a ring opening mechanism that irreversibly inactivate the enzyme.³⁴ Studies on MAO with 1-phenylcyclopropylamine and 1-phenylcyclobutylamine showed that the enzyme underwent the one-electron reduction and the resulting radical reaction lead to the irreversible inactivation of the enzyme.³⁰ Recent efforts have been made to observe the radical formation in the active site by EPR spectroscopy.^{32,33} The radical formed by a single electron donation to MAO A on the FAD may exist in equilibrium with a stable tyrosyl radical, as observed by EPR spectroscopy.³⁵ Further evidence for radical formation includes an observed anionic flavin radical on the isoalloxazine ring in MAO A.³⁶ The difficulty in observing the SET mechanism

is the lifetime of the radical that is short-lived and proves to be very difficult to observe in the substrate oxidation.

1.1.6.3. Hydride Transfer

KIE and QSAR results for D-amino acid oxidase were compatible with transfer of a hydride from substrate to FAD.³¹ The linear free energy correlation demonstrated little, if any, development of charge in the transition state. The isotope effect and solvent effect were consistent with a highly concerted process and a symmetric transition state. There was also little effect for steric parameters, which negates the polar nucleophilic attack mechanism and the following mechanism for DAAO was proposed (Figure 1.7C).

1.1.7. pH Dependence of the Redox Properties of HADH

The recent discovery of HADH's cofactor and possible mechanism of C-H bond cleavage²⁴ has encouraged the Kano group to probe the pH dependence of the redox properties towards the reductive-half reaction of HADH.^{26,40} Stoichiometric titration of HADH with dithionite showed a disappearance of 6-S-Cys-FMN absorbance and the appearance of the 6-S-Cys-FMN semiquinone (6-S-Cys-FMN_S) at the beginning of the titration. The 6-S-Cys-FMN_S gradually decreased as the reduced 6-S-Cys-FMN (6-S-Cys-FMNH_R) formed. Plotting absorbance change as a function of dithionite concentration revealed three moles of dithionite reacting with one mole of HADH.⁴⁰ This was consistent with the reduction of TMADH with dithionite.³⁷

Reductive titration with histamine revealed a two to one mole ratio of histamine to enzyme, which is also seen in TMADH with trimethylamine.^{23,40} Redox potentials were measured using a spectroelectrochemical method at pH 7.0.⁴⁰ Similar results were observed for HADH and TMADH (Table 1.2).^{40,41}

When the pH dependence of the redox potentials was examined, little pH dependency was found for the 6-S-Cys-FMN oxidized to 6-S-Cys-FMN semiquinone couple (6-S-Cys-FMN_{O/S}).⁴⁰ The 6-S-Cys--FMN_S to 6-S-Cys-FMN_R couple (6-S-Cys-FMN_{S/R}) exhibited pH dependence towards the negative potential with a slope of -60 mV pH⁻¹, which suggests the single-electron transfer was coupled with single-proton transfer. The redox potential of the [4Fe-4S] cluster was observed by cyclic voltammetry. It is relatively free from pH dependency at pH < 9, but at pH > 9, the potential drops with a slope of -180 mV pH⁻¹.⁴⁰ The enzymatic activity of HADH is pH dependent with regards to acid-base equilibrium.⁴⁰ The potential for 6-S-Cys-FMN_{S/R} decreases (pH<9) with respect to FeS₀, suggesting an increased driving force of intermolecular transfer from the 6-S-Cys-FMN_S to the [4Fe-4S] with increasing pH. This data is also supported by the EPR spectra, which indicates an increase in the semiquinone radical at $g = 2$ as pH increases. This could play a role in the observed increased rate constant of HADH as it approaches pH 9. The redox potential of the cofactors gives insight into the reaction mechanism and the reductive half reaction of HADH.

	HADH (mV)	TMADH (mV)
FMN _O -FMN _S couple	+34	+44
FMN _S -FMN _R couple	+30	+36
FMN _R -[4Fe-4S] _O couple	+36	+102

Table 1.2. Redox potentials of the cofactor^{40,41}

1.1.8. Model Systems of Histamine Binding

One of the great interests of HADH is the substrate selectivity for histamine.²⁴ There are a few enzymes that have been either crystallized with histamine or a derivate of histamine.¹⁶ These histamine binding proteins could provide insight into the binding of histamine in HADH and also the physiological histamine receptor. Understand the binding of histamine could have implications in drug design of antihistamines.¹⁶ Many antihistamines have been designed for the treatment of various physiological disorders.^{38,39} Commercially available drugs provide allergy relief by targeting the histamine H₁-receptor in the body,^{44,45} while another line of histamine antagonists targets the H₂-receptor and suppresses excess stomach acid. Antihistamines are widely prescribed for various ailments, and the design of these drugs requires selectivity and specificity. Model systems of proteins that specifically

bind histamine have contributed to the understanding of how histamine binds to its receptor and could potentially help in designing specific and effective pharmaceutical drugs.¹⁶ All four membrane-bound histamine receptor proteins have been sequenced, but the three dimensional structures have yet to be determined.⁴⁶⁻⁴⁹ As previously mentioned, each histamine receptor (H1, H2, H3, H4) has distinct pharmacological roles and requires careful analysis. Various histamine binding proteins have been helpful in understanding both the mode of histamine binding and the pharmacological and toxicological profiles of certain antihistamines.¹⁶ These proteins vary in function and structure but all provide insight into the binding of histamine, which is broken down into two aspects. The first involves the imidazole ring of histamine as the major mode for binding, while the second binds histamine through the aliphatic amine for stabilization in the active site. In histidinal dehydrogenase, the imidazole group is stabilized by hydrogen bonding to a glutamic acid side chain and coordination to the zinc atom.⁴⁰ Carbonic anhydrase also binds histamine primarily through its imidazole ring; histamine hydrogen bonds with asparagine and glutamic acid residues and shares π - π interactions with histidine and phenylalanine.⁴¹ Histamine binding proteins (HBP), however, which are found in blood sucking insects, are examples of proteins that stabilize the free amine of histamine.⁵² In HBP, the aliphatic amine of histamine forms a salt bridge with the glutamic acid and aspartic acid residues. In HBP, however, the imidazole ring of histamine is also involved in

binding; imidazole has ionic interactions with glutamic acid and aspartic acid residues and is within π -stacking distances with phenylalanine and tryptophan.⁵² The polar, internal binding pocket of HBP is ideal for histamine and mimics what is known about how histamine binds to histamine receptors within the body. Through model studies and site directed mutagenesis, it was determined that the primary ligand binding pocket in the H1 and H2 receptors have aspartic acid, serine, and threonine residues that interact with the amine group of histamine via electrostatic interactions in a predominantly polar pocket.^{48,53,54} The conserved aspartic acid in human H1, H2 and H4 receptors is essential for binding histamine.⁴⁸ The imidazole ring is stabilized by both hydrogen bonding with two glutamic acid residues and also π -stacking with a tyrosine residue. The histamine binding pocket in human H1, H2, and H3 receptors may be regulated by the bulkier residues tyrosine, tryptophan and phenylalanine, as the H4 receptor does not contain these residues, which could explain the difference in histamine interaction.⁴⁸ Proteins that are selective for histamine will allow research towards the understanding of the physiological binding of histamine.⁴⁸ In addition, these proteins will potentially allow for the development of specific antihistamine drugs.

1.1.9. Detection of Histamine with a Biosensor

One application of HADH is the potential design of a histamine biosensor. Amperometric detection of histamine could be used to understand

the physiological role of histamine, in regulating histamine levels in humans and histamine concentrations in fish. Reports suggest that histamine could play a significant role in cancer.^{1,55} One example of this is the possibility that histamine acts as a mediator of proliferation in breast cancer.⁵⁶⁻⁵⁹ Mast cells are responsible for the release of histamine and they are found in large quantities around the edge of solid tumors.⁴² At normal concentrations histamine is an immunostimulant, but it is believed to be an immunosuppressant at high concentrations.⁴³ One study examined the involvement of histamine in breast cancer and found elevated levels of histamine in the cancerous breast tissue with respect to the adjacent noncancerous breast tissue.⁴² Elevated histamine levels are also associated with colon cancer.^{55,61} The specific role histamine plays in cancer remains unclear.^{62,63} Detection methods with improved sensitivity and specificity could further the understanding of histamine's involvement in cancer.

The methods of histamine detection in the cancer studies include either radioenzymatic assay⁴⁴ or an HPLC-based derivatization assay.⁵⁵ The official method for the determination of histamine in fish and fermented food, as recognized by the Association of Official Analytical Chemists (AOAC), involves the derivatization of histamine with the fluorophore.^{65,66} This method requires the time-intensive procedure of isolating pure histamine by removing impurities. These methods have been proven to detect histamine; however, the detection of contaminants^{67,68} and the multi-step purification of histamine

are both problematic.⁵⁵ A number of histamine detection kits are commercially available. These kits are performed by ELISA,⁴⁵ but the expense and time requirements (30 min to 2h) are not ideal.⁴⁶ An enzymatic, real-time biosensor that is specific for histamine would further our understanding of histamine and its involvement in cancer, as well as help prevent scombroid food poisoning.

Histamine accumulates in spoiled fish due to the microbial decarboxylation of histidine.¹⁷ This elevated level of histamine is the main toxic agent in scombroid food poisoning, which is one of the most common illnesses that occur due to the consumption of fish. The symptoms of this acute illness include sweating, rash, flushing of the face, diarrhea, and abdominal cramps. In severe cases, symptoms can include respiratory distress and swelling of the tongue and throat, which require sudden medical attention. Most cures include a dose of antihistamines to reverse the effects of excess histamine consumption.¹⁷

1.1.10. Understanding HADH through TMADH

1.1.10.1. Crystal Structure of TMADH

The high structural homology (40% identity, 56% similarity) of HADH and TMADH and the spectroscopic evidence supporting similar redox chemistry of HADH and TMADH, suggest TMADH is a good model for HADH.²⁴ The crystal structure of TMADH has been determined at 2.2 Å resolution, showing two identical subunits with a molecular mass of 83 kDa

each.²² The structure of TMADH consists of three distinct domains: a small domain (residues 495-648), a large domain (residues 1-383), and a medium domain (residues 384-494 and 649-733). The large domain contains the 6-S-Cys-FMN and [Fe₄-S₄] cluster and is comprised of an 8 parallel β -barrel enclosed with 8 parallel α -helices. The covalently linked 6-S-Cys-FMN is located in the first parallel β -barrel. Large excursions of the chain are found at the ends of several β -strands, which give enough mass to the large domain to bury the 6-S-Cys-FMN. The entire structural motif of TMADH contains 16 α -helices and 18 β -strands. The two redox cofactors are located near the center of the large domain and are separated by a center-to-center distance of 12 Å. The cysteines of the iron-sulfur cluster are contained in a short helix located at the end of the β -barrel. The [Fe₄-S₄] cluster is found approximately 20 Å from the surface of the protein. The 8 α -methyl of the 6-S-Cys-FMN is only 4 Å from the closest cysteinyl sulfur atom and 6 Å from the nearest iron atom. The close proximity of the 6-S-Cys-FMN and [Fe₄-S₄] cluster could give rise to the electron coupling seen in the EPR spectrum. It is proposed that upon reduction of the 6-S-Cys-FMN, electrons are passed from the 6-S-Cys-FMN to the closest cysteine ligand of the [Fe₄-S₄] cluster via the 8 α -methyl on the 6-S-Cys-FMN. The electron transfer is consistent with the reaction of various other flavoproteins that undergo electron transfer reactions.

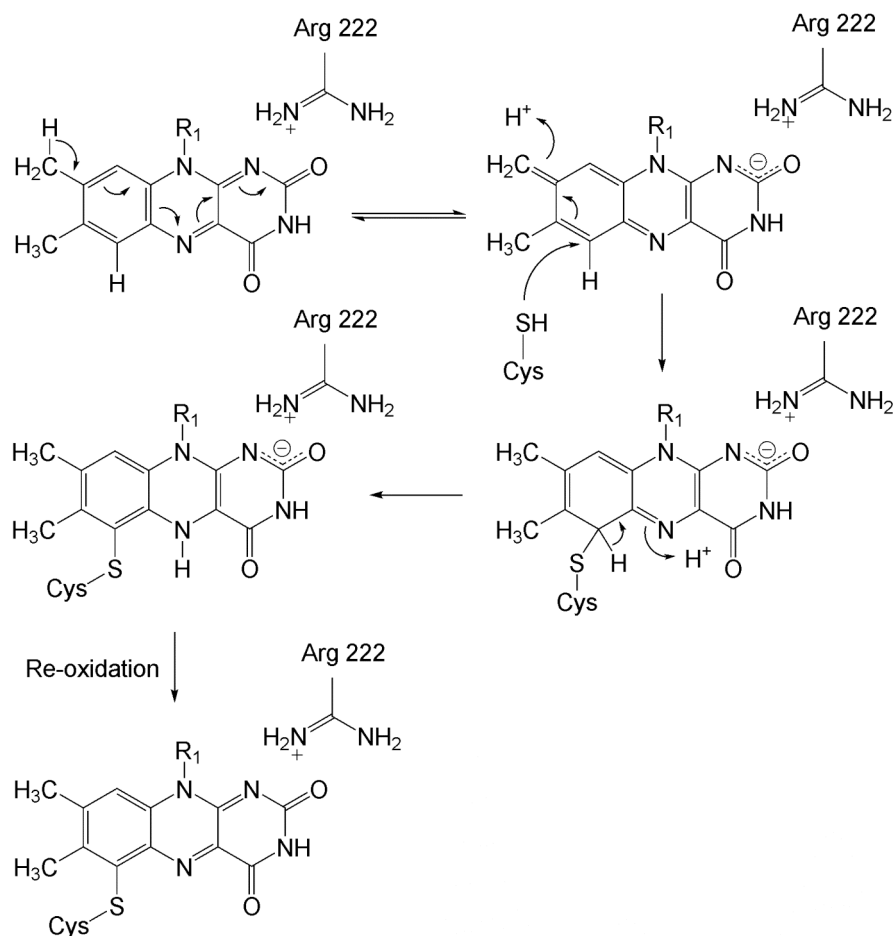
The 6-S-Cys-FMN is not planar and contains a high degree of bending (called a butterfly bend) in the active site.²² Computational studies were performed in attempt to understand the role of the butterfly bend in 6-S-Cys-FMN.^{71,72} Calculations were conducted on the energetically favored planar flavin versus the unfavorable nonplanar flavin. Results suggest that the energetically unfavored bend of the isoalloxazine ring raises its reduction potential from -220 mV to -10 mV in lumiflavin and from -174 mV to +17 mV in C6—methylsulfanyllumiflavin.^{71,72} The data suggest that the butterfly bend also raises the reduction potential in TMADH. These structural characteristics will aid in the understanding of HADH and its structural properties.

1.1.10.2. Covalent Linkage of 6-S-Cys-FMN

Mutagenesis studies on Cys30 and Trp335 in TMADH have aided in the understanding of the 6-S-Cys-FMN crosslinking.^{21,22,73} TMADH, DMADH, and HADH are the only enzymes known to contain the unusual 6-S-Cys-FMN.^{7,12} Cys30 is known to form a C6-covalent link with 6-S-Cys-FMN through nucleophilic attack by the thiolate group on cysteine.⁴⁷ However, when Cys30 was mutated to alanine in TMADH, the enzyme retained similar quantities of 6-S-Cys-FMN compared to the recombinantly expressed TMADH (26 and 30 % mol equivalent flavin: rTMADH to C30A TMADH, respectively).⁴⁸ The K_m of C30A was raised by a factor of two and k_{cat} was reduced by a factor of two with respect to the recombinantly expressed wild-type protein. The C30 bond was not required for the oxidative deamination of trimethylamine, although

inactivation of the enzyme mutant was seen with the addition of excess substrate or after approximately 10 turnovers. Inactivation of the enzyme was caused by formation of 6-hydroxy (6-OH) FMN with the C30A species. Thus, the C30 crosslink was thought to prevent the formation of the inactive 6-OH FMN. The inactive 6-OH FMN was characterized spectroscopically by observing the disappearance of the 440 nm peak and the appearance of a new peak at 400 nm. The C30A mutant species was treated with perchloric acid²¹ to remove the 6-OH FMN, which was then titrated and the peak at 600 nm was observed.⁴⁹ These spectra show a single ionization with a pK_a of ~ 7.0 , which is the known value for 6-OH FMN.⁴⁹ When the flavin isolated from the C30A mutant TMADH was analyzed by MALDI-MS, it was found to have a mass of 472.2 ± 0.1 Da,⁴⁸ which is within experimental error for the known 6-OH-FMN value of 472.3 Da.⁴⁹ Since 6-OH FMN was only recovered after substrate was added, while the as-isolated enzyme was devoid of 6-OH, it was thought that the 6-OH FMN forms by an hydroxide attack on the flavin substrate intermediate.⁵⁰ This theory on 6-OH FMN formation held until one of the three residues in the “aromatic bowl,” which is involved in cation – π bonding of substrate in the active site, was mutated.⁴⁸ Upon isolation and characterization of W355L, however, spectroscopic data showed a species similar to 6-OH FMN C30A. Isolation of the cofactor by perchloric acid revealed a single ionization with a pK_a of approximately 7.0 and an exact mass of 472.2 ± 0.1 , allowing it to be identified as 6-OH FMN.⁴⁸ The unique

characteristic of the 6-OH FMN formation in W355L was the fact that it formed in the absence of substrate. Only 8-21% of the isolated W355L TMADH contained 6-S-Cys-FMN, while 38-65% contained 6-OH FMN and 54-14% was in the deflavo form. (The different reported values are from two separate preparation of the enzyme.) This is different than the isolated C30A species, which only contained 6-OH FMN after the addition of substrate. After 6-OH FMN was found in W355L TMADH, both the native and recombinant forms were examined for this species. Native TMADH was found to contain 1.5% 6-OH FMN, while the recombinant form had 3%. The observation of 6-OH FMN formation in the wild type enzyme suggested that TMADH has the ability to derivatize the flavin without the use of substrate. The following mechanism of flavin derivatization in the absence of substrate was then proposed. (Scheme 1.2).⁴⁸ The hydroxylation proceeds through a flavin iminoquinone methide tautomeric form. An increase in electrophilicity at the C6 position is seen in the methide tautomeric form. Nucleophilic attack by either hydroxide or cysteine at the C6 position is followed by re-oxidation, which re-aromatizes the flavin to give either 6-OH or 6-S FMN. The methide tautomeric form has a negative charge between the N1 atom and the C2 carbonyl that is stabilized by the positively charged Arg222. Mutation of Arg222 to lysine compromised the formation of the 6-S-Cys-FMN link while mutation of Arg222 to valine completely abolished flavinylation of the enzyme.⁵¹ These results suggest that the mechanism of crosslink formation in flavoproteins involves a methide



Scheme 1.2. Proposed mechanism for formation of 6-OH-FMN (R₂=hydroxyl) or 6-S-Cys-FMN (R₂=cysteine)⁴⁸

tautomer, which creates an electrophilic position at the C6 or 8 α -methyl position on the isoalloxazine ring in flavoproteins.⁴⁸

1.1.10.3. Kinetics of Substrate Oxidation

One area of great interest for HADH is the reaction mechanism for the oxidation of substrate within the active site. The conserved residues and similar spectroscopic characteristics of TMADH and HADH suggest possible

similarities in the reaction mechanism.²⁴ Extensive enzyme kinetic studies on both wild-type and mutant forms of TMADH have been performed by Scrutton and coworkers.^{28,29,31,78} Cleavage of the C-H bond in flavoproteins is not well defined within the family of amine oxidizing enzymes. The four proposed mechanisms²⁸ of C-H bond cleavage in TMADH are the following:

- (1) Active base involved in proton abstraction, generating a carbanion species.⁵²
- (2) Formation of an ammonium cation radical followed by H-atom abstraction.⁵³
- (3) External radical involved in H-atom abstraction.⁵⁴
- (4) Nucleophilic attack of free base substrate, followed by proton abstraction by an active site base.⁵⁵

Kinetic studies on wild-type and mutant forms of TMADH were performed to discover whether the TMADH reaction pathway would fit one of these models.^{28,29,31,78,81}

1.1.10.3.1. TMADH Reaction Mechanism

Experiments with recombinant TMADH with the deuterated native substrate trimethylamine over the pH range 6.0 – 11.0 exhibited two ionizations in the Michaelis complex, with pK_a values of 6.5 and 8.5 and maximal activity seen in the alkaline region.²⁶ Mutations of TMADH were made to define the two ionization points and to further gain understanding of the reaction mechanism. The crystal structure of TMADH reveals several

residues involved in the active site, with an “aromatic bowl,” comprised of residues Tyr60, Trp264, and Trp355, that is involved in cation- π bonding of the substrate (Figure 1.8).^{22,82} Also in the active site are several basic residues (Tyr169, Tyr60, Try174, and His172) that possibly contribute to the observed ionization (Figure 1.9).²² Mutagenesis of these residues was performed, and plots of rate vs. pH were prepared to determine whether TMADH still exhibited ionization.^{28,29,78,82} The mutants Y169F and Y174F were cloned and expressed, but no change in the observed ionization or pH-dependent kinetic behavior occurred.⁵⁶ Mutation of Y169 to phenylalanine showed unique spectroscopic characteristics.^{28,78} In the crystal structure,²² Tyr169 is shown to have van der Waals interactions with the flavin cofactor and is hydrogen bonded to His172.⁵⁶ In the EPR spectrum of the Y169F mutant, the intense half field signal of $g \sim 4$ that was seen in the wild-type was not observed. This signal is attributed to the spin-spin interaction of the unpaired electron on the flavin semiquinone with the unpaired electron on the $[4\text{Fe-4S}]^+$.⁵⁶ Both wild-type and mutant spectra have a signal at $g \sim 2$ that accounts for both the axial signal of the semiquinone and the rhombic signal of the $[4\text{Fe-4S}]^+$. The Y169 is located next to the $\text{C}(2) = \text{O}$ group which is on the opposite side of the flavin ring from the $[4\text{Fe-4S}]$. The loss of the spin-spin interaction was rationalized by negative charge that develops due to the hydroxyl group, creating an electrostatic repulsion of the unpaired electron on the 6-S-Cys-FMN that pushes it towards the $[\text{Fe4-S4}]$ cluster.⁵⁶ This would

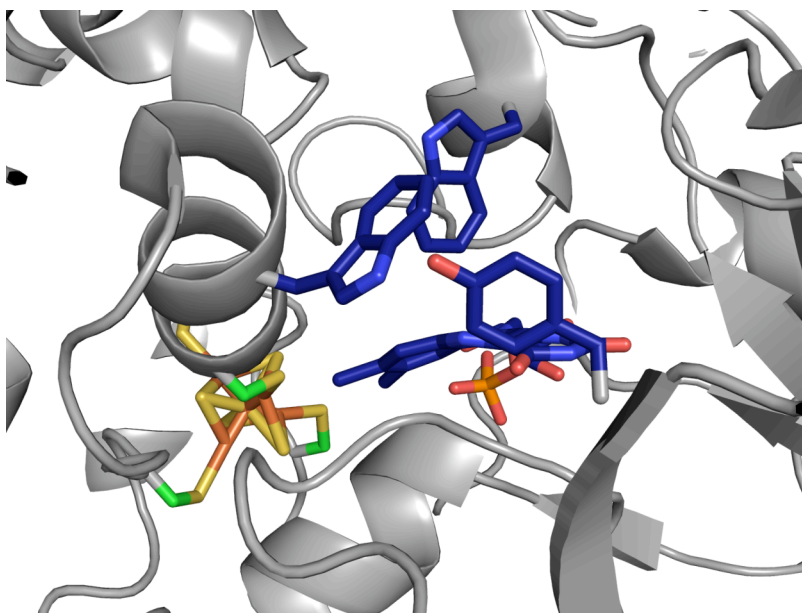


Figure 1.8. TMADH aromatic bowl²² All structures in the chapter were generated with pymol⁵⁷

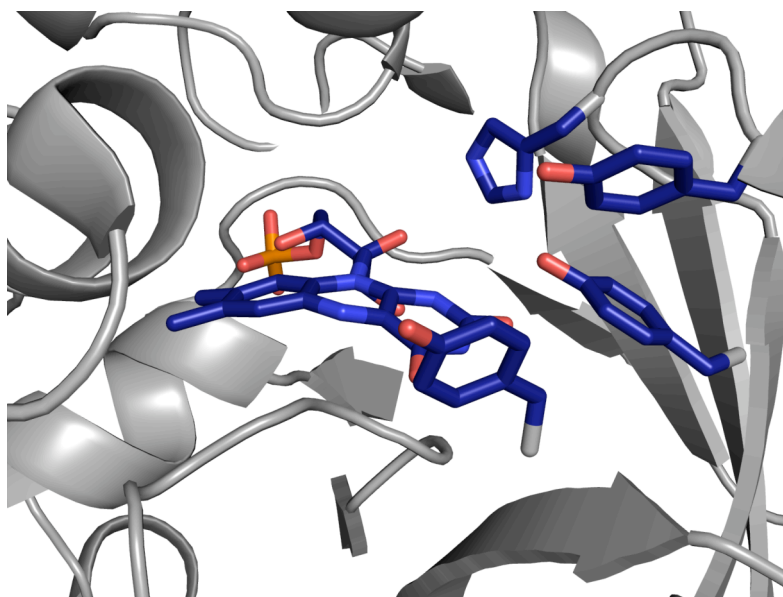


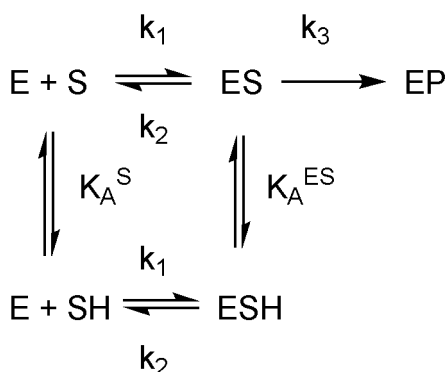
Figure 1.9. Basic residues in TMADH that possibly contribute to the observed ionization²²

reduce the spin-spin distance and therefore cause an increased spin-spin interaction.

Tyr60 is one of the three residues found in the “aromatic bowl” of the active site.⁵⁸ The Y60F mutant exhibits differences from the wild type TMADH. The Y60F data was fit to a double ionization which suggests little influence in the ionization observed; however, the Y60F mutant was shown to destabilize the basic form of the Michaelis complex by $\sim 1.3 \text{ kJ mol}^{-1}$, as the ionization shifted to a pK_a of 8.8. When His172 was mutated to Gln, the pK_a was 8.4 ± 0.1 , and the upper ionization was lost.²⁶ In the enzyme-substrate complex, this represents the ionization of the imidazolium side-chain of histidine that is necessary to control the rate of flavin reduction and maximal activity is observed following deprotonation of His172. A double mutant of Y60F and H172Q further reduced the stability of the trimethylamine base. As demonstrated by the double mutant, these residues contribute to the stability of the trimethylamine base by $\sim 2 \text{ kJ mol}^{-1}$ and over 3 pH units. This stabilization of the free trimethylamine (pK_a 9.8) is a result of both an amino-aromatic interaction between substrate and the hydroxyl group of Tyr60, as well as the imidazolium side chain of His172. These mutations demonstrate that both Y60 and H172 are important to the reaction mechanism, and the ionization of H172 is necessary for the rate of flavin reduction.

1.1.10.3.2. TMADH Active Base Determination

Since all of the possible ionizable residues were mutated, and only His172 influenced the upper ionization in the enzyme-substrate complex, the lower ionization remained undefined.²⁶ The oxidation of substrate by both wild-type and mutant TMADH has a large isotope effect (>7).^{28,29} In this study, His172 was mutated to simplify the observation of the lower ionization. In the case of H172Q, ionization of the protonated trimethylamine occurs at a pK_a of 6.8 ± 0.1 ; however, this value is shifted to pK_a of 7.4 ± 0.1 when the trimethylamine substrate is deuterated.^{28,29} This shift indicates that the deprotonation of the trimethylamine base corresponds to the lower ionization in the enzyme-substrate complex from moving from low to high pH. In the deuterated trimethylamine, the C-D bond contains a larger charge density and the N-H bond is more stable with respect to the C-H bond.^{28,29} The elevated pK_a value in the presence of deuterated substrate is therefore attributed to the N-H bond of the protonated trimethylamine dissociating easier than the deuterated trimethylamine. Scheme 1.3²⁸ demonstrates the controlled rate of flavin reduction based on protonation of substrate. The dissociation steps are in thermodynamic equilibrium based on the relatively slow conversion of ES complex to EP.²⁸ The buildup of unreactive ESH^+ complex that is seen in the deuterated substrate is caused by the increased pK_a . At pH 9.5 and above, the rates of reduction of the deuterated substrate and protonated substrate are equal, which means the substrate only exists in the S form and not in the SH^+ form.²⁸ This kinetic data suggest the deprotonation of substrate is



Scheme 1.3. Control of rate of reduction of 6-S-Cys-FMN by protonation of substrate²⁸

responsible for the lower ionization in the enzyme complex while the upper ionization is attributed to His-172 with the stability of substrate.²⁸

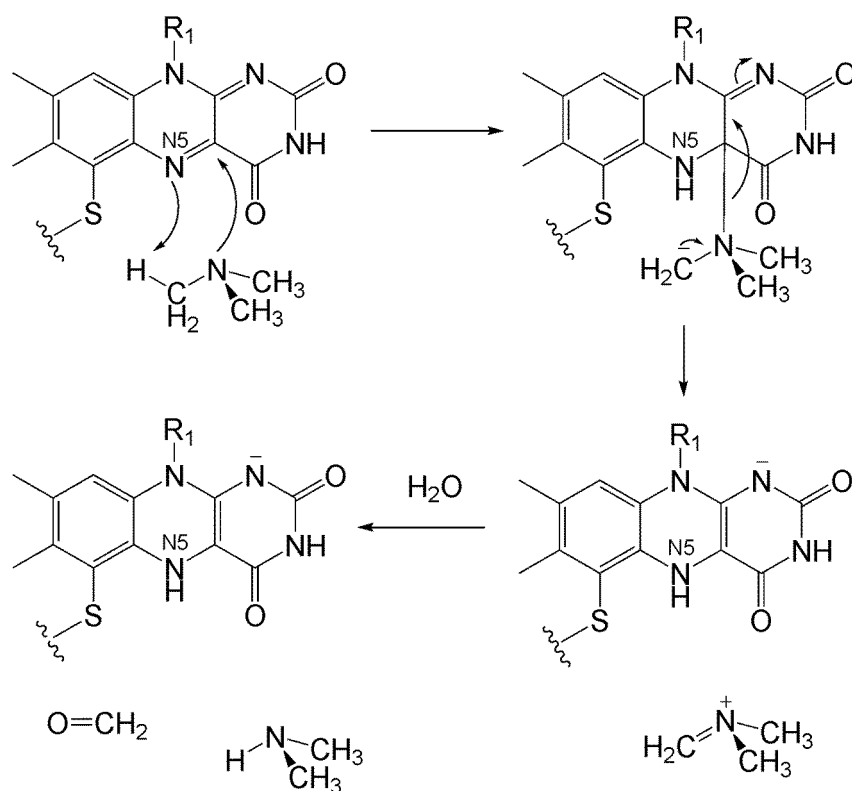
1.1.10.3.3. 6-S-Cys-FMN as an Active Base

Once characterization of the two ionizations in the Michaelis complex was accomplished, it was of interest to determine the active site base involved in the oxidation of trimethylamine.²⁸ All of the possible active site basic residues were examined by point mutations to identify their role in the substrate oxidation mechanism.^{28,29} Tyr169, Try60 and His172 are the potential active site bases, so these were mutated to observe their catalytic influence. As mentioned previously, two ionizations were observed in the Y169F and Y60F species.^{28,31,78} The H172Q TMADH mutant exhibited a 10% reduction in rate constant and loss of the upper ionization.²⁶ Therefore, the ionization of this residue influences the rate of reaction, but it is not the active site base. The mechanism of the enzyme monoamine oxidase A³² and D-

amino acid oxidase⁵⁹ demonstrate how the N-5 atom of the flavin can act as a base for C-H bond cleavage. This mechanism also suggests nucleophilic attack of the free amine on the C4 atom of the flavin isoalloxazine ring (Scheme 1.4).²⁸

Computational studies on lumiflavin and C6-methylsulfanyllumiflavin were performed in order to calculate the energies associated with the reduction of the 6-S-Cys-FMN.^{71,72} Both were analyzed as part of the wild type structure and part of a Cys30 mutant species, which is involved in the covalent crosslinking of the flavin within the enzyme. The wild-type structure exhibits an area of negative charge on both the C6 sulfur involved in the crosslink and on the N5 of the flavin that is believed to deprotonate the trimethylamine, suggesting the N5 atom possesses the nucleophilic properties necessary for the mechanism.²² Examination of the lowest unoccupied molecular orbital (LUMO) demonstrates significant orbital density on the N5 and C4 of the flavin. The N5 atom has a negative charge of < -0.5 e, which again supports the mechanism of deprotonation.²² The C4 atom has a positive charge of >0.0 e, which supports the mechanism of nucleophilic attack on the electrophilic C4a atom.²²

The reaction of phenylhydrazine also supports the mechanism of nucleophilic attack at the C4 position.⁶⁰ When the enzyme is incubated with phenylhydrazine, the 440 nm band attributed to the flavin is lost, and a new band grows in at 360 nm.⁶⁰ This new species at 360 nm was tested for



Scheme 1.4. Proposed oxidation reaction mechanism for TMADH²⁸

activity and was found to be 94% inactive. Isolation of this new species from proteolytic digests led to the discovery of the flavin being arylated at the C4 position.⁶⁰ This supports the theory of the C4 position of the flavin being the site of nucleophilic attack by substrate.^{31,84}

The data suggest the following mechanism for the oxidative deamination of trimethylamine by TMADH (Scheme 1.4).²⁸ The free trimethylamine base is deprotonated by the N5 atom of the flavin, and subsequently the deprotonated trimethylamine nucleophilically attacks the C4 atom. N-methyl-N-methylenmethanaminium is released from the flavin

before water oxidizes the substrate to form formaldehyde and dimethylamine. HADH is known to have a KIE > 7, butterfly bend in the 6-S-Cys-FMN, and react with phenylhydrazine which is reasonably to assume similarities within the reaction mechanism.²⁴

1.1.11. Reductive Half-Reaction of TMADH

There is spectroscopic evidence of a single unpaired electron on the [4Fe-4S] and on the semiquinone for both HADH and TMADH during the reductive half-reaction.^{7,81} The reductive half-reaction of TMADH with its natural substrate trimethylamine (TMA) was studied over the pH range 6.0 – 11.0.⁶¹ This reaction exhibits three resolved kinetic phases,^{23,24,26,81} which include a fast, intermediate, and slow phase.⁶¹ The reductive half-reaction begins with the fast phase, which is a two electron reduction of the flavin. The intermediate phase, follows with intramolecular electron transfer to the iron sulfur cluster from the dihydroflavin. The slow phase consists of product release and involves spin-spin interaction of the unpaired electrons on the [4Fe-4S]⁺ and the flavin semiquinone. The kinetic information of these three phases was determined by stopped-flow spectroscopy of the observable changes at 450 nm, 365 nm, and 520 nm at pH 8.0 and 10 °C.⁶¹ A reduced temperature was used because reduction of TMADH at elevated temperatures is very fast and prohibits detailed analysis. The rate constants from the spectroscopic data for each step are as follows: $k_{\text{fast}} = 500 \text{ s}^{-1}$; $k_{\text{int}} = 17 \text{ s}^{-1}$; and $k_{\text{slow}} = 1.6 \text{ s}^{-1}$.⁶¹ The data were collected at pH 8.0, since below

pH 7.0, the intermediate phase is difficult to resolve due to the small spectral change. Above pH 9.5, the rate constant for the slow phase and intermediate phase approach each other at high substrate concentration. The rate constants of both the slow and intermediate phases show a dependence on substrate concentration, where rate decreases as the substrate concentration increases. The degree of substrate inhibition increases with pH. A 50 % reduction in activity is seen for the intermediate phase, going from ~ 2 mM substrate at pH 7.5 to ~ 0.3 mM substrate at pH 9.5.⁶¹ The slow phase sees a reduction from ~ 20 mM substrate at pH 6.0 to ~ 1 mM substrate at pH 8.0.

1.1.12. Oxidative-Half Reaction

Reoxidation of HADH is known to occur by an external electron acceptor, but the identity of this electron carrier is unknown. The oxidative half-reaction of TMADH has been well characterized by mutagenesis and kinetic studies.^{62,63} As mentioned earlier, the reductive half-reaction of TMADH involves three kinetic phases.⁶¹ The fast phase involves the two electron reduction of 6-S-Cys-FMN, followed by the intermediate phase of intramolecular electron transfer from the reduced 6-S-Cys-FMN to the [4Fe-4S] center. Upon the release of product and binding of substrate, the slow phase involves the spin-spin interaction of the flavin-semiquinone and reduced [4Fe-4S] center. The [4Fe-4S] is reoxidized by the intermolecular transfer of electrons to the external electron acceptor.⁵⁰ The physiological

electron acceptor for the reoxidation of TMADH is an electron transferring flavoprotein (ETF),⁵⁰ but the physiological electron acceptor of HADH has yet to be determined.

Studies on the oxidative half-reaction of TMADH could aid in determining the mechanism of electron transfer from HADH to the electron acceptor. Residues involved in the intermolecular transfer from the [4Fe-4S] of TMADH to the surface of the protein were believed to be Tyr422 and Val344.⁴¹ The crystal structure of TMADH reveals a small groove by the [4Fe-4S], by which the FAD of the ETF could potentially bind.⁸⁵ Y422 and V344 are located in this small groove, with V344 providing the shortest pathway from the Cys-345, one of the cysteines that coordinates the [4Fe-4S], to the surface of TMADH.⁶² Y422 is involved the second pathway, which proceeds from C345 to Glu-439 then to Y442. Several mutations of Y422 and V344 were performed in order to either increase or decrease the side chain volume at these two positions.⁴¹ Ferricenium ions and ETF were both employed for the kinetic analysis of the Y422 and V344 mutants.⁴¹ In ensure that the mutant did not affect the oxidation of substrate, steady-state kinetics were examined to compare the reductive half reaction of the wild type to the mutants species. The mutants caused very little perturbation of binding and oxidation of substrate.⁶²

To understand how the mutations affected the electron transfer of TMADH, the mutants underwent steady-state kinetics with the artificial

electron acceptor Fc^+ .⁶² The mutants V344C, V344A, and V344G caused an increase in reaction rate of electron transfer to Fc^+ . Likewise, the larger, bulkier side chains of isoleucine and tyrosine caused slower electron transfer to Fc^+ . The Y442 mutants had little to no effect on the rate of electron transfer to Fc^+ . Evidence suggests that V344 represents the shortest route from the [4Fe-4S] to the surface.⁶² The shorter the side chains on the residues, the shorter and quicker the electron transfer to Fc^+ . Similarly, larger residues have longer and slower electron transfer, consistent with shorter and quicker route.

The oxidative half reaction of these mutations on TMADH was also examined with ETF.⁶² The V344 mutants had little effect on electron transfer, but mutations at the Y422 position perturbed the electron transfer significantly. The Y442G mutant had the greatest increase in dissociation constant for the ETF-TMADH complex and had a 10-fold decrease in rate constant compared with the wild type. Y442C also had a decrease in rate constant, though not as significant. This rate reduction in the Y442 mutants changed the geometrical alignment of the TMADH-ETF complex making electron transfer more difficult and less efficient. While the residue Y442 is more involved with the electron transfer from TMADH to the ETF, the role of V344 in the electron transfer to ETF was seen as minimal. This study shows the transfer of electrons to the ETF proceeds through Y442, while V344 plays a minimal role in this process.⁶²

1.1.13. Substrate Selectivity

The substrate selectivity that HADH has for histamine represents one of the unique properties of this enzyme. The substrates for which HADH is selective include histamine ($K_m = 31 \mu\text{M}$, $k_{\text{cat}}/K_m = 2.1 \times 10^5 \text{ M}^{-1}\text{s}^{-1}$), agmatine ($K_m = 37 \mu\text{M}$, $k_{\text{cat}}/K_m = 6.0 \times 10^4 \text{ M}^{-1}\text{s}^{-1}$), and putrescine ($K_m = 1280 \mu\text{M}$, $k_{\text{cat}}/K_m = 1500 \text{ M}^{-1}\text{s}^{-1}$).²⁴ As mentioned previously, HADH shares 40% identity and 56% similarity with TMADH and 37% identity and 51% similarity with DMADH.²⁴ Observation on substrate selectivity of these two protein could provide insight into the histamine selectivity of HADH.⁵⁸ TMADH and DMADH, which are selective for tertiary and secondary amines respectively, share a 63.5% sequence identity.⁵⁸ When comparing the active site residues of TMADH with DMADH, most are conserved. There are three residues which are not conserved (Tyr60 to Gln, Ser74 to Thr, and Trp105 to Phe, TMADH numbering) that could contribute to the selectivity of tertiary amines in TMADH verses secondary amines in DMADH.⁵⁸ As described above in TMADH, Y60 is one of the three residues involved in the aromatic bowl region for cation- π binding of the alkylammonium ion substrate. Cation- π interactions within the proteins have been observed in very diverse structures, from acetylcholinesterase⁶⁴ to the SH2 domain of the v-src oncogene.⁶⁵ The cation- π interaction of the alkylammonium ion with the aromatic bowl in TMADH represents the largest group of biologically relevant organic cation ligand binding. In DMADH, the Y60 residue is changed to glutamine and

modeling studies suggest that the change to glutamine in DMADH provides hydrogen bonding with the N-H of the dimethylammonium substrate.⁶⁶ The other two non-conserved residues pack against the Y60, and model studies of DMADH suggest that these residues influence the position of Gln60, giving it the ability to hydrogen bonding to the substrate; thus, the difference in substrate specificity would depend on these three residues.⁵⁸

Mutagenesis studies on TMADH were performed (Y60Q, S74T, and W105F) in attempt to switch its substrate specificity from TMA to DMA.⁵⁸ In wild type TMADH, DMA is a poor substrate where the ratio of selectivity coefficients for TMA to DMA is about 4000. The K_m value for TMA is 13.7 μM , versus 2.3 mM for DMA. The value of k_{cat} for substrate is 0.67 s^{-1} for TMA and 15.6 s^{-1} for DMA. Upon the triple mutation of TMADH (Y60Q, S74T, and W105F) an increase in K_m and an 800-fold decrease in k_{cat} were observed with TMA as a substrate. Reaction of triple mutated TMADH with DMA did not show a significant change in K_m or k_{cat} . Even though both substrates bind in the same location, the mutations seemed to only impair the binding of TMA. The effects of the TMADH mutations on the reductive half reaction were also examined. Flavin reduction is monitored spectroscopically by the decrease in absorbance at 443 nm, along with the growth of a peak at 365 that corresponds to the formation of the 6-S-Cys-FMN_{sq}-[4Fe-4S]⁺ species that results from the intramolecular electron transfer from the dihydroflavin. When triply mutated TMADH is reacted with TMA, the

rate of flavin reduction is reduced around 4000-fold, while minimal reduction in rate was observed with DMA as substrate. In contrast to wild-type, the specificity of the overall reductive half reaction favors DMA by 82,000-fold. An Absorbance change at 365 nm for the mutant TMADH reacting with TMA was monophasic and displayed no tendencies for substrate inhibition, in contrast with the biphasic wild type enzyme, in which each phase is controlled by substrate concentration. The reaction of mutant TMADH with DMA was biphasic and exhibited faster intramolecular electron transfer from the reduced 6-S-Cys-FMN to [4Fe-4S].⁵⁸

The enzymes TMADH and DMADH have active sites that contain highly conserved residues.⁵⁸ Mutation of TMADH residues Y60 (aromatic bowl) and S74 and W105 (interaction with Y60) was performed in order to change substrate specificity towards that of DMADH.⁵⁸ These residues are not conserved within the active sites of the two enzymes. These mutants greatly diminish substrate TMA from binding and decrease the reduction of 6-S-Cys-FMN. Of the three residues in the aromatic bowl, only Y60 (Gln60 in DMADH) is not conserved, which signifies the selectivity of TMADH for the trimethylammonium ion instead of the dimethylammonium ion.⁵⁸

1.1.14. Substrate Inhibition

HADH exhibits substrate inhibition at high concentrations of substrate, which is likewise seen in TMADH.²⁴ The steady-state reaction of TMADH has been studied in attempt to understand the substrate inhibition. As mentioned

above, TMADH and HADH exhibit similar spectroscopic properties upon reaction with substrate;²⁴ therefore, a similar mechanism of substrate inhibition would be expected to be seen in both of these enzymes. The redox cycle of TMADH was studied under steady-state conditions with the artificial electron acceptor ferricenium hexafluorophosphate (Fc^+).²⁵ Fc^+ was used since it does not interfere with the spectroscopic region used for analyzing the rate of reduction of TMADH, and it is shown to be comparable to the electron flow that is seen with physiological redox acceptor, ETF.

Stopped-flow studies monitored the decrease in absorbance at 443 nm (6-S-Cys-FMN) for the reduction of TMADH by substrate and increase in absorbance at 365 nm (anionic flavin semiquinone) and 440 nm (oxidation of the iron-sulfur cluster).²⁵ TMADH turnover was observed at a constant concentration of Fc^+ (100 μM) and varied concentration of TMA (20 μM – 2 mM). At lower TMA concentration, the peak at 365 nm is not observed, while the peak for oxidized 6-S-Cys-FMN at 443 nm is observed, which suggests the oxidized 6-S-Cys-FMN is the dominant species at low substrate concentrations. At high substrate concentration, the absorbance at 365 nm grows in, while the peak at 443 nm is lost, indicating that the semiquinone of 6-S-Cys-FMN is the predominant species. The peak at 440 nm, which represents oxidized $[\text{Fe}_4\text{-S}_4]$ cluster, is observed at high substrate concentrations. Spectral analysis at intermediate concentration of TMA (55 and 100 μM) demonstrated both a semiquinone peak at 365 nm and oxidized

6-S-Cys-FMN peak at 443 nm, indicating both species are present at intermediate substrate concentrations. Concentrations of Fc^+ were also varied to observe substrate inhibition. The oxidized enzyme at 443 nm was seen at high concentrations of Fc^+ while low Fc^+ concentrations caused the semiquinone to be the predominant species. When the Fc^+ concentration is lowered to 50 μM and concentration of TMA is varied (20 μM – 2 mM), the oxidized 6-S-Cys-FMN is not observed and the semiquinone and oxidized [Fe-S] cluster are present.²⁵

A proposed branching mechanism for TMADH was constructed with two paths in the 0/2 cycle and 1/3 cycle (Figure 1.10).²⁵ At low TMA and high electron acceptor concentrations, the 0/2 cycle predominates with the two-electron reduction of the enzyme in the catalytic cycle. At high TMA and lower Fc^+ concentrations the 1/3 cycle will predominate, where substrate binds to the one-electron reduced enzyme, leading to substrate inhibition. The binding of substrate stabilizes the semiquinone, shifting the potential of the [Fe-S] cluster from +102 mV to +50 mV. The potential of the quinone/semiquinone couple increases from +44 mV to +240 mV and the semiquinone/hydroquinone couple decreases from +36 mV to -50 mV. This effect stabilizes the semiquinone oxidation state of 6-S-Cys-FMN and shifts the equilibrium of the oxidation-reduction potential towards the semiquinone and oxidized [Fe-S] cluster. The bound substrate is not able to reduce the

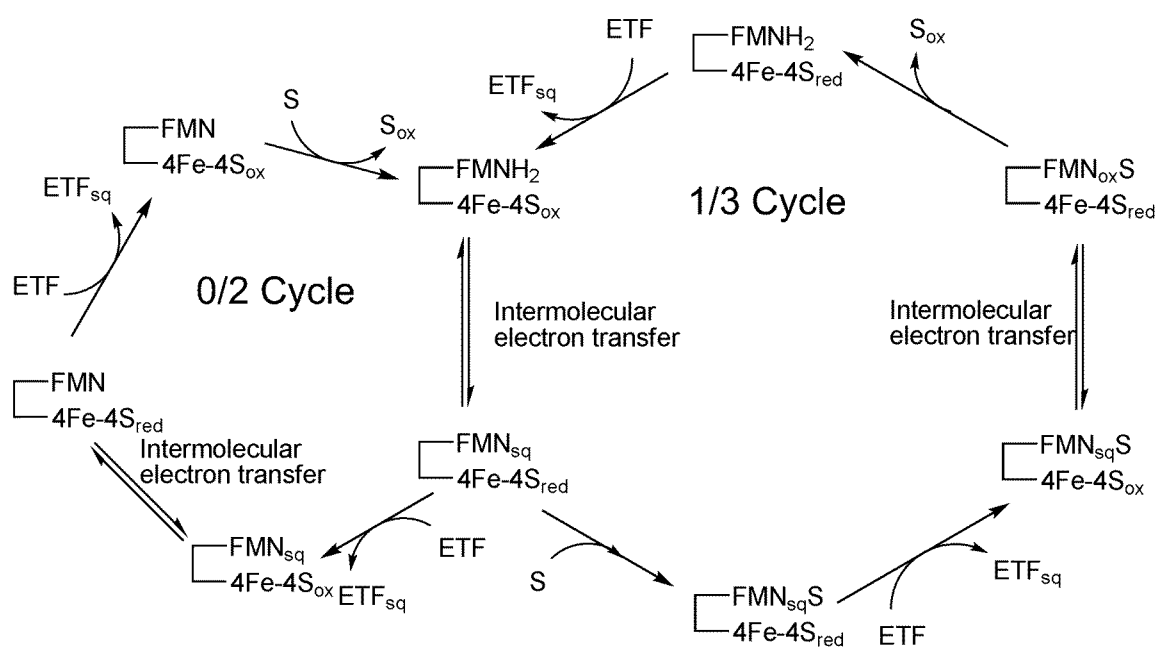


Figure 1.10. Proposed mechanism for TMADH for 0/2 and 1/3 cycle²⁵

enzyme when 6-S-Cys-FMN is in the semiquinone state, so catalysis is inhibited.²⁵

1.1.15. Expression and Purification of recombinant HADH

The selectivity and specificity of HADH for histamine makes it an interesting protein of which to pursue structural determination. Understanding the selectivity for histamine has the potential to improve antihistamine drug design and will provide information on the binding of histamine to natural histamine receptors. HADH is a recently discovered protein that has yet to be crystallized. A high yield expression system and crystallographic determination of HADH will aid in furthering the understanding this protein.

Native expression of HADH from *N. simplex* yields 0.5 mg L⁻¹. For this reason, a recombinant over expression system for HADH was desired in order to conduct kinetic studies and X-ray crystallography. Discussed in this chapter is the expression and purification of recombinant HADH (rHADH) developed by Dr. Hirakawa used herein to generate the HADH protein for crystallization. The SDS-PAGE and spectroscopic evidence support that rHADH is comparable to native HADH.

1.2. Materials and Methods

1.2.1. Cloning and expression

The *hadh* gene was cloned from genomic DNA of *N. simplex* (ATCC 6946).²⁴ PCR was performed on the HADH gene with the following primers:

Seq 5' to 3' GCTCTAGACATATGACCGAGCAGC

Seq 3' to 5' GGAATTCAAGCTTTCACGCCAGCTGGGTGA.

Due to the GC rich nature of the gene, 10 µL GC-Rich PCR system PCR reaction buffer (Roche Applied Science) and 1 µL of GC-Rich PCR system nucleotide mix (Roche Applied Science) were added to 50 µl of PCR reaction solution. PCR was performed with the following conditions: an initial 95 °C for 5 min, then cycled between 95 °C for 1 min, 60 °C for 30s and 72 °C for 5min, for a total running time of 5 hours. The primers were designed to amplify the 2.1 Kbp fragment and incorporate EcoRI (New England BioLabs) and XbaI (New England BioLabs) flanking sites for subsequent insertion into pUC19. The resulting *hadh* gene was sequenced with the following primers:

M13 and M13R

HSDHseq1 GAGCGCCCAGGCCTCGATGCGC

HSDHseq2 TACAGCGGCGTCCACCACTTCC

HSDHseq3 GCTCCACACGGCGGCCGCGATC

HSDHseq4 CTGCGCGAGCAGCTCGGCCACGAC

in the forward and reverse directions and then subcloned between the NdeI and EcoRI sites of pET21b (Novagen) in order to express the recombinant protein without the C-terminal T7-tag or the N-terminal His-tag. The plasmid was transformed into *E. coli* Rosetta 2 (DE3) cells (Novagen). The cells were grown in 1 L of Terrific Broth media with 100 mg L⁻¹ ampicillin at 37 °C and shaken at 225 rpm to an OD₆₀₀ of 0.7. Protein expression was induced with 0.1 mM isopropyl β-D-1-thiogalactopyranoside (IPTG). 250 mg L⁻¹ Iron sulfate and 50 mg L⁻¹ riboflavin were also added at an OD₆₀₀ of 0.7 to ensure full incorporation of the [Fe₄-S₄] cluster and FMN cofactors. The temperature was reduced to 20 °C and the cultures were allowed to shake at 225 rpm overnight. The cells were harvested by centrifugation at 4°C.

HADH was also grown in selenomethionine rich media in order to obtain selenomethionine-substituted protein for multiwave anomalous dispersion (MAD) data set. The same plasmid was transformed into the methionine-auxotrophic *E. coli* strain B834 (DE3) (Novagen).⁶⁷ The cells were grown in SelenoMet Medium Base (AthenaES) where 21.6 g SelenoMet Medium Base was dissolved in 1 L of deionized water. The media was

autoclaved and allowed to cool. 5.1 g SelenoMet mix was dissolved in 50 mL of deionized water and the solution was sterile filtered. The resulting SelenoMet solution, 100 mg L⁻¹ ampicillin, and 30 µg/mL L-SeMet were added to the selenomet medium base. 5 mL of media was removed and LB was added to 5% concentration to grow the starter culture. The starter culture was allowed to grow overnight and was used to inoculate the 1 L base media. Induction and expression of HADH protein followed previous methods. Efforts for higher incorporation of selenomethionine into the protein were made by increasing the amount of L-SeMet added to the selenomethionine medium to 60 µg/mL. In addition, the starter culture was spun down and washed twice with SeMet media before inoculation and induction with IPTG.

1.2.2. Purification

Cells (10 g) were resuspended in 20 mM potassium phosphate buffer (pH = 7.4) containing 0.1 M KCl. Cells were lysed by ultrasonication, and centrifuged at 40 000 *g* for 30 min. The supernatant was loaded onto a 100 mL Toyopearl-DEAE column pre-equilibrated with 20 mM potassium phosphate (pH = 7.4) containing 0.1 M KCl, and proteins were eluted with a 300 mL linear gradient increasing from 0.1 to 0.3 M KCl (20 mM potassium phosphate buffer, pH 7.4). Fractions exhibiting an Abs₄₄₄/Abs₃₈₂ ratio of 1.0 or higher were pooled and (NH₄)₂SO₄ was added to a final concentration of 0.8 M. The protein solution was then loaded on to a 100 mL Toyopearl Butyl-650 column (Tosoh Bioscience) pre-equilibrated with 50 mM potassium phosphate

buffer (pH = 7.4) containing 0.8 M $(\text{NH}_4)_2\text{SO}_4$. Bound proteins were eluted with a 300 mL gradient decreasing from 0.8 to 0 M $(\text{NH}_4)_2\text{SO}_4$ (50 mM potassium phosphate buffer, pH = 7.4). Fractions exhibiting an $\text{Abs}_{444}/\text{Abs}_{382}$ ratio of 1.2 or higher were pooled and concentrated to 1 mL using an Amicon Ultra-30 centrifugal unit (Millipore). This protein was loaded onto a HiLoad Superdex 200 sizing column (GE Biosciences) and eluted with 50 mM Tris-HCl (pH 7.4) containing 0.15 M KCl. Fractions with an $\text{Abs}_{444}/\text{Abs}_{382}$ ratio of 1.38 or higher were concentrated to >20 mg/mL. The purity of HADH was confirmed with SDS-PAGE and protein concentration was determined by a BCA assay (Thermo Fisher Scientific).

Selenomethionine-substituted protein was purified as described with around ~10 fold reduction in cell paste and protein expression. Flavination, purity and activity were all in agreement with the recombinant expressed HADH. The incorporation of selenomethionine was determined by MALDI-TOF mass spectrometry at the KU Analytical Proteomics Lab.

1.2.3. HADH Coupled Assay

HADH coupled assay was measured using the electron acceptor dichlorophenolindophenol (DCPIP) coupled to the redox mediator phenazine methosulfate (PMS) according to published procedures with slight modifications.²² 0.5 μg of HADH was added to 0.1 M Tris buffer pH 7.0 containing 500 μM PMS, 50 μM DCPIP, and 0- 2 mM histamine. The bleaching of the absorbance at 580 was observed on Cary UV/Vis

spectrophotometer with constant temperature (30°C). The activity rate of enzyme was plotted against histamine concentration

1.3. Results

1.3.1. The Cloning of HADH gene in pET21b Vector Achieves

Expression of Soluble Protein.

The *hadh* gene of *N. simplex* was amplified with PCR and confirmed by the presence of a 2.1 Kb band on a 1% agarose gel. The amplified gene was extracted and purified (Quigen) and digested with EcoRI and XbaI for ligation into pUC19. The size of the cloning vector pUC19 enables easier sequencing and the confirmation that no undesired mutation was introduced into the *hadh* gene. The plasmid was subjected for sequencing (UC Berkeley) in a concentration of ~ 500 µg/mL with 0.5 µg DNA/5kb DS plasmid with 3.2 pmol primer in 13 µl water. Sequencing results were in good agreement with wild-type *hadh* (Figure 1.11). The plasmid was digested with EcoRI and NdeI and ligated into the pET21b expression vector for the purpose of transforming and expressing the protein in bacteria. Incorporation of the *hadh* gene into the pET21b expression vector was confirmed on a DNA agarose gel demonstrating a band for the *hadh* gene (2.1 Kb) and the pET21b vector (5.4 Kb) after digestion with EcoRI and NdeI.

1.3.2. The Expression of Soluble HADH yields high yield (~20 mg/L protein) and High Purity for Crystallography.

Starter cultures were prepared, and soluble protein was observed in a 1 L culture grown expression in LB with a protein band at 76 kDa, which is in good agreement with wild-type HADH. Optimization of soluble protein expression was performed with TB, LB, and 2X YT media (Figure 1.12). SDS-PAGE revealed that protein expression was highest in TB media based on intensity of an anionic dye (coomassie blue) that binds non-specifically to protein. The protein was purified as fully flavinated and purity of fractions were examined after each step. Figure 1.13 shows the 12.5% SDS-PAGE gel after each stage of purification. After each column, the SDS-PAGE gel reveals the separation of unwanted protein. The major band seen in the SDS-PAGE gel was in good agreement with the calculated molecular weight (76 kDa) of HADH. Full flavination was confirmed based on the Abs_{444}/Abs_{382} ratio of 1.4 indicating full incorporation of 6-S-Cys-FMN into the protein, as seen in the native HADH.⁶⁸ Figure 1.14 depicts the absorbance spectra and the Abs_{444}/Abs_{382} ratio after each stage of purification. The progressive increase of the Abs_{444}/Abs_{382} ratio after each purification step demonstrates the removal of impurities. After the first column, DEAE column, the average expected Abs_{444}/Abs_{382} ratio is 1.15, where the butyl column increases the average value of 1.25-1.30 column. Fractions from the size exclusion column demonstrated an Abs_{444}/Abs_{382} ratio of 1.38, indicating flavination is very

	10	20	30
HADH_Native			
rHADH	MTEQPAVAAPYDVL	FEPVQIGPFTTKNRFY	
	40	50	60
HADH_Native			
rHADH	QVPHCNGMGYRDPSAQASMRKIKAEGGWSA		
	70	80	90
HADH_Native			
rHADH	VCTEQVEIHATSDIAPF	IELRIWDDQDLPA	
	100	110	120
HADH_Native			
rHADH	LKRIADAIHEGGGLAGIELAHNGMNAPNQL		
	130	140	150
HADH_Native			
rHADH	SRETPLGPGHLPVAPDTIAPIQARAMTKQD		
	160	170	180
HADH_Native			
rHADH	IDDLRRWHRNAVRRSIEAGYDIVVYGAHG		
	190	200	210
HADH_Native			
rHADH	YSGVHHFLSKRYNQRTDEYGGSLNRMRL		
	220	230	240
HADH_Native			
rHADH	RELLEDTLDECAGRAAVACRITVEEEIDGG		
	250	260	270
HADH_Native			
rHADH	ITREDIEGVLRELGELPDLWDFAMGSWEGD		

	280	290	300
HADH_Native	SVTSRFAPEGRQEEFVAGLKKLT	TKPVVGV	
rHADH	SVTSRFAPEGRQEEFVAGLKKLT	TKPVVGV	
	310	320	330
HADH_Native	GRFTSPDAMVRQIKAGILDLIGAARPSIAD		
rHADH	GRFTSPDAMVRQIKAGILDLIGAARPSIAD		
	340	350	360
HADH_Native	PFLPNKIRDGRLNLIRECIGCNICVSGDLT		
rHADH	PFLPNKIRDGRLNLIRECIGCNICVSGDLT		
	370	380	390
HADH_Native	MSPIRCTQNPSMGEEWRRGWHPERIRAKES		
rHADH	MSPIRCTQNPSMGEEWRRGWHPERIRAKES		
	400	410	420
HADH_Native	DARVLVVGAGPSGLEAARALGVRGYDVVLA		
rHADH	DARVLVVGAGPSGLEAARALGVRGYDVVLA		
	430	440	450
HADH_Native	EAGRDLGGRVTQESALPGLSAWGRVKEYRE		
rHADH	EAGRDLGGRVTQESALPGLSAWGRVKEYRE		
	460	470	480
HADH_Native	AVLAELPNVEIYRESPMTGDDIVEFGFEHV		
rHADH	AVLAELPNVEIYRESPMTGDDIVEFGFEHV		
	490	500	510
HADH_Native	ITATGATWRTDGVARFHTTALPIAEGMQVL		
rHADH	ITATGATWRTDGVARFHTTALPIAEGMQVL		
	520	530	540
HADH_Native	GPDDLFAGRLPDGKKVVVYDDDHYYLGGVV		
rHADH	GPDDLFAGRLPDGKKVVVYDDDHYYLGGVV		

	550	560	570
HADH_Native	AELLAQKGYEVSIVTPGAQVSSWTNNTFEV		
rHADH	AELLAQKGYEVSIVTPGAQVSSWTNNTFEV		
	580	590	600
HADH_Native	NRIQRRLIENGVARVTDHAVVAVGAGGVTV		
rHADH	NRIQRRLIENGVARVTDHAVVAVGAGGVTV		
	610	620	630
HADH_Native	RDTYASIERELECDTVVMVTARLPREELYL		
rHADH	RDTYASIERELECD A VVMVTARLPREELYL		
	640	650	660
HADH_Native	DLVARRDAGEIASVRGIGDAWAPGTIAAAV		
rHADH	DLVARRDAGEIASVRGIGDAWAPGTIAAAV		
	670	680	690
HADH_Native	WSGRRAAEFFDAVLPSNDEVPFRREVTQLA		
rHADH	WSGRRAAEFFDAVLPSNDEVPFRREVTQLA		

Figure 1.11. Sequence Alignment of native-HADH with rHADH

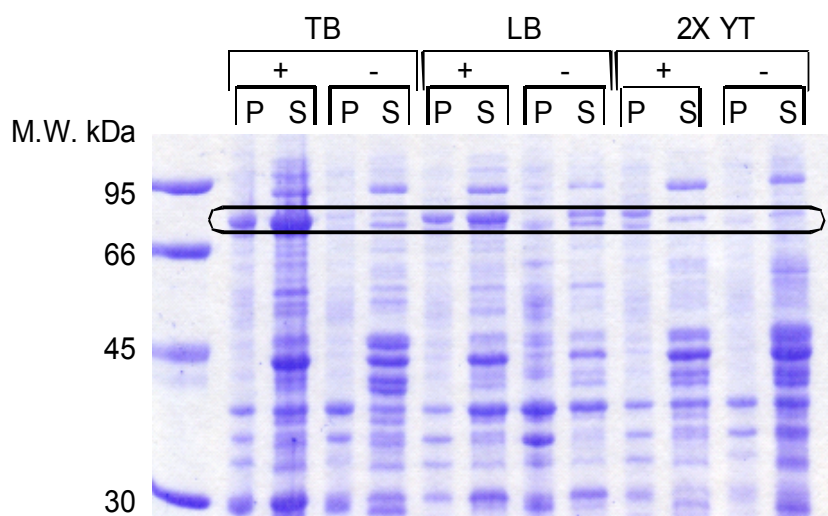


Figure 1.12. Optimization of HADH expression in Terrific Broth (TB), Luria-Bertani Media (LB), and 2X Yeast Extract Trypton (2X YT) with (+) and without (-) Isopropyl β -D-1-thiogalactopyranoside (IPTG). Highest expression was seen in TB media. P = Pellet, S = Supernatant

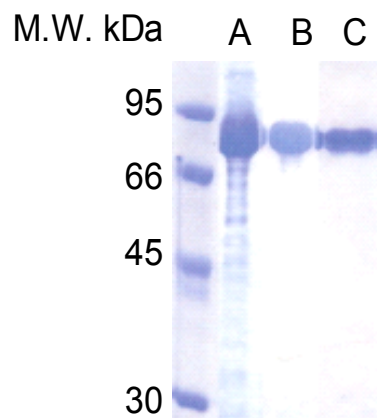


Figure 1.13. SDS-PAGE showing each stage of purification A) DEAE B) Butyl-Sepharose C) Size exclusion chromatography

close to 100%. The protein concentration was quantified with the BCA assay (Pierce) for a final yield of 10-20 mg/L protein. This expression system results in the highest yield of HADH in the literature and gives an ~ 40 fold increase from the native HADH. HADH activity was examined by the rate of reduction of DCPIP at 580 nm, with the specific activity of recombinant HADH being $40 \text{ mmol} \cdot \text{min}^{-1} \cdot \text{mg}^{-1}$ compared to $45 \text{ mmol} \cdot \text{min}^{-1} \cdot \text{mg}^{-1}$ of the native HADH.

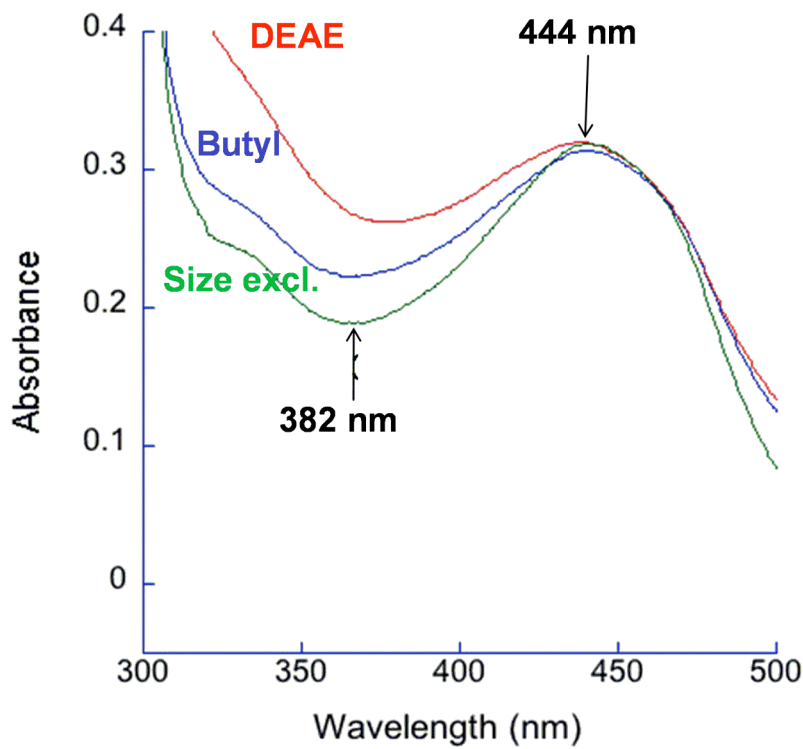


Figure 1.14. UV/Vis spectra of fractions collected after A) DEAE B) butyl-Sepharose C) size exclusion column. Ratios were calculated based on A444/A382 for determination of complete flavinylation

1.3.3. HADH Coupled Assay demonstrate activity of recombinant HADH (rHADH) is comparable as native HADH

It is necessary to prove the recombinant HADH behavior the same as the native HADH (Table 1.3). A coupled assay was employed to test the activity of the recombinant HADH against the native HADH. In the coupled assay, as HADH turns over histamine, the electrons are transferred to the redox mediator phenazine methosulfate, which transfers electrons to the DCPIP. The reduction of DCPIP demonstrates a bleaching effect at 580 nm and the rate of enzymatic activity is calculated. The K_m value obtained from the rHADH (38 μM) is in good agreement with native HADH (31 μM) (Figure 1.14). Table 1.3. demonstrates the similarities of rHADH with the native HADH.

	rHADH	Native HADH
hadh gene	2.1 Kb	2.1 Kb
SDS-PAGE gel	76 kDa	76 kDa
Specific Activity	40 $\text{mmol} \cdot \text{min}^{-1} \cdot \text{mg}^{-1}$	45 $\text{mmol} \cdot \text{min}^{-1} \cdot \text{mg}^{-1}$
K_m	38 μM	31 μM

Table 1.3. rHADH and native HADH comparison

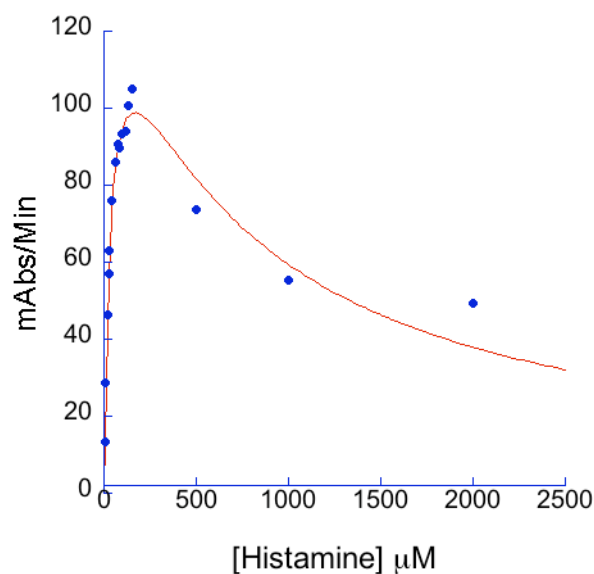


Figure 1.15. HADH coupled Assay with histamine

1.4. Discussion

1.4.1. The Cloning of HADH in pET21b Vector Achieves Expression of Soluble Protein.

Previous efforts in the Limburg lab to establish a recombinant expression for HADH produced mostly insoluble protein. Attempts were made with the *hadh* gene in pDEST expression vector transfected into *E. coli* for soluble protein. Inoculation with and without IPTG and glucose only led to insoluble protein. The amplification of the *hadh* gene proved to be challenging as the GC-rich nature of the gene increased the melting point. Longer run time and the addition of GC-rich PCR system reaction buffer and nucleotide mix successfully amplified the *hadh* gene. The amplified gene was

ligated into pUC19 with restriction enzymes XbaI and EcoRI. The sequence alignment with the native HADH demonstrated excellent agreement with only three polymorphism (Val60, Val78, and Ala615). These three amino acid residues are not involved in the active site. Difficulty followed with inserting the *hadh* gene into the expression vector pET21b. Several different restriction enzymes were employed for ligation into the vector. NdeI and XbaI both prove unsuccessful as demonstrated by 1% agarose gel, along with NdeI and HindIII. The restriction enzymes, NdeI and EcoRI, were able to properly ligate the gene into pET21b. The pET21b/*hadh* construct was transformed into *E.coli* Rosetta cells. The protein expression was optimized with TB media. This result correlates well with the growth conditions found in the initial screening of *N. simplex*.²² The cell growth in histamine-glycerol media expressed the highest HADH activity.

1.4.2. The Expression of Soluble rHADH yields high yield (~20 mg/L protein) and High Purity for X-ray Crystallography.

The prerequisite of kinetic and crystallographic studies on rHADH are high expression of pure and fully flavinated protein. The induction of pET21b/*hadh* construct in Rosetta cells produced soluble protein in high yield of 10-20 mg/L. The rHADH protein was purified with anion exchange (DEAE), hydrophobic (butyl), and size exclusion column chromatography. After each column purification, fractions were collected and the extent of flavination was evaluated. Each fraction was plotted against the Abs₄₄₄/Abs₃₈₂ ratio, which

demonstrated a bell shaped curve. Fractions were usually collected at the beginning to the end of the bell shaped curve. Most of the fractions after the size exclusion column chromatography showed full flavination and gave high purity with the Abs_{444}/Abs_{382} ratio greater than 1.35.

1.4.3. HADH Activity Assay demonstrate activity of rHADH is the same as native HADH

The activity assay revealed the activity of rHADH is identical to the native HADH, assuring that the kinetic study on rHADH represents that of native HADH. The activity assay was performed on rHADH and the K_m and specific activity were in good agreement with the native HADH. The assay also demonstrated substrate inhibition of rHADH, which is also seen with the native HADH.

1.5. Conclusion

Expression and purification of rHADH resulted in highest yield reported in literature with ~ 100 % flavination. HADH is highly selective for histamine, and solving the crystal structure will further the understanding how the enzyme active site recognizes histamine specifically. The activity assay demonstrated that the rHADH behaves the same as the native enzyme. The recombinant expression of HADH should be able to be employed for mechanistic studies on electron transfer, substrate selectivity, and oxidative turnover. The crystal structure analysis of rHADH was pursued in hopes of understanding the structure/function correlation of HADH, in particular the

histamine selectivity of HADH. The following chapter will discuss crystallization, structural determination, and the structural analysis of rHADH.

References

- (1) Harrison, P. *Metalloproteins*; Houndmills, Basingstoke, Hampshire : Macmillan, 1985.
- (2) Liddington, R., Derewenda, Z., Dodson, E., Hubbard, R., Dodson, G. *J. Mol. Biol.* **1992**, 228, 551-579.
- (3) Borgstahl, G. E., Parge, H.E., Hickey, M.J., Beyer Jr., W.F., Hallewell, R.A., Tainer, J.A *Cell* **1992**, 71, 107.
- (4) Reitzer, R., Gruber, K., Jogl, G., Wagner, U.G., Bothe, H., Buckel, W., Kratky, C. *Structure Fold. Des.* **1999**, 7, 891-902.
- (5) "<http://www.rcsb.org/pdb/home/home.do>", P. D. B.
- (6) Whittaker, M., Floyd, C., Brown, P., Gearing, A., *Chem. Rev.* **1999**, 99, 2735.
- (7) Overall, C., Lopez-Otin, C., *Nat. Rev. Cancer* **2002**, 2, 657.
- (8) Coussens, L., Fingleton, B., Marisian, L., *Science* **2002**, 295, 2387.
- (9) Mann, S. *Biomimetic materials chemistry*; VCH: New York, 1996.
- (10) Medina, M. A.; Urdiales, J. L.; Rodriguez-Caso, C.; Ramirez, F. J.; Sanchez-Jimenez, F. *Crit. Rev. Biochem. Mol. Biol.* **2003**, 38, 23-59.
- (11) Haas, H. L.; Wolf, P. *Iontophoresis Transm. Mech. Mamm. Cent. Nerv. Syst., Proc. Satell. Symp.* **1978**, 444-6.
- (12) Barocelli, E.; Ballabeni, V. *Pharmacological Research* **2003**, 47, 299-304.
- (13) Shin, N.; Coates, E.; Murgolo, N. J.; Morse, K. L.; Bayne, M.; Strader, C. D.; Monsma, F. J., Jr. *Molecular Pharmacology* **2002**, 62, 38-47.
- (14) Ligneau, X.; Morisset, S.; Tardivel-Lacombe, J.; Gbahou, F.; Ganellin, C. R.; Stark, H.; Schunack, W.; Schwartz, J. C.; Arrang, J. M. *Br. J. Pharmacol.* **2000**, 131, 1247-1250.
- (15) Gantz, I.; DelValle, J.; Wang, L. D.; Tashiro, T.; Munzert, G.; Guo, Y. J.; Konda, Y.; Yamada, T. *Journal of Biological Chemistry* **1992**, 267, 20840-3.
- (16) Konkimalla, V. B.; Chandra, N. *Biochemical and Biophysical Research Communications* **2003**, 309, 425-431.
- (17) Morrow, J. D.; Margolies, G. R.; Rowland, J.; Roberts, L. J., 2nd *N. Engl. J. Med.* **1991**, 324, 716-20.
- (18) Loechel, C.; Basran, A.; Basran, J.; Scrutton, N. S.; Hall, E. A. *H. Analyst* **2003**, 128, 889-898.
- (19) Bao, L.; Sun, D.; Tachikawa, H.; Davidson, V. L. *Analytical Chemistry* **2002**, 74, 1144-1148.

- (20) Zeng, K.; Tachikawa, H.; Zhu, Z.; Davidson, V. L. *Analytical Chemistry* **2000**, *72*, 2211-2215.
- (21) Siddiqui, J. A.; Shoeb, S. M.; Takayama, S.; Shimizu, E.; Yorifuji, T. *Journal of Biochemistry, Molecular Biology and Biophysics* **2001**, *5*, 37-43.
- (22) Siddiqui, J. A.; Shoeb, S. M.; Takayama, S.; Shimizu, E.; Yorifuji, T. *FEMS Microbiology Letters* **2000**, *189*, 183-187.
- (23) Mewies, M.; McIntire, W. S.; Scrutton, N. S. *Protein Science* **1998**, *7*, 7-20.
- (24) Limburg, J.; Mure, M.; Klinman, J. P. *Archives of Biochemistry and Biophysics* **2005**, *436*, 8-22.
- (25) Roberts, P.; Basran, J.; Wilson, E. K.; Hille, R.; Scrutton, N. S. *Biochemistry* **1999**, *38*, 14927-14940.
- (26) Basran, J.; Sutcliffe, M. J.; Hille, R.; Scrutton, N. S. *Biochemical Journal* **1999**, *341*, 307-314.
- (27) Dunn, R.; Marshall, K.; Munro, A.; Scrutton, N., *FEBS Journal* **2008**, *275*, 3850-3858.
- (28) Basran, J.; Sutcliffe, M. J.; Scrutton, N. S. *Journal of Biological Chemistry* **2001**, *276*, 42887-42892.
- (29) Grant, K. L.; Klinman, J. P. *Biochemistry* **1989**, *28*, 6597-605.
- (30) Scrutton, N. S. *Natural Product Reports* **2004**, *21*, 722-730.
- (31) Pollegioni, L.; Blodig, W.; Ghisla, S. *Journal of Biological Chemistry* **1997**, *272*, 4924-4934.
- (32) Miller, J. R.; Edmondson, D. E. *Biochemistry* **1999**, *38*, 13670-13683.
- (33) Silverman, R. B.; Hoffman, S. J.; Catus, W. B., III *Journal of the American Chemical Society* **1980**, *102*, 7126-8.
- (34) Silverman, R. B. *Prog. Brain. Res.* **1995**, *106*, 23-31.
- (35) Rigby, S. E. J.; Hynson, R. M. G.; Ramsay, R. R.; Munro, A. W.; Scrutton, N. S. *Journal of Biological Chemistry* **2005**, *280*, 4627-4631.
- (36) Kay, C. W. M.; El Mkami, H.; Molla, G.; Pollegioni, L.; Ramsay, R. R. *Journal of the American Chemical Society* **2007**, *129*, 16091-16097.
- (37) Rohlf, R. J.; Hille, R. *J. Biol. Chem.* **1991**, *266*, 15244-52.
- (38) Pearlman, D. S. *Drugs* **1976**, *12*, 258-73.
- (39) Oppenheimer, J. J.; Casale, T. B. *Expert Opin. Investig. Drugs* **2002**, *11*, 807-817.
- (40) Barbosa, J. A. R. G.; Sivaraman, J.; Li, Y.; Larocque, R.; Matte, A.; Schrag, J. D.; Cygler, M. *Proc. Natl. Acad. Sci. USA* **2002**, *99*, 1859-1864.
- (41) Briganti, F.; Mangani, S.; Orioli, P.; Scozzafava, A.; Vernaglion, G.; Supuran, C. T. *Biochemistry* **1997**, *36*, 10384-10392.
- (42) Reynolds, J. L.; Akhter, J. A.; Magarey, C. J.; Schwartz, P.; Adams, W. J.; Morris, D. L. *Br. J. Surg.* **1998**, *85*, 538-41.

- (43) Nielsen, H. J.; Kikuchi, Y. *Adv. Biosci.* **1993**, 89, 319-34.
- (44) Henry, D. P.; Bowsher, R. R.; Verburg, K. M. *Scand. J. Gastroenterol.* **1991**, 180, 26-31.
- (45) Claeys-Bruno, M.; Vandenabeele-Trambouze, O.; Sergent, M.; Geffard, M.; Bodet, D.; Dobrijevic, M.; Commeyras, A.; Phan Tan Luu, R. *Chemometrics and Intelligent Laboratory Systems* **2006**, 80, 176-185.
- (46) Pessatti, T. L. P.; Fontana, J. D.; Pessatti, M. L. *Methods Mol. Biol.* **2004**, 268, 311-316.
- (47) Lim, L. W.; Shamala, N.; Mathews, F. S.; Steenkamp, D. J.; Hamlin, R.; Nguyen Huu, X. *Journal of Biological Chemistry* **1986**, 261, 15140-6.
- (48) Mewies, M.; Basran, J.; Packman, L. C.; Hille, R.; Scrutton, N. S. *Biochemistry* **1997**, 36, 7162-7168.
- (49) Massey, V.; Hemmerich, P. *Biochemical Society Transactions* **1980**, 8, 246-57.
- (50) Huang, L.; Rohlf, R. J.; Hille, R. *Journal of Biological Chemistry* **1995**, 270, 23958-65.
- (51) Mewies, M.; Packman, L. C.; Mathews, F. S.; Scrutton, N. S. *Biochemical Journal* **1996**, 317, 267-272.
- (52) Rohlf, R. J.; Hille, R. *J. Biol. Chem.* **1994**, 269, 30869-79.
- (53) Silverman, R. B. *Accounts of Chemical Research* **1995**, 28, 335-42.
- (54) Edmondson, D. E. *Xenobiotica* **1995**, 25, 735-53.
- (55) Kim, J. M.; Bogdan, M. A.; Mariano, P. S. *Journal of the American Chemical Society* **1993**, 115, 10591-5.
- (56) Basran, J.; Jang, M. H.; Sutcliffe, M. J.; Hille, R.; Scrutton, N. S. *J. Biol. Chem.* **1999**, 274, 13155-61.
- (57) DeLano, W. L. T. P. M. G. S. D. S., San Carlos, CA, USA.
- (58) Basran, J.; Mewies, M.; Mathews, F. S.; Scrutton, N. S. *Biochemistry* **1997**, 36, 1989-1998.
- (59) Miura, R.; Setoyama, C.; Nishina, Y.; Shiga, K.; Mizutani, H.; Miyahara, I.; Hirotsu, K. *Journal of Biochemistry (Tokyo)* **1997**, 122, 825-833.
- (60) Nagy, J.; Kenney, W. C.; Singer, T. P. *J. Biol. Chem.* **1979**, 254, 2684-8.
- (61) Jang, M. H.; Basran, J.; Scrutton, N. S.; Hille, R. *J. Biol. Chem.* **1999**, 274, 13147-54.
- (62) Basran, J.; Chohan, K. K.; Sutcliffe, M. J.; Scrutton, N. S. *Biochemistry* **2000**, 39, 9188-9200.
- (63) Wilson, E.; Huang, L.; Sutcliffe, M.; Mathews, S.; Hille, R.; Scrutton, N. *Biochemistry* **1997**, 36, 41-48.

- (64) Sussman, J. L.; Harel, M.; Frolow, F.; Oefner, C.; Goldman, A.; Toker, L.; Silman, I. *Science FIELD Full Journal Title: Science (New York, N.Y.)* **1991**, 253, 872-9.
- (65) Waksman, G.; Kominos, D.; Robertson, S. C.; Pant, N.; Baltimore, D.; Birge, R. B.; Cowburn, D.; Hanafusa, H.; Mayer, B. J.; et al. *Nature* **1992**, 358, 646-53.
- (66) Raine, A. R. C.; Yang, C.-C.; Packman, L. C.; White, S. A.; Mathews, F. S.; Scrutton, N. S. *Protein Science* **1995**, 4, 2625-8.
- (67) Doubleie, S. *Methods Enzymol.* **1997**, 276, 523-530.
- (68) Fujieda, N., Tsuse, N., Satoh, A., Ikeda, T., Kano. *Biosci. Biotechnol. Biochem.* **2005**, 69, 2459-2462.

Chapter 2

Crystal Structure Determination of Histamine Dehydrogenase from *Nocardioides Simplex*

2.1. Introduction

As stated in the previous chapter histamine dehydrogenase (HADH) is an amine oxidizing enzyme first isolated from cultures of *Nocardioides simplex*.¹ Limburg et al. pursued the cloning of the full length *hadh* gene from *N. simplex* in order to gain insight into the nature of the redox active cofactors in the native HADH. Through sequence alignment, HADH showed high similarity with several flavoproteins, most notably TMADH.² Further spectroscopic studies confirmed an [4Fe-4S] and 6-S-Cys-FMN as the cofactors involved in oxidation of histamine.² HADH is known to have high substrate selectivity towards histamine and bind histamine in the mono-protonated form.² Kinetic isotope effect also demonstrated that C-H bond cleavage is partly rate limiting. To understand the narrow substrate selectivity and oxidation reaction, structural studies were performed on rHADH. The crystal structure of rHADH could provide an opportunity to define how the enzyme active site contributes to the histamine selectivity. Modeling of histamine in the active site of rHADH suggests important residues involved in the binding of histamine in rHADH. Such a knowledge could also provide a better understanding of the physiological binding of histamine within human

histamine receptors (HHR). The sequence of all four HHR is known, but none of the crystal structures have been determined.³⁻⁷ Modeling studies of HHR, along with other histamine binding proteins, have helped provide insight into how histamine binds within its natural receptor, which could aid in the design of antihistamines. The active site structure of rHADH may provide information for the mechanism of C-H bond cleavage, which remains unclear for many flavoproteins.⁸ One important enzyme where the mechanism of C-H bond cleavage is uncertain is the FAD containing flavoprotein monoamine oxidase (MAO).⁹⁻¹¹ This enzyme is involved in the breakdown of important biogenic amines in the body including, dopamine, serotonin, and norepinephrine. The substrates of MAO and HADH are very similar in chemical structure. Probing the mechanism of HADH could potentially reveal a clearer understanding of substrate oxidation in MAO and other flavoproteins.

In addition, the histamine selectivity of HADH may allow it to be used in a histamine biosensor.² When considering biosensor design, several conditions must be met.¹²⁻¹⁴ The first is exclusive selectivity for the substrate of analytical interest. The second is the ability of the enzyme to facilitate electron transfer between the enzyme and the electrode. Dehydrogenases are preferred over oxidase as they can be used under O₂ limited conditions.

The determination of the rHADH crystal structure can be used to evaluate and confirm the presence of the redox active cofactors, the residues involved in binding of substrate, and mechanism of substrate oxidation

presented by Limburg et al.² In this study, we were able to solve the crystal structure of HADH to 2.7 Å. Structural similarities and differences that distinguish HADH from TMADH will be discussed, with emphasis on the histamine binding site. Modeling studies of neutral and mono-protonated histamine were performed to gain insight into how the active site is arranged to gain selectivity for histamine.

2.2. Materials and Methods

2.2.1. Crystallization

Prior to crystallization, protein was concentrated to 20 mg/mL in 50 mM Tris-HCl buffer (pH 7.4) containing 0.15 M KCl. Screening of crystallization conditions was performed by the hanging-drop vapor-diffusion method using commercially available sparse matrix screening kits (Hampton Research and Emerald Biosystems). Equal volumes of protein and reservoir solution (1 µL + 1 µL) were mixed and equilibrated against 750 µL reservoir solution at 293 K. After 5 days, yellow crystals appeared in the three following conditions: 0.4 M NaH₂PO₄, 1.6 M K₂HPO₄, 0.1 M imidazole pH 8.0, and 0.2 M NaCl (Emerald Biosystems #20); 2.0 M (NH₄)₂SO₄, 0.1 M CAPS, pH 10.5, and 0.2 M Li₂SO₄ (Emerald Biosystems #33); and 2.0 M (NH₄)₂SO₄, 0.1 M Hepes pH 7.5, and 2% PEG (Hampton Research #39). Each of these commercial solutions were replicated from reagents in the, but only #33 was able to reproduce crystals. Sharp needles and square box shaped crystals were mostly observed with the Hampton Research #39 crystallization condition

solution. Concentrations of protein from 20 to 5 mg/mL were screened for optimization of crystal growth. Initial testing and handling of these crystals proved difficult, exposure to the atmosphere with opening the well and the addition of various cryoprotectants would dissolve the crystals or the crystal lattice would crack, resulting in poor diffraction patterns. Crystals were then grown in 2.0 M $(\text{NH}_4)_2\text{SO}_4$, 0.1 M Hepes pH 7.5, and 2% PEG (Hampton Research #39) with the addition of 2%-4% glycerol (v/v) to aid in the addition of the cryoprotectant. Crystals were frozen in liquid nitrogen in a solution of mother liquor (2.0 M $(\text{NH}_4)_2\text{SO}_4$, 0.1 M Hepes pH 7.5, and 2% PEG (Hampton Research #39)) and 25% glycerol as a cryoprotectant.

2.2.2. Data collection and processing

Initially unsubstituted HADH crystals were screened for X-ray diffraction in-house on an R-Axis IV++ detector with Cu $K\alpha$ X-rays generated by a Rigaku RU-H3RHB rotating-anode generator and focused using an Osmic confocal optical system (Rigaku, Japan) at the KU Protein Structure Laboratory. A full data set was collected, but initial attempts at molecular replacement using the TMADH structure (PDB 1DJN)¹⁵ as a search model were not successful due to the complexity of the screw axis in the crystal lattice. Subsequently, SeMet-HADH crystals which were generated with HADH grown in the presence of L-SeMet, were screened, and a complete MAD data set was collected at beamline BL9-2 at the Stanford Synchrotron Radiation Laboratory (SSRL) using the Stanford Automated Mounting (SAM)

system.¹⁶ Data collection was performed at 100 K using an oscillation angle of 1° per frame over a total of 270° to yield a highly redundant data set. The diffraction data was processed with MOSFLM¹⁷ and scaled with SCALA from the CCP program suite.¹⁸

2.2.3. Refinement and Validation

The model was refined using the data set to 2.7 Å resolution using iterative round of refinement with REFMAC²⁰ and model building performed with COOT.²¹ The structure was validated using PROCHECK²² and WHATIF.²³ All figures were prepared using PyMOL.²⁴

2.2.4. Histamine Modeling

The ligands were sketched in SYBYL²⁵ and refined via molecular mechanics optimization using the Tripos Force Field²⁶ and Gasteiger-Marsili electrostatics.²⁷ The ligands were docked into the HADH receptor via FlexX²⁸ retaining for explicit consideration all residues and crystallographically resolved heteroatomic moieties within 8.0 Å of the receptor center. All other docking controls were left at default setting.

2.3. Results

2.3.1. The Screening of Crystal Growth Conditions for HADH Reveals Three Different Conditions that Produce HADH Crystals.

The process of protein crystallization for an new protein requires the screening of many conditions to produce well-ordered single 3-D crystals. HADH protein in 50 mM Tris-HCl buffer pH 7.4 containing 0.15 M KCl with a

concentration of 20 mg/mL was screened against possible crystallization solutions from Hampton Research Screening Crystal Screen Kits I and II (HRI and HRII) and Emerald Biosystems Screening Wizard Kits I and II (EBI and EBI). After a period of five days, crystals were obtained in EBI #20, EBI #33, and HRI #39. All crystals were yellow due to the 6-S-Cys-FMN, which made distinguishing protein from salt crystals very easy. Both EBI #20 and EBI #33 yielded small crystals with small two-dimensional plates growing in EBI #33 (Figure 2.1). Both were well separated with slight birefringence but were too small for preliminary diffraction. Homemade solutions of both EBI #20 and EBI #33 were prepared in attempt to improve crystal quality. Small, 2-D, urchin-like crystals were observed in EBI #33 (Figure 2.2), but further efforts were focused on HRI #39 because these crystals produced 3-D chunky yellow crystals and long needle like crystals (Figure 2.3). After 11 days of growth, the crystals had good birefringence with a regular surface on many crystals. When protein concentrations were screened from 20 mg/mL to 2 mg/mL, crystals of similar morphology were observed.

2.3.2. The Screening of Cryoprotectants for X-ray Data Collection

Reveals the Need to Grow Crystal in 2-5% Glycerol for Stability.

The benefit of collecting an X-ray data set with a crystal flash cooling in a cryoprotectant is to avoid the formation of ice crystals in the flash cooling process. Various cryoprotectants were tested to optimize the diffraction quality. Both 30% glycerol and 25% PEG 400 were initially tested since these

A)



B)



Figure 2.1. Screening hits for Emerald Biosciences Crystal Kit #1 A) #20 - 0.4 M NaH_2PO_4 /1.6 M K_2HPO_4 , 0.1 M Imidazole pH 8.0, 0.2 M NaCl B) #33 2.0 M $(\text{NH}_4)_2\text{SO}_4$, 0.1 M CAPS, pH 10.5, 0.2 M Li_2SO_4



Figure 2.2. Homemade solution of Emerald Biosciences Crystal Kit #33 2.0 M $(\text{NH}_4)_2\text{SO}_4$, 0.1 M CAPS, pH 10.5, 0.2 M Li_2SO_4 .

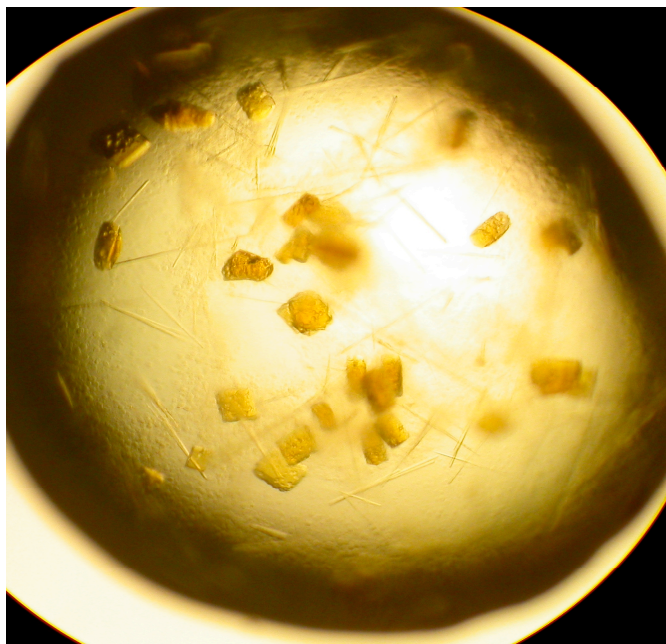


Figure 2.3. Hampton Research Crystal Screen Kit 1 #39 2.0 M $(\text{NH}_4)_2\text{SO}_4$, 0.1 M Hepes, pH 7.5, 2% PEG.

compounds are known to provide a glassy surface in the flash cooling process, but many crystals appeared to visually dissolve or gave poor diffraction patterns. Cryoprotectants containing the mother liquor with 30% sucrose, 30% glucose, 30% ethylene glycol, and 30% 2-methyl-2,4-pentanediol were tested with similar results. Efforts with capillary mount also proved to give little diffraction due to the crystal drying and dissolving with

exposure to the atmosphere. Initial tests were performed with 25% PEG-400; since the crystallization solution contained 2% PEG-400. It was reasoned that the addition of higher concentration of PEG might minimize the damage to the crystal lattice with PEG-400 already in solution, but this proved also to dissolve the crystal. The growth of the crystal in another cryoprotectant was then applied to glycerol, which demonstrated the best diffraction pattern during cryoprotectant screening. rHADH protein solutions were grown in HRI #39 with the addition of 2-6% glycerol. Within 2-3 days, crystal growth was observed in the 2-4% glycerol and growth was seen in 5-6% glycerol 5-6 days later. The crystals consisted of medium to large size crystals that were of two morphologies: long and slender rods (walking stick) and flattened squares (pizza box) (Figure 2.4). Freezing in 25% glycerol as a cryoprotectant resulted in good diffraction and no observable dissolving of the crystal.

2.3.3. Expression of SeMet Incorporated rHADH for the Purpose of Collecting MAD Data Set for Crystallography

Expression and purification of SeMet-incorporated rHADH was performed in order to collect a MAD data set for phase determination. Cell growth in SeMet media was stunted, with an additional 5-20 hours were needed to reach $OD_{600} = 0.7$. Longer time was also needed for cell growth in a second prep, which involved an additional 30 $\mu\text{g}/\text{mg}$ L-SeMet and the added step of spinning down and washing the starter culture cells with SeMet media. Purity and flavination, as observed by SDS-PAGE and absorbance



Figure 2.4. Hampton Research Crystal Screen Kit 1 #39 2.0 M $(\text{NH}_4)_2\text{SO}_4$, 0.1 M Hepes, pH 7.5, 2% PEG. Common crystal morphology of walking sticks and pizza boxes.

spectra closely resemble the expression of wild-type rHADH. A slight decrease in $\text{Abs}_{444}/\text{Abs}_{382}$ ratio of 1.37 was observed in the SeMet-rHADH, along with a 10-fold decrease in protein yield, though activity was found in good agreement with the wild-type HADH. Incorporation of SeMet into rHADH was observed with MALDI-TOF mass spectrometry. The first prep incorporated 10 out the 13 L-Met as L-SeMet (Figure 2.5). A second attempt for full incorporation of SeMet into rHADH was performed by doubling the L-SeMet concentration and removing the LB media before inoculation into expression media. This resulted in slower growth of the cells and a reduced

incorporation of 5 out of 13 L-Met residues replaced by L-SeMet as observed by MALDI-TOF mass spectrometry (Figure 2.6).

2.3.4. Complete Data Set Collected for the SeMet-rHADH at the Stanford Synchrotron Radiation Laboratory (SSRL)

Initial SeMet-rHADH crystal screening was performed on the in house X-ray diffraction. Crystal samples were grown in HRI #39 with 4% glycerol for screening on the house source X-ray diffraction. Collection of the data set suggested the crystals belong to the orthorhombic space group $P2_12_12_1$ with unit-cell parameters $a = 101.1411$, $b = 107.0355$ and $c = 153.3517$ (Table 2.1). Each asymmetric unit contained two molecules of HADH and had a Matthews coefficient of 60%. Initial attempts with molecular replacement were unsuccessful using the TMADH structure as a search model (PDB 1DJN).¹⁵ Efforts were subsequently directed towards solving the structure with an multiwavelength anomalous diffraction (MAD) data set. Two SeMet-HADH protein preps were generated yielding protein with partial incorporation of 10/13 and 5/13 L-SeMet. L-SeMet-HADH crystals were grown in HRI #39 with 2-5% glycerol with no change in crystal morphology. A complete MAD data set was collected at beamline 9-2 at the SSRL. The X-ray diffraction data was collected with 99.7 completeness to 2.7 Å resolution (Figure 2.7) and an R_{sym} value of 16% (Table 2.1). The data set was highly redundant (9.7) with 451,076 points collected and 46,309 unique reflections. This data set was high enough quality to solve the structure by molecular replacement

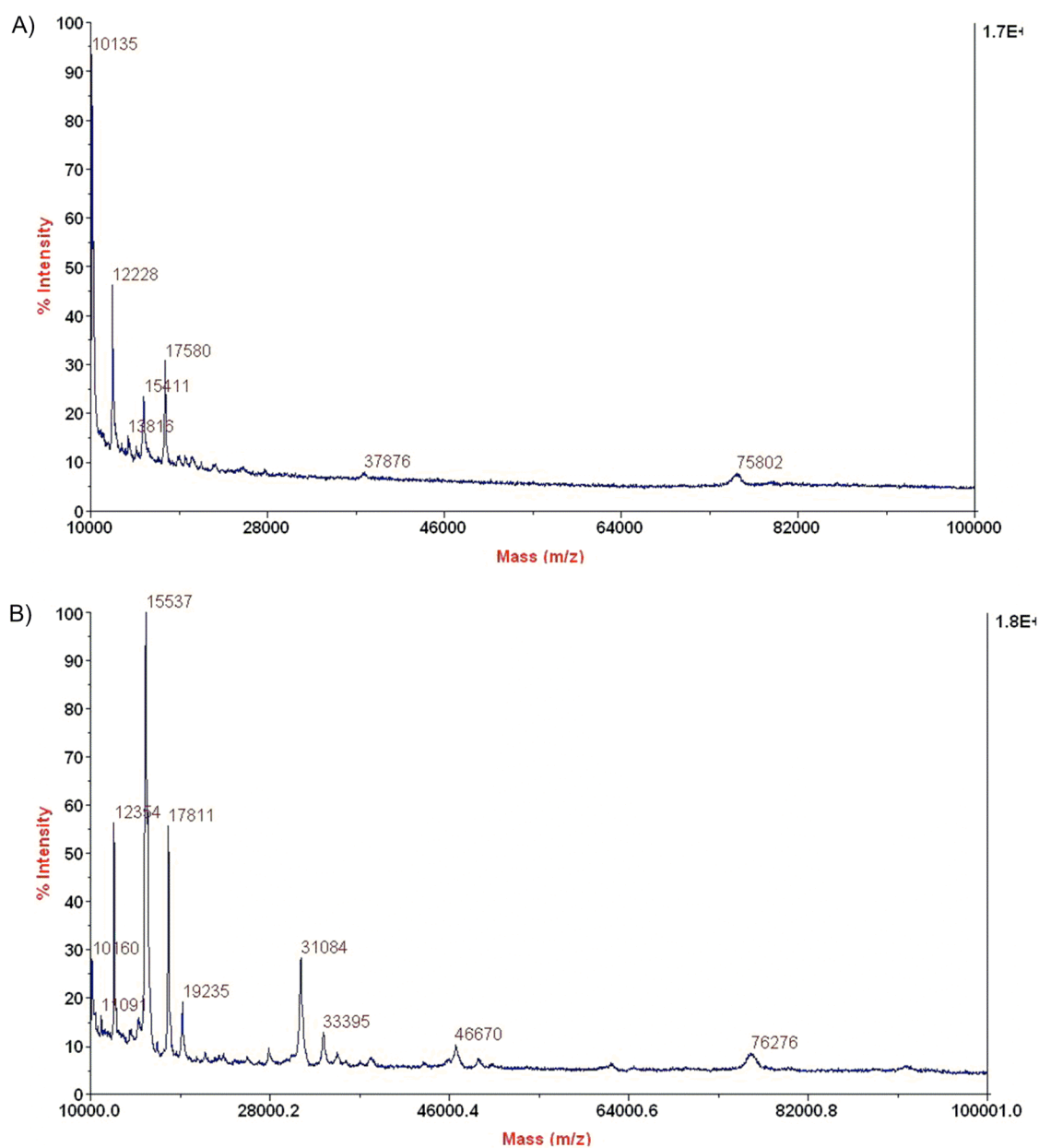


Figure 2.5. Mass spectrum (MALDI-TOF) of A) unsubstituted rHADH and B) SeMet incorporated rHADH. 10 of 13 Met were incorporated with SeMet

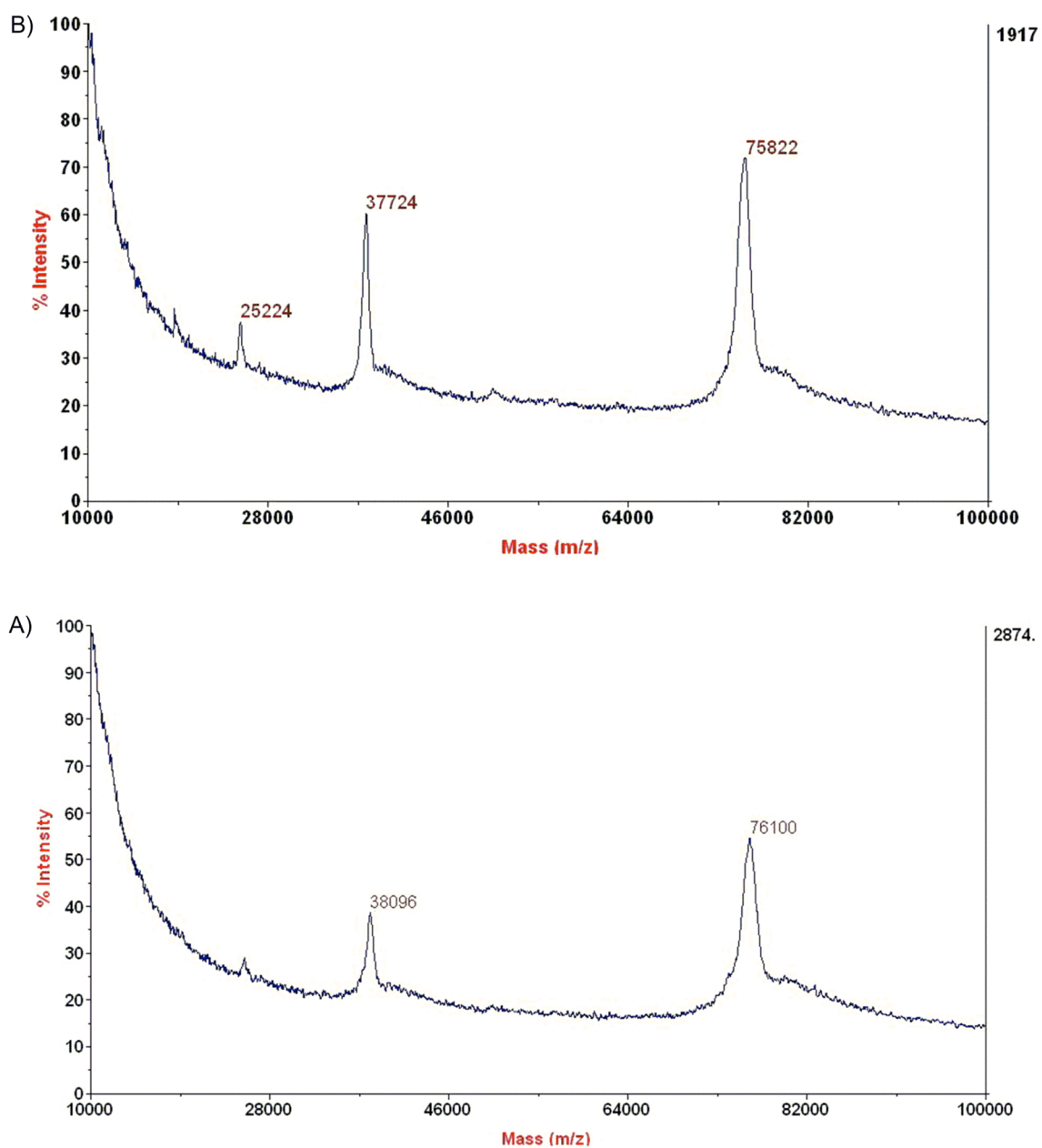


Figure 2.6. Mass spectra (MALDI-TOF) of A) unsubstituted rHADH B) SeMet incorporated rHADH. Within the second prep, 5 of 13 Met were incorporated with SeMet.

Space group	P2 ₁ 2 ₁ 2 ₁
Unit-cell parameters (Å)	a = 101.14 b = 107.03 c = 153.35
Resolution (Å)	84.5 – 2.70 (2.77 – 2.70)
No. of measurements	451,076
No. of unique reflections	46,309
Redundancy	9.7 (9.2)
Completeness (%)	99.7 (98.8)
R _{sym} (%)	16.0 (38.5)
Average I/σ(I)	16.8 (6.3)

Table 2.1. X-ray data collection statistics for SeMet-rHADH. Values in parentheses are for the last shell.

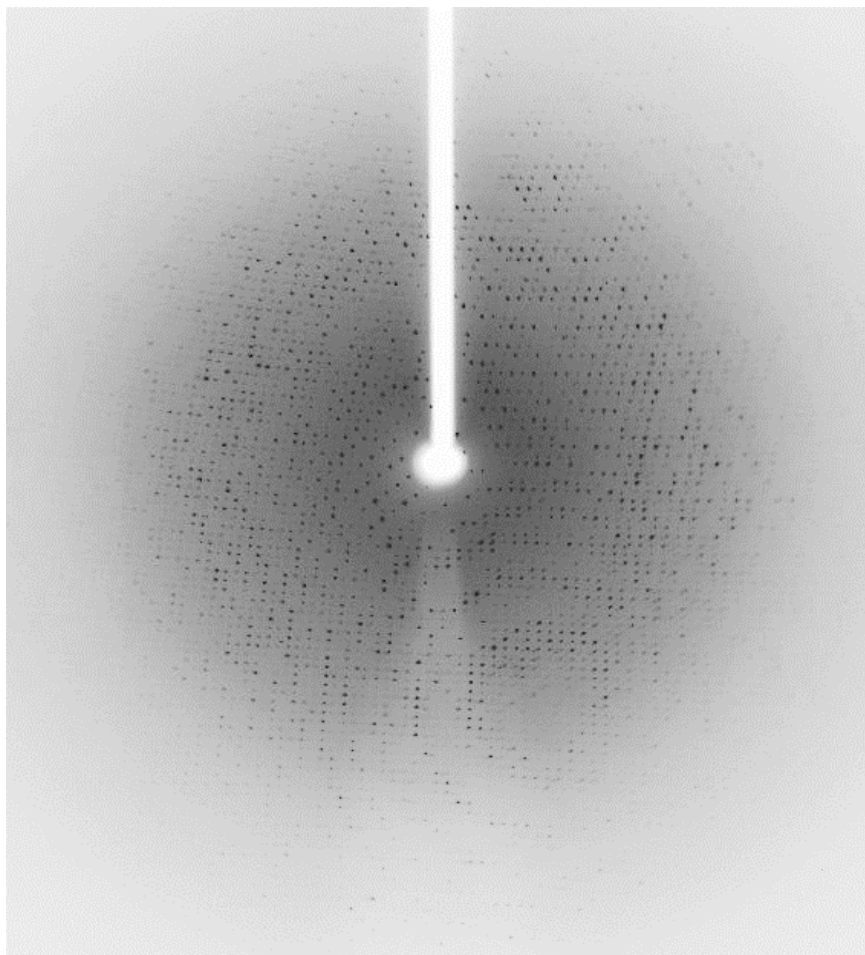


Figure 2.7. X-ray diffraction pattern of SeMet-rHADH at SSRL

using TMADH structure as a search model (PDB 1DJN).¹⁵ The HADH crystal structure was refined with Refmac and modeled with COOT.

2.3.5. rHADH Structure

Preparation of SeMet-rHADH followed previously described procedures.¹⁹ Activity of rHADH maintained activity as seen in native HADH

as described in chapter 1. The SeMet HADH crystal was refined at 2.7 Å with two molecules per asymmetric unit. The structure was validated using PROCHECK²² and WHATIF.²³ The Ramachandran plot showed 87.1% residues in most favored region, 12.4% in the additional allowed regions, 0.5% in the generously allowed and no residues in the disallowed region. Data refinement statistics are described in Table 2.2.

Rwork/Rfree(%)	19.7/25.3
B-factors	
Protein	21.7
6-S-Cys-FMN	4.40
[4Fe-4S]	20.86
ADP	17.18
RMSD	
Bond lengths (Å)	0.012
Bond angles (°)	1.463

Table 2.2. Refinement Statistics

2.3.6. The Overall Structure of rHADH

rHADH was crystallized as a homodimer with two molecules per asymmetric unit (Figure 2.8). Each subunit contains 690 residues with

molecule A modeled with residues 7-690 and molecule B modeled with residues 7-689. Both contain [4Fe-4S] and 6-S-Cys-FMN as redox active cofactors with the addition of a single ADP molecule per each subunit. Figure 2.9 shows the structure of each subunit of the homodimer with the prosthetic groups colored in red. The root mean square deviation (RMSD) for the C α between molecules A and B for rHADH is 0.34 Å. With the high structural similarity between both molecules, continued analysis will focus on molecule A due to the complete modeling the C-terminus. The molecule is comprised of four segments within three domains (Figure 2.9). The large domain contains the first segment of residues 7-385. The medium domain is comprised of the second segment of residues 386-491 and the last segment of residues 622-690, while the small domain consists of third segment of residues 492-621.

2.3.6.1. The Large Domain of HADH

The large domain contains an N-terminal TIM barrel (Figure 2.10) common to other flavoproteins, with the eight parallel β -barrels covered by the eight parallel α -helices. This domain contains the 6-S-cys-FMN and [4Fe-4S].³⁰ The 6-Scys-FMN is located at the opening of β -barrel and is surrounded by the 8-fold α -helices and large excursions at the end of β -

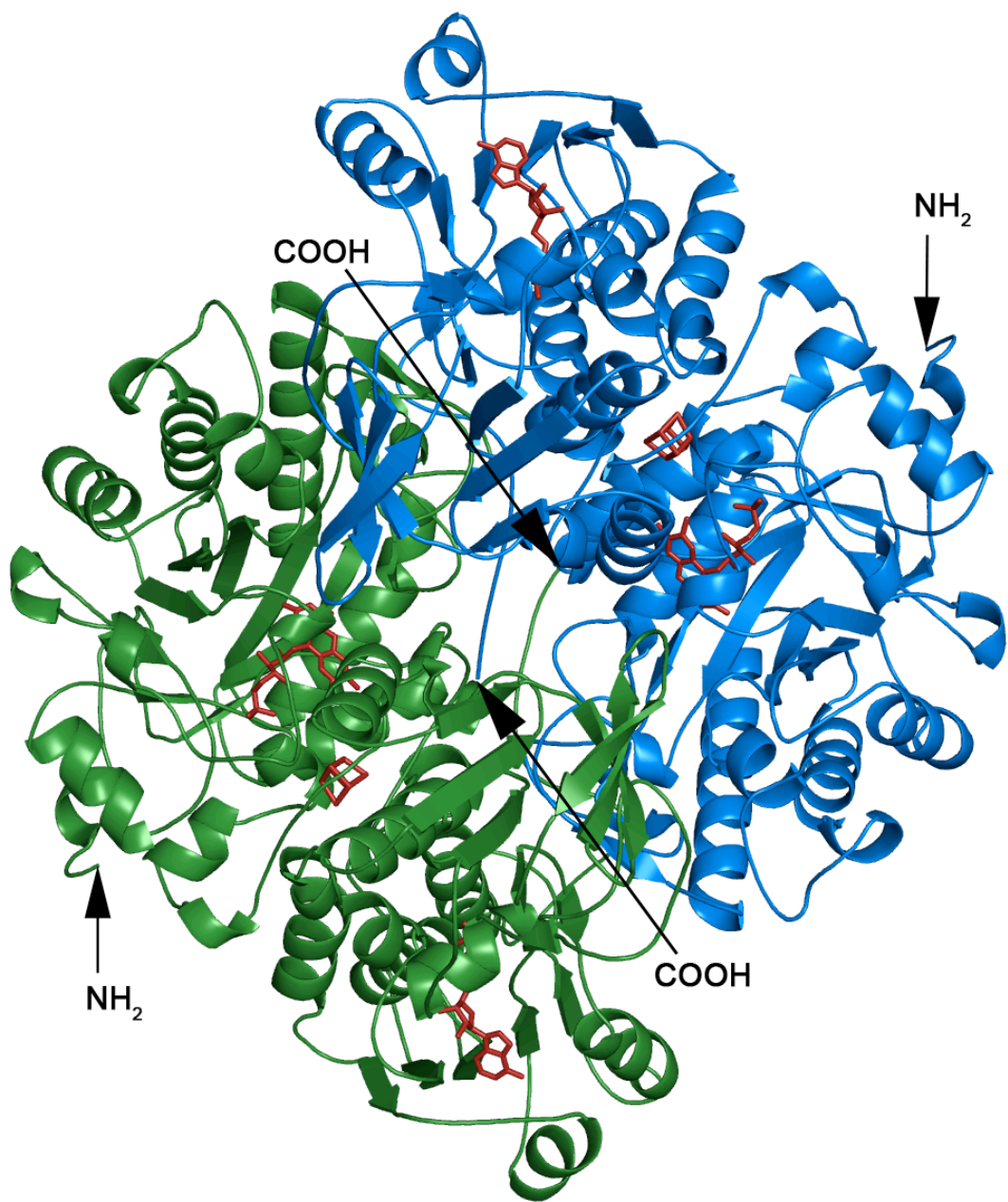


Figure 2.8. Overview of rHADH structure. Ternary Structure of rHADH with one dimer in green and the other in blue. The prosthetic groups are colored red within the molecule.

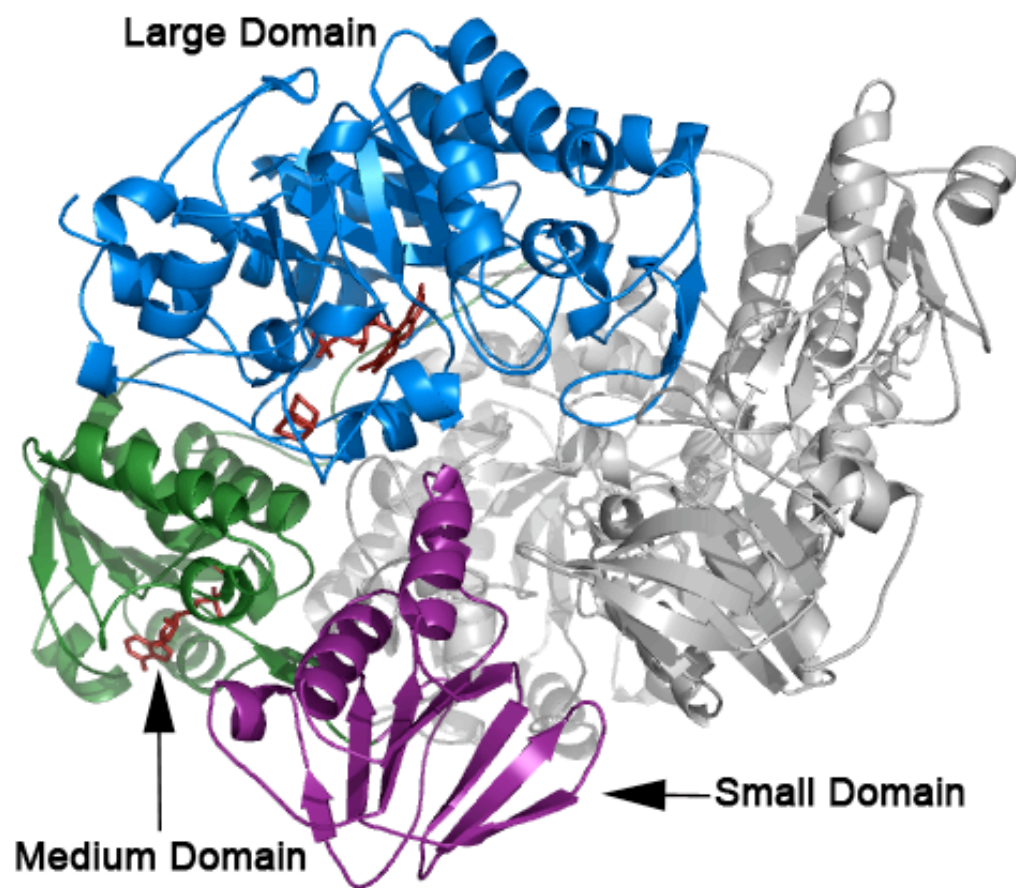


Figure 2.9. Individual domains of each subunit. The large domain is colored in blue, the medium is colored in green, and the small domain is colored in purple. The prosthetic groups are colored red within the molecule.

stands 2,3,4,6, and 8 of the barrel that serve to cover and bury the 6-S-Cys-FMN. The 6-S-Cys-FMN is covalently linked to Cys35 positioned after the first parallel strand of the β -barrel. The cysteine is linked to the 6-S-Cys-FMN through its C-6 atom, which is only known for two other flavoproteins.³¹ The [4Fe-4S] cluster is positioned outside the β/α -barrel and connected after the end of the parallel α -helix (helix 8) close to the medium domain. The [4Fe-4S] is coordinated to four cysteine residues (Cys348, Cys351, Cys354, and Cys366).

2.3.6.2. The Medium and Small Domains of rHADH

The medium domain is comprised of five α -helices that cover 3 parallel β -sheets, with three of the α -helices on one side and two on the other. The last 20 C-terminal residues of the fourth segment are in contact with the adjacent subunit. The ADP is located in the medium domain, but it is not covalently linked to any residue within the domain. The ADP is exposed to the surface, next to the interface of the medium and small domains. The small domain contains three α - helices that cover over five parallel β -sheets. Three-stranded anti-parallel β -sheets cover the other face.

2.3.7. Structural Comparison of HADH with TMADH

HADH shares structural homology with a large family of flavoproteins containing a TIM barrel domain.^{30,32-34} HADH is structurally most similar to the 6-S-Cys-FMN and [4Fe-4S] containing flavoprotein, TMADH.³⁴ The enzyme TMADH catalyzes the oxidative demethylation of trimethylamine to

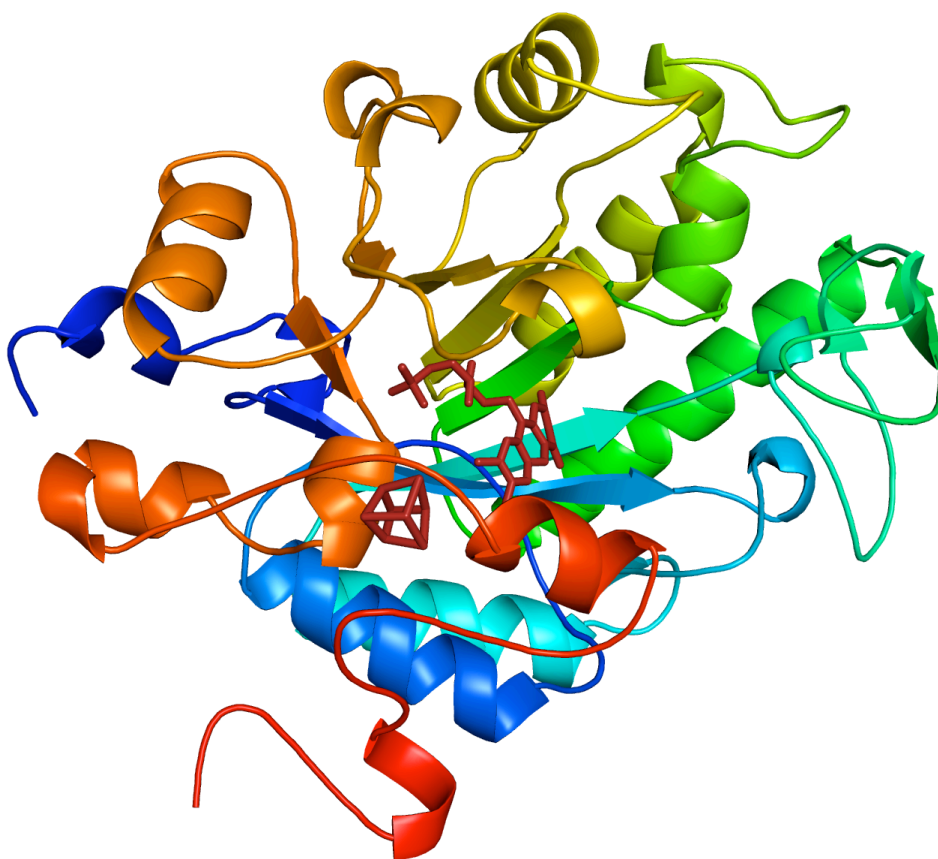


Figure 2.10. HADH large domain rainbow colored from N-terminus (blue) to C-terminus (red) demonstrating the TIM barrel. The prosthetic groups are also in red.

dimethylamine and formaldehyde.³⁵ Both the enzymes are homodimer in structure and are similar in size, 76 kDa and 82 kDa for HADH and TMADH respectively.^{2,35} Molecule A of HADH demonstrates high structural similarity with molecule A of TMADH based on the root mean square deviation of 1.15 Å for the C α atoms. Figure 2.11 shows the overlay of each molecule of HADH and TMADH. Both of the structures are comprised of four segments within three domains.³⁴ The large domain has the TIM barrel structural motif found in TMADH and in other flavoproteins.³²⁻³⁴ The medium and small domain secondary structures share similarities corresponding with the α helices and β sheets.³⁴ One main structural difference between HADH and TMADH is found in the small domain. In TMADH, a long loop is connected to the three anti-parallel β -sheets consisting of residues 606-631, which is not found in HADH. This loop in TMADH extends over the large domain in the adjacent molecule. This loop is also not found in the FMN and [4Fe-4S] *E. coli* 2,4-dienoyl-CoA reductase, which shares a 30% identity with TMADH.³⁰ The redox active cofactors, 6-S-Cys-FMN and [4Fe-4S] cluster, are positionally conserved in both HADH and TMADH, along with bound ADP in the medium domain.³⁴ The function of the bound ADP is unknown.² The bound ADP is spatially analogous with bound FAD in other flavoproteins, i.e. *E. coli* 2,4-dienoyl-CoA reductase.³⁰ In this flavoprotein, the FAD transfers electrons to the FMN through the [4Fe-4S], which will reduce the substrate by two electrons.

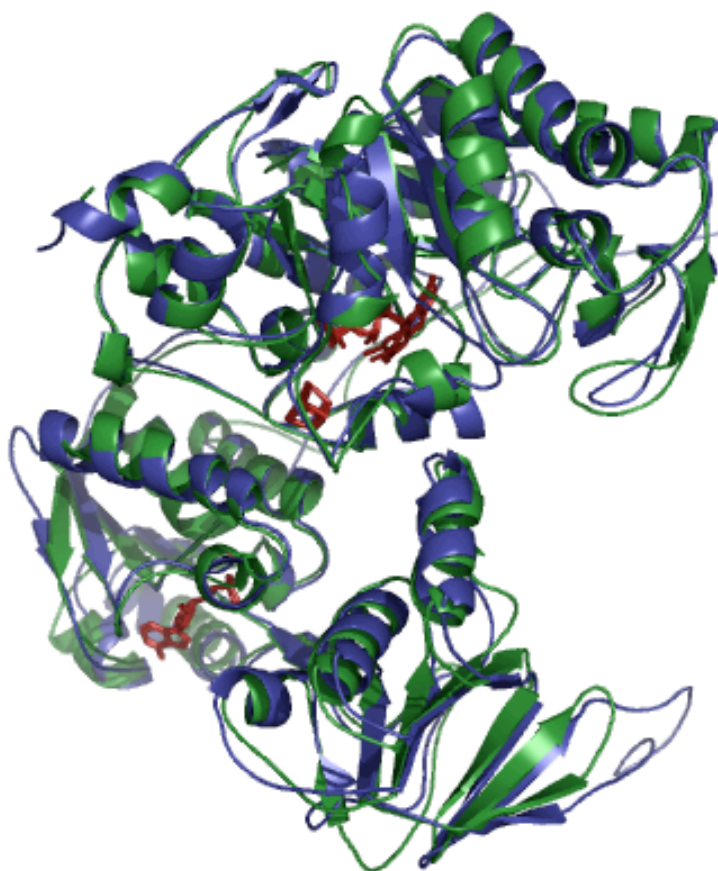


Figure 2.11. HADH subunit overlaid with TMADH. HADH molecule A (green) is overlaid with molecule B (blue) TMADH.

2.3.8. The Active Site of HADH

The prosthetic groups, 6-S-Cys-FMN and [4Fe-4S], in HADH are involved in the oxidation of histamine.² Both cofactors are found in the large domain of HADH, with the 6-S-Cys-FMN covalently linked to Cys35 and the [4Fe-4S] coordinated to four cysteine residues (Cys348, Cys351, Cys354, and Cys366)² (Figure 2.12). The distance of the 8 α -methyl of the 6-S-Cys-FMN to the closest iron is around 6 Å, while the closest cysteine residue is 4 Å away. The distances 8 α -methyl of the 6-S-Cys-FMN to the closest iron and cysteine are reasonably close to the distances of the 8 α -methyl of the 6-S-Cys-FMN to the closest iron and cysteine in TMADH based on overlay of both cofactors.³⁴ Within the active site, residues in HADH, Arg230, His179, and Tyr176 (HADH numbering) are conserved in TMADH. In TMADH, these residues are involved in substrate oxidation^{36,37} and in 6-S-Cys-FMN biogenesis.³⁸ Arg230 is positioned 2.70 Å from the O2 carbonyl of the 6-S-Cys-FMN, while Arg222 in TMADH is 2.60 Å from the carbonyl.³⁴ This residue was found in TMADH to stabilize the negative charge buildup on the N1 and C2 carbonyl during 6-S-Cys-FMN biogenesis in TMADH.³⁸ In HADH, Tyr176 is almost 1.0 Å further from the O2 carbonyl of 6-S-Cys-FMN, 3.72 Å in HADH and 2.80 Å in TMADH, but both are within hydrogen bonding distances to the N δ atom of the imidazole ring of the neighboring histidine (H179). The difference in Tyr and 6-S-Cys-FMN distance could influence the extent of the spin-spin coupling and explain the differences observed in

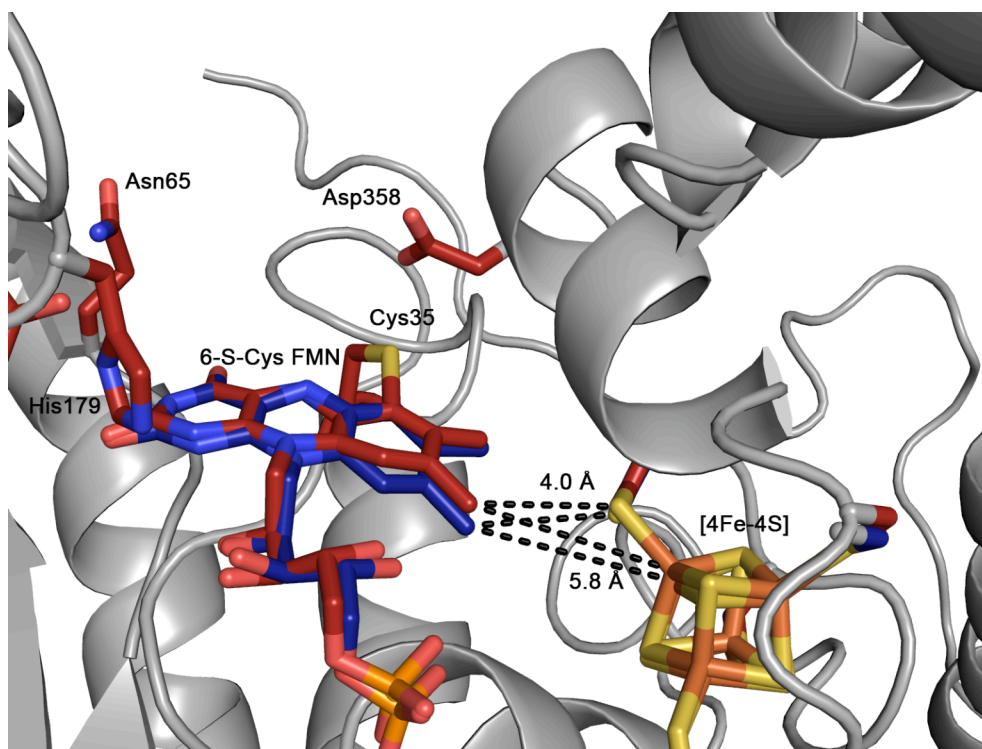


Figure 2.12. The prosthetic groups, 6-S-Cys-FMN and [4Fe-4S], in HADH (red) are involved in the oxidation of histamine. The cofactor distances for TMADH (blue) and HADH (red) from the FMN to closest cysteine and iron center is the same. Overlap was performed with SSM superimpose in Coot based on α chain of both proteins.

TMADH and in HADH.^{2,36} This tyrosine residue is also involved in hydrogen bonding with histidine residue and is proposed to be essential to lower the pK_a of histidine residue for substrate oxidation based on the mutation studies with TMADH.³⁶ His179 is around 0.5 Å closer to the 6-S-Cys-FMN than His172 is to the 6-S-Cys-FMN in TMADH. Through mutation studies, this histidine residue is believed to influence the upper ionization in the enzyme-

substrate complex of TMADH.³⁷ The 6-S-Cys-FMN in both HADH and TMADH exhibit a butterfly bend centered at the N5 and N10 positions (Figure 2.13). The figure demonstrates the bend in the 6-S-Cys-FMN of HADH (green) is not as extensive as the bend in TMADH (blue), while the purple 6-S-Cys-FMN of HADH was under planar constraint within the refinement process. The electron density of HADH suggests that the bend of the 6-S-Cys-FMN lies between the planar 6-S-Cys-FMN in the constrained refinement and the bend found TMADH. Experimentally, it was determined that the 6-S-Cys-FMN bend increased the two electron reduction potential of the 6-S-Cys-FMN.³⁹⁻⁴¹ This increase is in good agreement with the findings in this work, as the two-electron potential of TMADH is higher than HADH.⁴²

One of the major differences between HADH and TMADH is the substrate selectivity. The differences in substrate binding to TMADH and HADH are due to differences within the active site. In TMADH, substrate binds to the “aromatic bowl”.⁴³ The binding of substrate in TMADH involves cation- π bonding of the alkylammonium ion mediated by one tyrosine and two tryptophan residues. Only one tryptophan is conserved between these two enzymes in HADH, where the other two residues are substituted by glutamine and aspartic acid. These residues may provide insight for the selectivity of HADH for histamine versus TMADH and DMADH. Since the structure did not contain histamine, docking studies of histamine were undertaken to assist in understanding the enzyme’s selectivity.

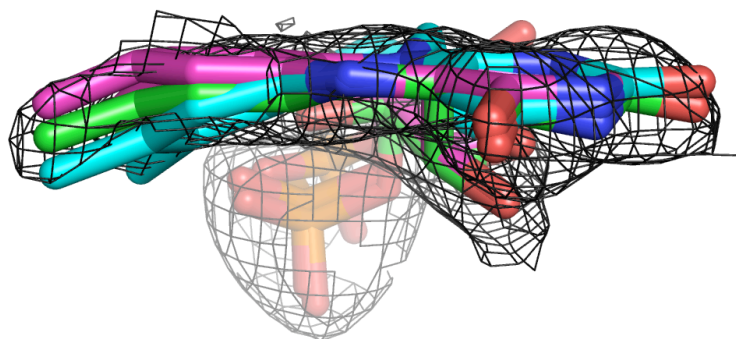


Figure 2.13. Butterfly bend structure of 6-S-Cys-FMN. Electron density shown as $2 |F_o| - |F_c|$ map at 1.0σ around the 6-S-Cys-FMN of strained refinement of HADH 6-S-Cys-FMN (purple), unstrained refinement of HADH 6-S-Cys-FMN (green), and TMADH (blue)

2.3.9. The Modeling of Histamine into the Active Site to Understand the Mode of Binding

To gain understanding of the substrate selectivity of HADH, histamine was modeled into the active site (Figure 2.14). The molecular model of histamine was docked into the active site in both the neutral and protonated

forms, with the cation predicted to be substantially more energetically favorable than the neutral species (-21.50 kcal/mol vs. -14.44 kcal/mol). The binding of histamine is characterized by several interactions that stabilize the enzyme-substrate complex. The histamine is positioned over the *si* face of the isoalloxazine ring (Figure 2.15). The negative charge of the Asp358 and Glu79 tightly binds the amino group of histamine. This salt bridge would provide exceptional stabilization for the amino group. The imidazole group of histamine forms π - π interactions with Tyr181 and Phe77. Tyr181 exhibits π -stacking interaction, with Phe77 forming end-on interactions with the imidazole group. Asn115 also contributes to the stabilization by hydrogen-bonding to the nitrogen of the imidazole ring.

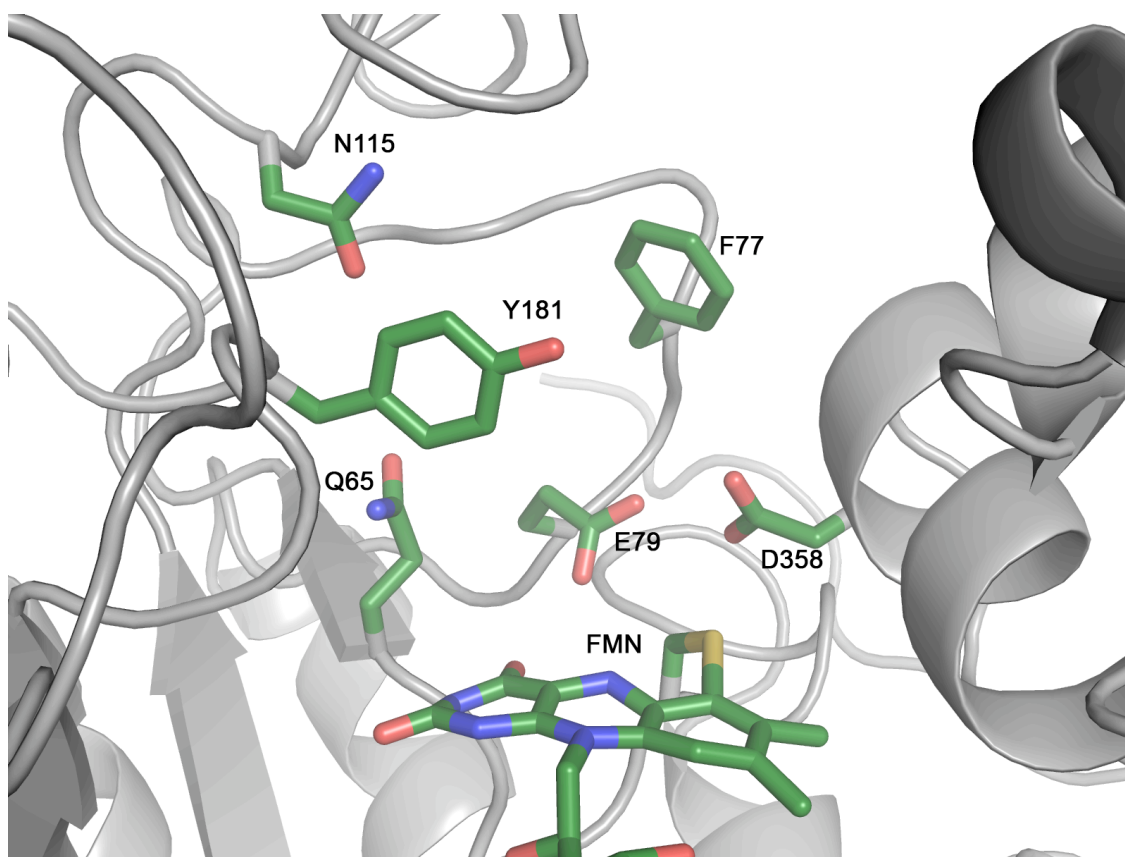


Figure 2.14. Putative histamine binding site.

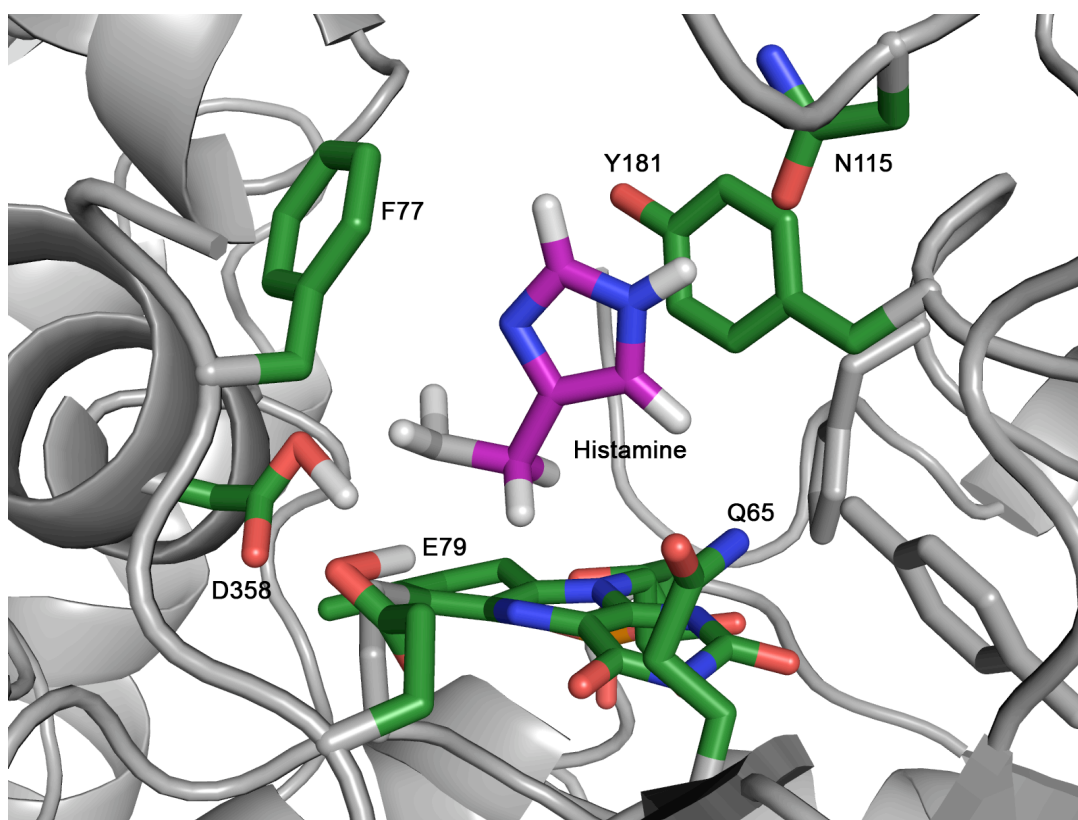


Figure 2.15. Model study on histamine binding in the active site of rHADH.

2.4. Discussion

2.4.1. Screening of Crystal Growth Conditions for HADH Reveals Three Different Conditions that Produce HADH Crystals

The process of protein crystallization requires the screening of many different conditions to produce crystals if conditions are not known. Hampton Research Screening Kits I and II (HRI and HRII) and Emerald Biosystems Screening Kits I and II (EBI and EBII) were used to identify the conditions of

crystal growth. Three different conditions were found to grow crystals within a week, EBI #20, EBI #33 and HRI #39. Minimal optimization of EBI #20 and EBI #33 were pursued, since the crystal morphology of HRI #39 produced the greatest potential for diffractable crystals in a short time period. Crystal morphology of HRI #39 did not vary with protein concentration, as 5 mg/mL to 20 mg/mL produced similar long rods and flatten square boxes crystal shapes. Initial HADH crystal screening was performed on the in house X-ray diffraction.

2.4.2. Screening of Cryoprotectants for X-ray Data Collection Reveals the Need to Grow Crystal in 2-5% Glycerol to Avoid Damaging the Crystal

The exposure of the crystal to the atmosphere and the initial addition of various cryoprotectants readily dissolved the crystal within minutes. Different approaches were then pursued to obtain a crystal that could be frozen and yield well-ordered diffraction. Gradually increasing the concentration of glycerol in 5% increments to the final concentration of 25% proved unsuccessful as the crystal would still dissolve in higher concentrations of the cryoprotectant. Efforts were then made to collect a data set at room temperature without cryoprotectant using a capillary mount. The challenge in this method is to avoid drying out the crystal during manual manipulation to a sealed capillary. The HADH crystals examined using this method did not yield a quality data set from this method but unclear if this was due to the crystal or the

manipulation. The introduction of cryoprotectant while the crystal is forming can reduce the damage to the crystal caused by the addition of cryoprotectant. Thus, before crystallization 2 – 6 % glycerol was added to the mother liquor. This did not change the crystal morphology of the walking sticks or pizza boxes. These crystals grown in this manner appeared unaffected when 25 % glycerol was added as a cryoprotectant. The crystals were mounted at the home source X-ray diffraction and obtain good diffraction data. Initial tests determined the HADH crystals belong to the orthorhombic space group $P2_12_12_1$ with unit-cell parameters $a = 101.1411$, $b = 107.0355$ and $c = 153.3517$ (Table 2.1). Each asymmetric unit contained two molecules of HADH. The Matthews coefficient V_M of $2.79 \text{ \AA}^3 \text{ Da}^{-1}$ which corresponds to a solvent content of 60%. Due to the high sequence identity and homology with TMADH (PDB 1DJN)¹⁵ this structure was used to attempt to solve the structure using molecular replacement. This method proved difficult and while other programs of molecule replacement were being pursued, SeMet HADH was prepared to obtain a MAD data set.

2.4.3. Expression of SeMet incorporated rHADH for the purpose of collecting MAD data set for X-ray crystallography

Since molecular replacement proved to be more difficult than expected, HADH protein was grown in SeMet rich media in which the heavy atom selenium is incorporated into the protein by replacing normal amino acid methionine with methionine in which the sulfur in the amino acid is substituted

with selenium. The anomalous scattering of the heavy atom can give the corresponding phase angle, which is then used to solve the crystal structure.⁴⁴ The initial attempt at SeMet incorporated 10 out of the 13 L-Met as L-SeMet into rHADH. A complete data collection was successfully collected at the SSRL and phasing using the incorporated SeMet was attempted using multiwavelength anomalous diffraction. It appeared that insufficient incorporation of SeMet caused problems for determining phase information although the number of SeMet was also high. A subsequent attempt at higher SeMet incorporation by the addition of higher concentration of L-SeMet during protein expression, only resulted in a reduction in the amount of SeMet incorporated (5 out of 13). However, the first SeMet data was of significantly higher quality compared to home source and was used for molecular replacement.

2.4.4. Complete Data Set collected for the SeMet-rHADH at the Stanford Synchrotron Radiation Laboratory (SSRL)

A complete MAD data set was collected at beamline 9-2 at the SSRL at the remote, peak, and edge of the X-ray absorbance of selenium. Screening of L-SeMet crystals showed higher order in longer, cuboid walking sticks rather than the flat, square box crystals. It also appeared that the best diffraction data could be collected with the crystal hanging out of the loop. (Figure 2.16).

HADH crystals were also grown with substrate in order to understand the binding of histamine with substrate bound (histamine) and inhibitor bound (N-methyl-histamine) with a five fold increase of inhibitor concentration to enzyme. The resulting crystals only consisted of pizza boxes, which we were unable to obtain reasonable diffraction. In the future, seeding the crystal solution of enzyme and histamine with microcrystals from the walking sticks could be used to influence the crystal morphology towards the diffractable walking sticks.

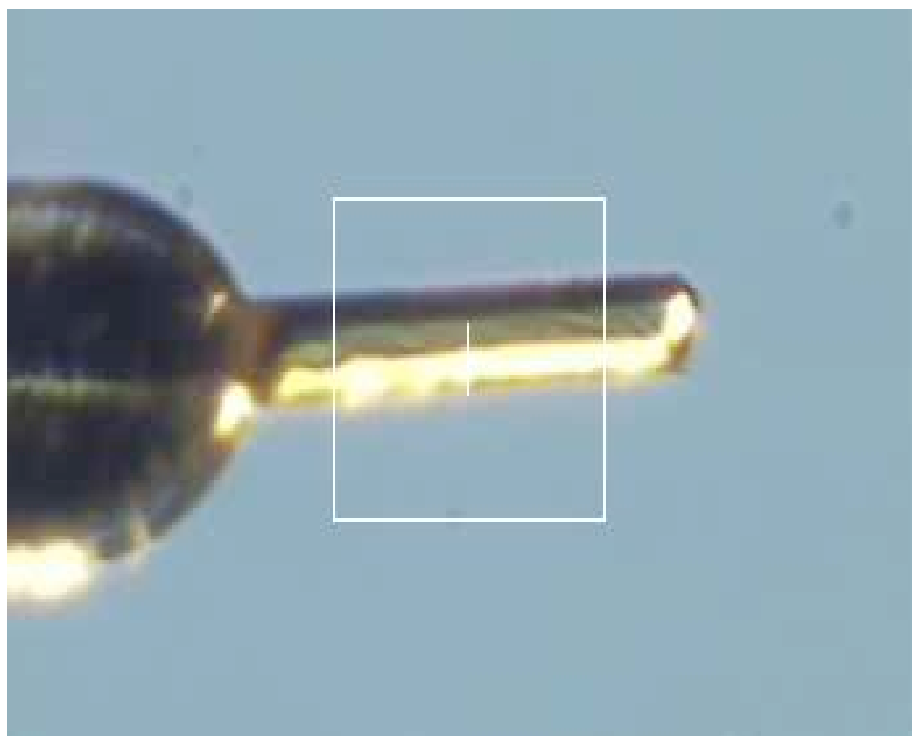


Figure 2.16. Data collection of HADH crystal hanging out of the loop

2.4.5. The Active Site of HADH

2.4.5.1. Active Site Comparison of HADH and TMADH

Many structural similarities exist between HADH and TMADH, but the difference in substrate specificity suggests a unique aspect of the active site of HADH. The crystal structure of HADH and modeling studies with histamine were performed in order to gain understanding of the substrate specificity of HADH. Only one of the residues in the aromatic bowl of TMADH (Trp267) is conserved in HADH.⁴⁵ With the polar residues Asp358, Glu79, Gln65, Tyr181, and Gln115, the binding pocket of HADH resembles that of histamine binding proteins (HBPs) and the proposed binding pocket of HHR³⁻⁷ rather than TMADH, which consists of the aromatic side chains (Tyr60, Trp264, and Trp355).⁴⁵ A distinct difference between TMADH and HADH is the substrate selectivity within the active site. The tertiary alkylammonium trimethylamine (TMA) in TMADH is bound through the organic cation- π bonding of the aromatic bowl, Tyr60, Trp264, and Trp355. Only one residue in HADH (Trp267) is conserved from the aromatic bowl of the TMADH, and the Trp267 residue is not responsible for the stabilization of histamine in HADH. Gln65 and D358 are the two other residues spatially conserved with the aromatic bowl. These polar residues stabilize the substrate through a salt bridge and hydrogen bonding, as opposed to the cation- π stabilization found in the aromatic bowl of TMADH with residues Tyr60 and Trp355.

2.4.5.2. The Mechanism Biogenesis of 6-S-Cys-FMN in HADH Could Resemble TMADH Based on Spatially Conserved Arginine Residue in the Active Site

Within the active site of HADH, Arg230 is spatially conserved with Arg222 in TMADH (Figure 2.17). Mutation studies in TMADH³⁸ have revealed that Arg222 is involved in the 6-S-Cys-FMN biogenesis in which the Cys30 is covalently linked to the C6 position on the flavin isoalloxazine ring. In the proposed mechanism, the 6-S-Cys-FMN forms through flavin tautomerization.³⁸ In the flavin iminoquinone methide tautomer, the C6 atom of the flavin is susceptible to nucleophilic attack.³⁸ Arg222 in TMADH is conserved with Arg230 in HADH and is important for the stability of negative charge buildup in the N1 atom and C2 carbonyl region. Mutation studies of Arg222 to lysine in TMADH show reduced flavination of the enzyme, while R222V and R222Q prevent flavinylation altogether.³⁸ Arg222 in TMADH is conserved as Arg230 in HADH, suggesting the possible formation of 6-S-Cys-FMN following the same mechanism. Similar mutation studies of HADH would conclusively support the iminoquinone methide tautomeric mechanism.

2.4.5.3. The Two Electron Potential of the 6-S-cys-FMN may be Influenced by the Butterfly Bend of 6-S-Cys-FMN in the Active Site

The 6-S-Cys-FMN of HADH has a unique bend along the N5-N10 axis of the flavin isoalloxazine ring in the active site. The butterfly bend of 6-S-Cys-FMN in TMADH was originally thought to be a result of the covalent

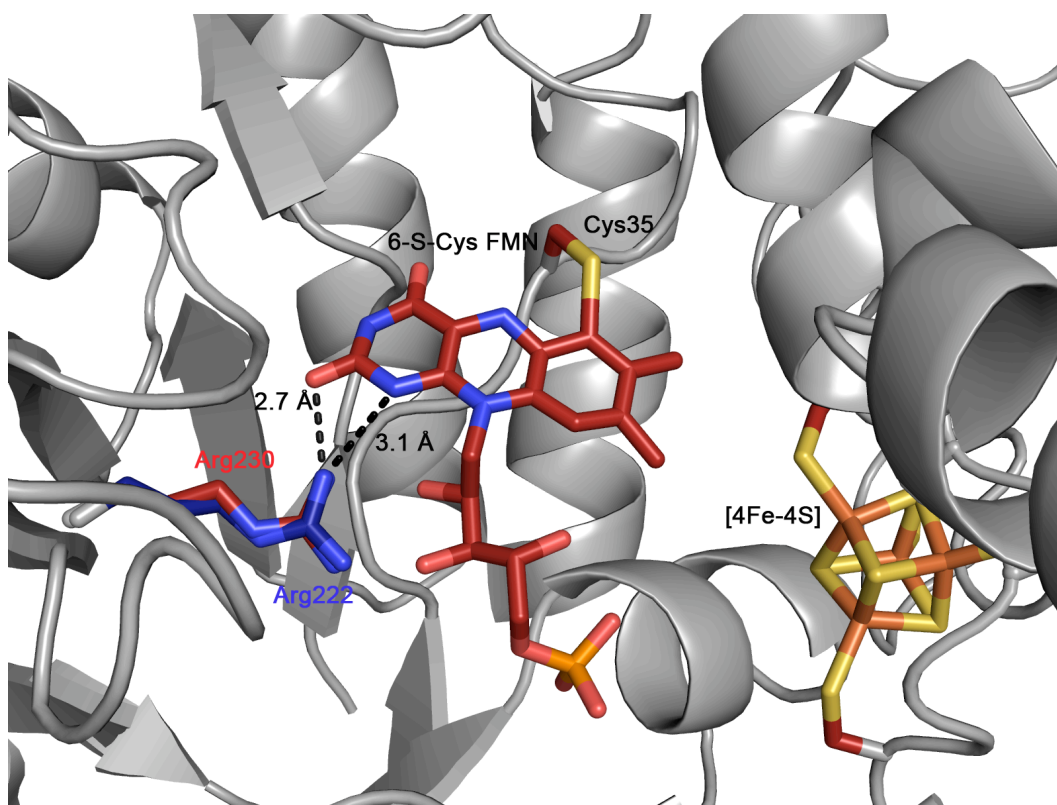


Figure 2.17. The spatial arrangement of Arginine in HADH (Red Arg230) and TMADH (Blue Arg222) suggests similar mechanism of 6-S-Cys-FMN biogenesis

linkage of the thioether bond of the cysteine and the isoalloxazine ring.⁴⁶

However, mutation studies of C30A in TMADH resulted in a non-covalently bound 6-S-Cys-FMN identical to native TMADH, suggesting this covalent linkage is not responsible for the 25° butterfly bend.⁴⁶ Computational studies on both the planar and butterfly bend conformations were performed on lumiflavin and C6-methylsulfanyllumiflavin, and these studies suggested that

the butterfly bend raises the two-electron reduction potential, making the 6-S-Cys-FMN more reactive to substrate.^{40,41} Based on the electron density of HADH, the bend of the 6-S-Cys-FMN is not as extensive as the bend in TMADH. The redox potential of HADH for 6-S-Cys-FMN_{O/S} and 6-S-Cys-FMN_{S/R} have been reported to be +34 mV and +30 mV, respectively,⁴² while the reported values of TMADH for 6-S-Cys-FMN_{O/S} and 6-S-Cys-FMN_{S/R} are +44 mV and +36 mV, respectively.⁴⁷ The slightly less positive redox potentials of 6-S-Cys-FMN in HADH may be influenced by the slightly flattened bend in the 6-S-Cys-FMN.

2.4.5.4 Conserved Tyr in the Active Site Contributes to the Spin-interaction States of HADH and TMADH

Tyr176 in HADH is conserved as Try169 in TMADH, but is almost 1.0 Å farther away from isoalloxazine ring (Figure 2.18). Mutation studies on TMADH with Y169F revealed the loss of the spin couple of the semiquinone and reduced [4Fe-4S].³⁶ This phenomenon was observed by EPR as the loss of feature at half-field. This same phenomenon of the loss of the feature at half-field is observed native HADH.³⁶ Limburg et al. suggested that either the spatial arrangement of the two cofactors or the arrangement of the amino acids could affect the spin coupling.² The 6-S-Cys-FMN distance to [4Fe-4S] are equal in HADH and TMADH with 4.0 Å from the 8 α carbon to the nearest cysteine residue and 5.7 Å from the 8 α -methyl to the closest iron in the [4Fe-

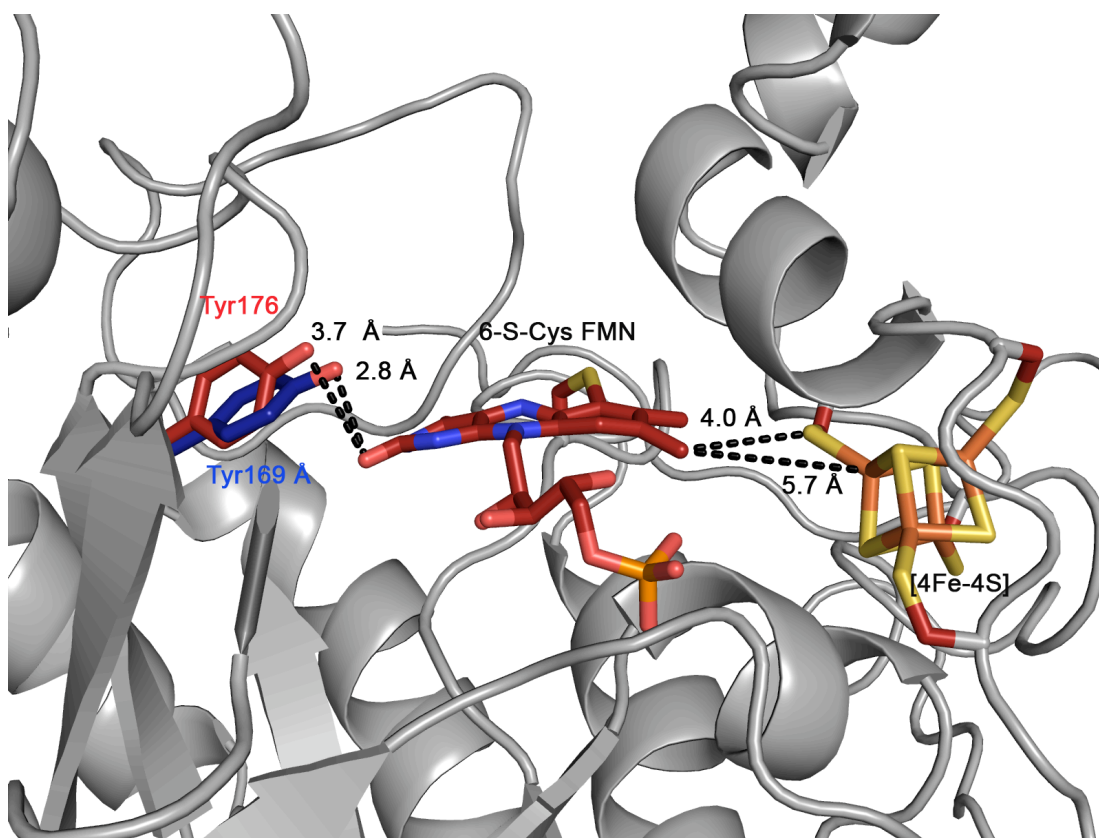


Figure 2.18. Conserved Tyr in the Active Site Contributes to the Spin-interaction States of HADH (Red Tyr176) and TMADH (Blue 169)

4S] shows the spatial relationship of the cofactors is the same. In a mutation study done by Scrutton substituting Tyr169 with phenylalanine, the complex EPR signal associated with the spin-interaction state in the wild type is not observed at high-field and the signal at $g \sim 4$ is greatly reduced.³⁶ The mutant forms the semiquinone and reduced [4Fe-4S], but the magnetic moments of the two unpaired spins do not interact as strongly as wild type. The proposed

rationale behind this was that the negative charge on the hydroxyl group develops and forces unpaired electron density on the 6-S-Cys-FMN towards [4Fe-4S] and reduces the distance of the spin-interaction. The tyrosine in the active site of HADH is almost an entire Å farther from the isoalloxazine ring and likely does not assist in the spin coupling of the semiquinone and reduced [4Fe-4S].

2.4.6. Histamine Binding In HADH

2.4.6.1. The Modeling of Histamine in the Active Site reveals Important Residues for Selectivity

Limburg et al. proposed that the mono-protonated histamine binds to the active based on the pH dependence on k_{cat}/K_m .² Results of modeling studies also suggest a more favorable binding of the mono-protonated over the neutral histamine. Also predicted were the active site residues Glu79 and Asp358 involved in histamine binding², and could contribute to the ionization observed in the pH dependence on k_{cat}/K_m . The involvement of these residues in histamine binding are also consistent with modeling studies. Histamine is also stabilized by Phe77 and Tyr181 through π - π stacking interactions.

The binding of histamine in the active site of HADH explains the high selectivity. Biogenic amines such as tyramine and dopamine, which have a hydroxyl group on the aromatic ring would have a high degree of steric hindrance with the asparagine residue (Asn115), which would not allow for

the binding of these substrates. Aliphatic amines, such as n-butylamine, putrescine, and methylamine, do not benefit from the π - π interactions that are observed with the imidazole group of histamine. Agmatine could take advantage of both the interactions with the amino group and the π - π interaction of the guanidine group, along with stabilization with the asparagine residue. However, the π - π interaction would not be comparable to the imidazole ring histamine, which alters its binding affinity.

2.4.6.2 Known Binding motif of Histamine Binding Proteins

Validates the Binding mode of Histamine in HADH.

There are a handful of proteins that have been crystallized with histamine bound in the active site.⁴⁸ These range from proteins found in humans, histamine methyltransferase and histidine decarboxylase, to proteins found in insects, nitrophorin and histamine binding proteins. Though the residues involved in the binding of histamine differ, the stabilization of histamine through either the imidazole ring or the amino group of histamine is conserved throughout these proteins. When comparing HADH with the other histamine binding proteins, the binding motif correlates most closely with salivary proteins seen in blood sucking insects, commonly known as histamine binding proteins (HBP), and histamine methyltransferase. In the HBPs, the negatively charged residues of aspartic acid, glutamic acid, or both stabilize the amino group of histamine. Stacking interactions with the aromatic residues tyrosine, phenylalanine, and tryptophan help to stabilize the

imidazole ring of histamine. The HBPs found in these insects function to bind histamine with high affinity during blood feeding, as this will suppress the inflammation response. The role of histamine methyltransferase (HNMT) is to inactivate histamine. This occurs by transferring a methyl group from S-adenosyl-L-methionine to the imidazole ring. The binding of histamine in HNMT involves the amino group of histamine interacting with glutamic acid, glutamine, and asparagine residues. The aromatic residues tryptophan and tyrosine provide π stacking with the imidazole. The binding of histamine in HADH follows the motif of these two classes of proteins. HADH binds the amino group of histamine through negatively charged aspartic acid and glutamic acid residues, along with π - π stacking interactions with tyrosine and phenylalanine. Even though the function and mechanism of HBPs, HNMT, and HADH differ, the selectivity of histamine and the binding motif is clearly consistent with these high-affinity histamine-binding proteins

2.4.6.3. Docking of Histamine in the Active Site of HADH has Similarities with Human Histamine Receptor/ Histamine Model

The sequences of the human histamine receptors (HHR) are known, but the crystal structures have yet to be determined.³⁻⁷ Modeling studies of the HHR and other histamine binding proteins have provided some understanding of the physiological binding of histamine. In all four HHR, a salt bridge between a conserved aspartic acid and the amino group of histamine has proven essential for histamine binding based on site-directed

mutagenesis studies.³⁻⁷ HADH also has an aspartic acid residue that forms a salt bridge with the cationic amino group of histamine, exhibiting a similar binding motif to all four HHRs, with a glutamic acid residue that also contributes to the ion-pair interaction. HHR 1 and HHR 4 both contain an asparagine residue that hydrogen bond to the imidazole nitrogen.^{3,49} In HADH, Asn115 plays the same role as the asparagine in these two HHR, stabilizing the imidazole ring. In HHR1, a tyrosine residue contributes to imidazole binding by forming a π - π interaction³, while in HADH Tyr181 and F77 provide the same stabilization of the imidazole group. The binding motif of HADH demonstrates significant similarities with HHR, and especially the binding motif of HHR1.

One of the most prescribed families of pharmacological drugs are designed to target the H1 receptor within the body. Understanding how histamine binds within this receptor could greatly increase selectivity and specific pharmacological action. The important residues in the HHR 1 that are essential for the binding of histamine are aspartic acid, tyrosine, and asparagine. In HADH, the same residues interact to stabilize histamine making HADH a great model for HHR1, for which the crystal structure has not been solved.

2.4.7. The Possible Catalyst Mechanism for C-H Bond Cleavage and Potential to Probe the Possible Mechanism.

The proposed mechanism of C-H bond cleavage for HADH involves the nucleophilic attack amino group of histamine at the C4 position of the 6-S-Cys-FMN with proton abstraction by the N5 atom of the 6-S-Cys-FMN. Elimination and formation of the imine follows the nucleophilic attack and then subsequent oxidation with water and the eventual formation of the reduced 6-S-Cys-FMN. (Figure 2.19) This mechanism had been proposed by TMADH and MAO.^{10,50,51} Limburg et al. determined the KIE of 7.0 indicating the C-H bond cleavage was part of the rate determining step under subsaturating conditions.² They also observed the reaction of phenylhydrazine with HADH. In TMADH, Scrutton et al. reacted phenylhydrazine and noticed that an unusual spectrum was observed.⁵² After isolation of the isoalloxazine ring, the phenylhydrazine was seen complexed to the ring. This electrophilic position was also confirmed by experimental and computational studies on the isoalloxazine.^{46,53} Quantitative structure-activity relationships (QSAR) with MAO have been performed by Edmondson with para and meta-substituted benzylamines.¹⁰ They observed negative charge build up that supports proton abstraction mechanism for the substrate C-H bond and suggests a polar nucleophilic mechanism as proposed here. Further computational studies of the LUMO in both lumiflavin and C6-methylsulfanyllumiflavin suggest significant orbital density on N5 and C4a.⁴⁶ This could play a significant role in the mechanism of C-H bond cleavage of

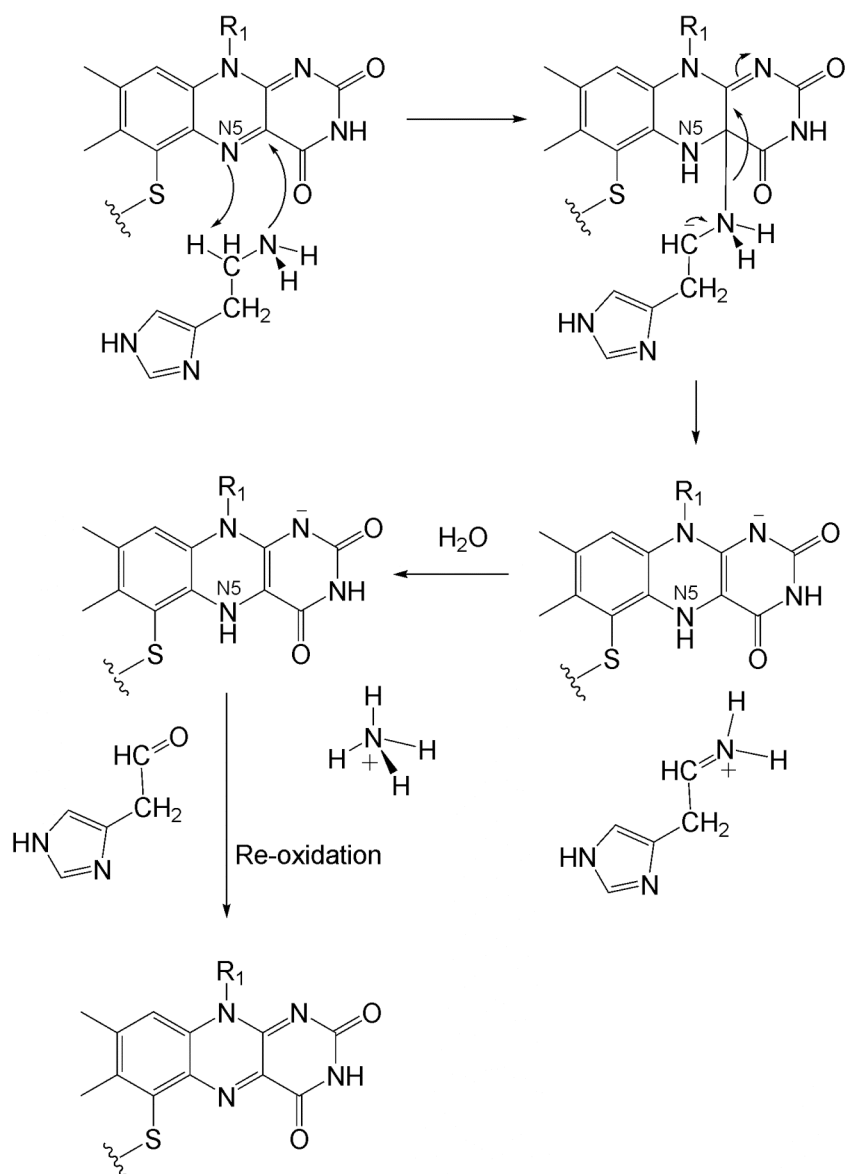


Figure 2.19. Proposed Oxidation of Histamine by HADH

histamine. The positive electrostatic potential found at C4a suggests a possible location of substrate adduct formation.⁴⁶

Phenylhydrazine is known to react with 6-S-Cys-FMN in HADH and TMADH.^{2,52} The KIE found in HADH that shows the C-H bond cleavage is rate limiting.² These mechanistic similarities suggest that HADH undergoes nucleophilic addition mechanism in the substrate oxidation.^{10,50,51}

Other possible means of probing the mechanism of HADH could involve the use of derivatized substrates.² The use of mono or di-substituted fluorohistamine creates an amino group that is harder to oxidize and decreases the nucleophilicity of histamine. A decrease in the rate of the reduction would suggest a covalent mechanism is involved in substrate oxidation. Substrates with steric bulk at the amine position would affect the rate of reduction if a covalent mechanism is employed. If the reduction rate is constant with these derivatives there is a possibility of electron transfer, and an increase in reaction rate with the difluorohistamine might suggest a hydride transfer.² This could possibly help in towards understanding oxidation of substrate in flavoproteins.

2.4.8. The Possible Electron Transfer from Cofactors of HADH to the External Electron Exceptor.

In the oxidative half-reaction, HADH transfers one electron from the reduced [4Fe-4S] cluster to an external electron acceptor. The natural electron acceptor for HADH is unknown. The physiological electron acceptor

for TMADH was found to be the electron transferring flavoprotein (ETF).⁵⁴ In TMADH, Tyr442 was shown to be the means of transferring electrons to ETF.⁵⁵ Mutation studies of Tyr442 and Val344 in TMADH demonstrate two possible pathways for electron transfer.⁵⁵ With ferricenium (Fc) as the electron acceptor, the rate of electron transfer was greatly affected by introduction of various mutations at Val344. Smaller side chains (Val344A, Val344C, and Val344G) showed an increased rate, while longer side chains (Val344I and Val344Y) reduced the rate of electron transfer to Fc⁺. Electron transfer to native ETF was unaffected by mutations at Val344. In contrast, mutations at Tyr442 had little effect on electron transfer to Fc⁺, while the mutations Tyr442P, Tyr442L, Tyr442C, and Tyr442G showed major reduction of electron transfer to ETF. The conclusion of this mutation study suggested two modes of electron transfer: 1) electron transfer from the [4Fe-4S] to Val344 is the shortest pathway, because small Fc⁺ is able to access through a small groove. 2) ETF is not able to penetrate this small groove, and electron transfer occurs on a longer pathway from Cys345 to Glu439 to Tyr442. The physiological electron acceptor for HADH is not known, and ETF protein could not be recovered in the purification process of HADH from *N. simplex*. Some possible single-electron acceptors are ferredoxin, cytochrome c, and azurin.² The residues of the electron transfer pathway found in TMADH are not conserved within HADH (Figure 2.20). The longer pathway in HADH includes Cys348 to Ala441 to Arg444, though electron transfer along this route is

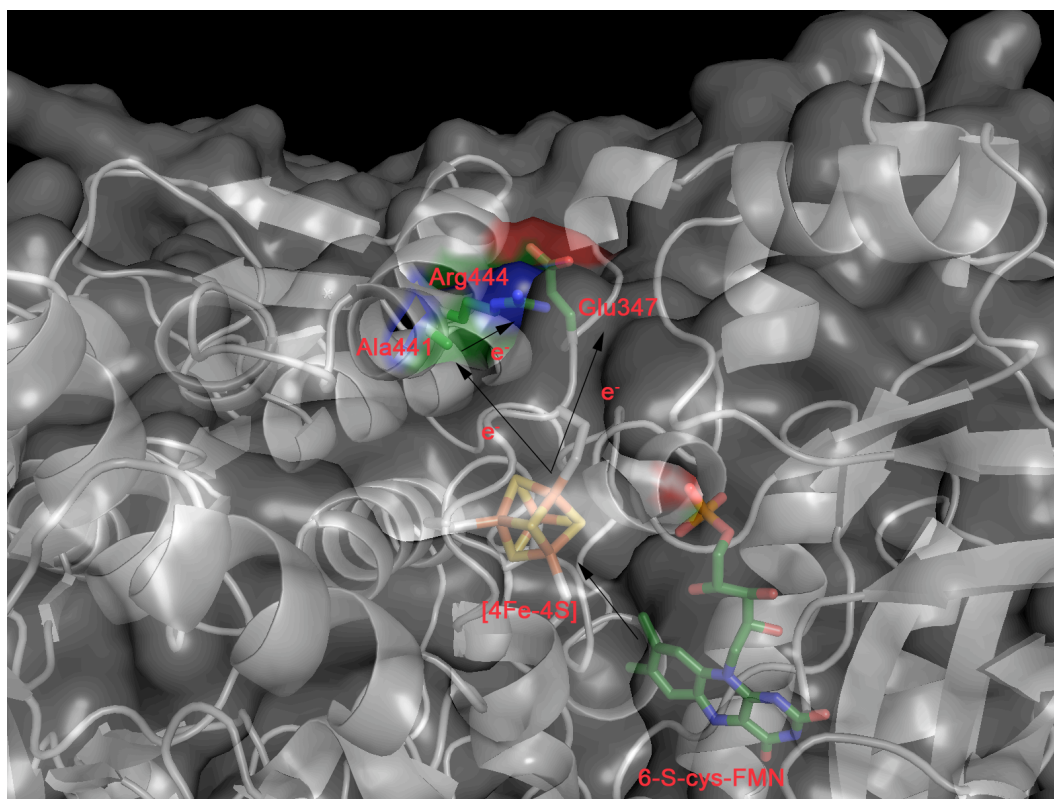


Figure 2.20. Proposed Electron transfer of HADH

probably unlikely. The more probable route of electron transfer is from Cys348 to Glu347. Glu347 is exposed to the surface and is directly adjacent to Cys348. Mutations of this cysteine residues in HADH are currently in progress to uncover the mechanism and residues involved in the oxidative half-reaction. Further studies will decipher the specific route of electron transfer in HADH.

2.4.9. Possible Design of a Histamine Sensor

In the design of an enzymatic sensor, the transfer of electrons from the reduced enzyme to the electrode surface is vital for successful detection. Charge transfer can occur through a mediator or by engineering the enzyme to the electrode surface. Biosensor design has been pursued by several groups. One means of creating an enzymatic biosensor is to immobilize the enzyme in a polypyrrole film on the electrode surface. Potassium ferricyanide was employed to mediate electrons from the reduced enzyme to the electrode. HADH has demonstrated substrate inhibition based on the substrate and external electron acceptor concentrations, so problems with the sensitivity at high histamine concentration might arise if the external electron acceptor is not present at sufficient concentrations to reoxidize HADH. A better route to an enzymatic biosensor would be to genetically engineer the protein to the sensor itself. This would allow for electrons to travel directly from the [4Fe-4S] to the electrode. This concept was demonstrated with TMADH, where the enzyme was wired to the electrode.¹⁴ In order for electron transfer to occur, the wiring of the enzyme needs to be in close proximity to the redox active cofactors. HADH has an ideal setup, with the residue right next to the [4Fe-4S] exposed to the surface of the enzyme (Glu347). This residue can be mutated to a cysteine residue, which can in turn be immobilized onto the surface of the electrode. However, mutation close to the [4Fe-4S] might cause a change in the reduction potential. Cyclic voltammetry would need to be employed to test the redox potential of the

[4Fe-4S] to ensure no change had occurred. A design for a portable enzymatic sensor for histamine detection could be applicable in the field of cancer research and in FDA detection of contaminated fish.

2.5. Conclusion

HADH is known to have high substrate selectivity. To better understand this narrow substrate selectivity, structural studies were performed on histamine dehydrogenase.² HADH crystallization conditions were screened finding HRI #39 as optimal for crystal growth. Further screening would be useful to obtain data with higher resolution or with histamine bound. Overall, a complete data set was collected with HADH crystals that contained 4% glycerol and a “walking stick” crystal morphology. Although they grew readily, the diffraction of the square boxes yielded poor diffraction quality. Shifting the equilibrium of crystal growth towards the “walking sticks” could improve the resolution, especially when co-crystallization of substrate is desired. Slight modifications in HRI #39, such as pH, salt, or buffer concentration, should be explored. Also, slight modification to EBI #20 and EBI#33 could produce desirable crystals. X-ray diffraction data of HADH recombinantly expressed in *E. coli* has been determined to 2.7 Å resolution. HADH shares the common TIM barrel motif found in many flavoproteins along with prosthetic groups that are spatially analogous to other FMN and [4Fe-4S] dependent flavoproteins. The docking studies suggest that binding of histamine mimics the binding motif found in

histamine methyltransferase and HBP. These enzymes are selective for histamine and bind histamine with high affinity. In these proteins, the amino group is stabilized by the negative charge on the carboxylate group and π - π interaction with aromatic residues. Histamine is proposed to have a similar binding motif with human histamine receptors (HHR), especially human histamine receptor 1, which is the target of pharmaceutical drug design. A conserved aspartic acid found in all four HHR, stabilizes the amino group of histamine through ion-pair interactions. HHR 1 also stabilizes the imidazole ring of histamine with tyrosine and asparagine residues. Both the ion pair interaction and the imidazole stabilization binding motifs are conserved in HADH. HADH's high selectivity towards histamine and its optimal electronic properties make it an excellent choice for a biosensor for the detection of histamine. The similar binding motif of HADH and HHR 1 could provide a better understanding of histamine binding within the body, allowing the development of highly specific and selectivity antagonists to HHR1.

Reference

- (1) Siddiqui, J. A.; Shoeb, S. M.; Takayama, S.; Shimizu, E.; Yorifuji, T. *FEMS Microbiology Letters* **2000**, *189*, 183-187.
- (2) Limburg, J.; Mure, M.; Klinman, J. P. *Archives of Biochemistry and Biophysics* **2005**, *436*, 8-22.
- (3) Jongejan, A.; Leurs, R. *Archiv. der Pharmazie*. **2005**, *338*, 248-259.
- (4) Gantz, I.; Munzert, G.; Tashiro, T.; Schaffer, M.; Wang, L.; DelValle, J.; Yamada, T. *Biochemical and Biophysical Research Communications* **1991**, *178*, 1386-92.
- (5) Stark, H.; Sippl, W.; Ligneau, X.; Arrang, J. M.; Ganellin, C. R.; Schwartz, J. C.; Schunack, W. *Bioorg. Med. Chem. Lett.* **2001**, *11*, 951-4.
- (6) Sippl, W.; Stark, H.; Holtje, H. D. *Pharmazie* **1998**, *53*, 433-7.
- (7) Oda, T.; Morikawa, N.; Saito, Y.; Masuho, Y.; Matsumoto, S.-I. *Journal of Biological Chemistry* **2000**, *275*, 36781-36786.
- (8) Scrutton, N. S. *Natural Product Reports* **2004**, *21*, 722-730.
- (9) Kay, C. W. M.; El Mkami, H.; Molla, G.; Pollegioni, L.; Ramsay, R. R. *Journal of the American Chemical Society* **2007**, *129*, 16091-16097.
- (10) Miller, J. R.; Edmondson, D. E. *Biochemistry* **1999**, *38*, 13670-13683.
- (11) Rigby, S. E. J.; Hynson, R. M. G.; Ramsay, R. R.; Munro, A. W.; Scrutton, N. S. *Journal of Biological Chemistry* **2005**, *280*, 4627-4631.
- (12) Lui, G.; Paddon-Row, M.; Gooding, J. *Electrochem. Commun.* **2007**, *9*, 2218-2223.
- (13) Loechel, C.; Basran, A.; Basran, J.; Scrutton, N. S.; Hall, E. A. H. *Analyst* **2003**, *128*, 166-172.
- (14) Loechel, C.; Basran, A.; Basran, J.; Scrutton, N. S.; Hall, E. A. H. *Analyst* **2003**, *128*, 889-898.
- (15) Trickey, P.; Basran, J.; Lian, L. Y.; Chen, Z. W.; Barton, J. D.; Sutcliffe, M. J.; Scrutton, N. S.; Mathews, F. S. *Biochemistry* **2000**, *39*, 7678-7688.
- (16) Cohen, A. E., Ellis, P. J., Miller, M. D., Deacon, A. M. & Phizackerley, R. P. *J. Appl. Cryst.* **2002**, *35*, 720-726.
- (17) Leslie, A. G. W. *Acta Crystallographica Section D-Biological Crystallography* **2006**, *62*, 48-57.
- (18) Collaborative Computational Project, N. *Acta Cryst.* **1994**, *D50*, 760-763.
- (19) Reed, T. M.; Hirakawa, H.; Mure, M.; Scott, E. E.; Limburg, J. *Acta Crystallogr. F* **2008**, *F64*, 785-787.
- (20) Murshudov, G. N.; Vagin, A. A.; Dodson, E. J. *Acta Crystallogr. Sect. D Biol. Crystallogr.* **1997**, *D53*, 240-255.

- (21) Emsley, P.; Cowtan, K. *Acta Crystallogr. Sect. D: Biol. Crystallogr.* **2004**, *D60*, 2126-2132.
- (22) Laskowski, R. A.; MacArthur, M. W.; Moss, D. S.; Thornton, J. M. *Journal of Applied Crystallography* **1993**, *26*, 283-91.
- (23) Vriend, G. *Journal of Molecular Graphics* **1990**, *8*, 52-6, 29.
- (24) DeLano, W. L. T. P. M. G. S. D. S., San Carlos, CA, USA.
- (25) SYBYL 8.0, T. T. A., St. Louis, MO, 2007. .
- (26) Clark, M.; Cramer, R. D., III; Van Opdenbosch, N. *Journal of Computational Chemistry* **1989**, *10*, 982-1012.
- (27) Gasteiger, J.; Marsili, M. *Tetrahedron* **1980**, *36*, 3219-22.
- (28) Rarey, M.; Kramer, B.; Lengauer, T.; Klebe, G. *Journal of Molecular Biology* **1996**, *261*, 470-489.
- (29) Lovell, S., Davis, I., Arendall III, W.B., de Bakker, P., Word, J., Prisant, M., Richardson, J., Richardson, D., *Proteins: Structure, Function, and Genetics* **2003**, *50*, 437-450.
- (30) Hubbard Paul, A.; Liang, X.; Schulz, H.; Kim Jung-Ja, P. *J. Biol. Chem.* **2003**, *278*, 37553-60.
- (31) Mewies, M.; McIntire, W. S.; Scrutton, N. S. *Protein Science* **1998**, *7*, 7-20.
- (32) Yang, C.-C.; Packman, L. C.; Scrutton, N. S. *European Journal of Biochemistry* **1995**, *232*, 264-71.
- (33) Lindqvist, Y.; Braenden, C. I.; Mathews, F. S.; Lederer, F. *Journal of Biological Chemistry* **1991**, *266*, 3198-207.
- (34) Lim, L. W.; Shamala, N.; Mathews, F. S.; Steenkamp, D. J.; Hamlin, R.; Nguyen Huu, X. *Journal of Biological Chemistry* **1986**, *261*, 15140-6.
- (35) Colby, J.; Zatman, L. J. *Biochem. J.* **1974**, *143*, 555-67.
- (36) Basran, J.; Jang, M. H.; Sutcliffe, M. J.; Hille, R.; Scrutton, N. S. *J. Biol. Chem.* **1999**, *274*, 13155-61.
- (37) Basran, J.; Sutcliffe, M. J.; Hille, R.; Scrutton, N. S. *Biochemical Journal* **1999**, *341*, 307-314.
- (38) Mewies, M.; Basran, J.; Packman, L. C.; Hille, R.; Scrutton, N. S. *Biochemistry* **1997**, *36*, 7162-7168.
- (39) Hasford, J. J.; Kemnitzer, W.; Rizzo, C. J. *Journal of Organic Chemistry* **1997**, *62*, 5244-5245.
- (40) Zheng, Y.-J.; Ornstein, R. L. *Journal of the American Chemical Society* **1996**, *118*, 9402-9408.
- (41) Dixon, D. A.; Lindner, D. L.; Branchaud, B.; Lipscomb, W. N. *Biochemistry* **1979**, *18*, 5770-5.
- (42) Tsutsumi, M.; Fujieda, N.; Tsujimura, S.; Shirai, O.; Kano, K. *Bioscience, Biotechnology, and Biochemistry* **2008**, *72*, 786-796.
- (43) Bellamy, H. D.; Lim, L. W.; Mathews, F. S.; Dunham, W. R. *Journal of Biological Chemistry* **1989**, *264*, 11887-92.

- (44) Rhodes, G. *Crystallography Made Crystal Clear*, Third ed.; Elsevier: New York, 2006.
- (45) Basran, J.; Mewies, M.; Mathews, F. S.; Scrutton, N. S. *Biochemistry* **1997**, 36, 1989-1998.
- (46) Trickey, P.; Basran, J.; Lian, L. Y.; Chen, Z.; Barton, J. D.; Sutcliffe, M. J.; Scrutton, N. S.; Mathews, F. S. *Biochemistry* **2000**, 39, 7678-88.
- (47) Pace, C. P.; Stankovich, M. T. *Arch. Biochem. Biophys.* **1991**, 287, 97-104.
- (48) Konkimalla, V. B.; Chandra, N. *Biochemical and Biophysical Research Communications* **2003**, 309, 425-431.
- (49) Shin, N.; Coates, E.; Murgolo, N. J.; Morse, K. L.; Bayne, M.; Strader, C. D.; Monsma, F. J., Jr. *Molecular Pharmacology* **2002**, 62, 38-47.
- (50) Basran, J.; Sutcliffe, M. J.; Scrutton, N. S. *Journal of Biological Chemistry* **2001**, 276, 42887-42892.
- (51) Basran, J.; Sutcliffe, M. J.; Scrutton, N. S. *Journal of Biological Chemistry* **2001**, 276, 24581-24587.
- (52) Nagy, J.; Kenney, W. C.; Singer, T. P. *J. Biol. Chem.* **1979**, 254, 2684-8.
- (53) Kim, J. M.; Bogdan, M. A.; Mariano, P. S. *Journal of the American Chemical Society* **1993**, 115, 10591-5.
- (54) Huang, L.; Rohlf, R. J.; Hille, R. *Journal of Biological Chemistry* **1995**, 270, 23958-65.
- (55) Basran, J.; Chohan, K. K.; Sutcliffe, M. J.; Scrutton, N. S. *Biochemistry* **2000**, 39, 9188-9200.

Chapter 3

Targeting the Endoplasmic Reticulum for Inhibition of Collagen

Production by Prolyl 4-Hydroxylase

3.1. Background

3.1.1. Fibrosis

Fibrosis is a disease characterized by the over production and progressive accumulation of collagen.¹ Fibrosis has been observed in many tissues and organs including the heart, kidney, lungs, blood vessels, and skin.^{1,2} Excessive collagen production results in the destruction of normal function and structure of these organs. The most prevalent types of fibrosis include pulmonary fibrosis, fibrosis of the liver, and rheumatoid arthritis. Table 3.1 demonstrates the effects of fibrosis on people. In pulmonary fibrosis, the air sacs in the lungs thicken from

	Deleterious Effects
Pulmonary Fibrosis	84,000 people die each year ³
Liver Fibrosis	900,000 people have been diagnosed 26,000 people will die ⁴
Rheumatoid Arthritis	Millions of people affected with joint pain and discomfort ⁵

Table 3.1. The deleterious effects of fibrosis on human population

the formation of scar tissue,⁶ making oxygen transfer from the lungs to the blood very difficult. Fibrosis of the liver, or cirrhosis, involves the development of scar tissue in place of normal tissue. This scar tissue blocks the transfer of blood into the liver preventing the removal of poisons and bacteria from the blood.⁷ Rheumatoid arthritis is an autoimmune disease that causes inflammation of the joints and the surrounding connective tissue.⁵ The destruction of cartilage and ligaments triggers the inflammatory response, which produces scar tissue.

While all types of fibrosis within these tissues are characterized by excess collagen, the environmental triggers that cause fibrosis within these tissues vary significantly. Pulmonary fibrosis is primary caused by smoking, inhalation of inorganic dusts or chemicals, or viral infections.³ Liver fibrosis is often caused by excessive alcohol consumption or viral hepatitis.⁸ In many cases of fibrosis, the initial cause of inflammation is varied, but the deleterious effect is the overproduction of collagen. Fibrotic diseases are chronic and progressive in their injurious effect. A treatment able to cure or minimize fibrosis could alleviate the pain and discomfort felt by many around the world.

3.1.2. Fibrosis – Pathway and Possible Prevention

Development of a cure to fibrosis is as varied as the disease itself. Simply abstaining from alcohol or smoking will greatly reduce the risk of liver fibrosis and slow its advancement within the body.⁸ The cellular response is another target towards inhibiting fibrosis. The cellular involvement in the

pathway to fibrosis is described in Figure 3-1.^{9,10} After tissue is damaged, the body responds to substances released from dead and dying cells by the activation of macrophages. These macrophages activate cytokines, the most notable being TNF- α and interleukins 1 and 6. The pathway continues with the activation of the inflammatory response in the local environment,

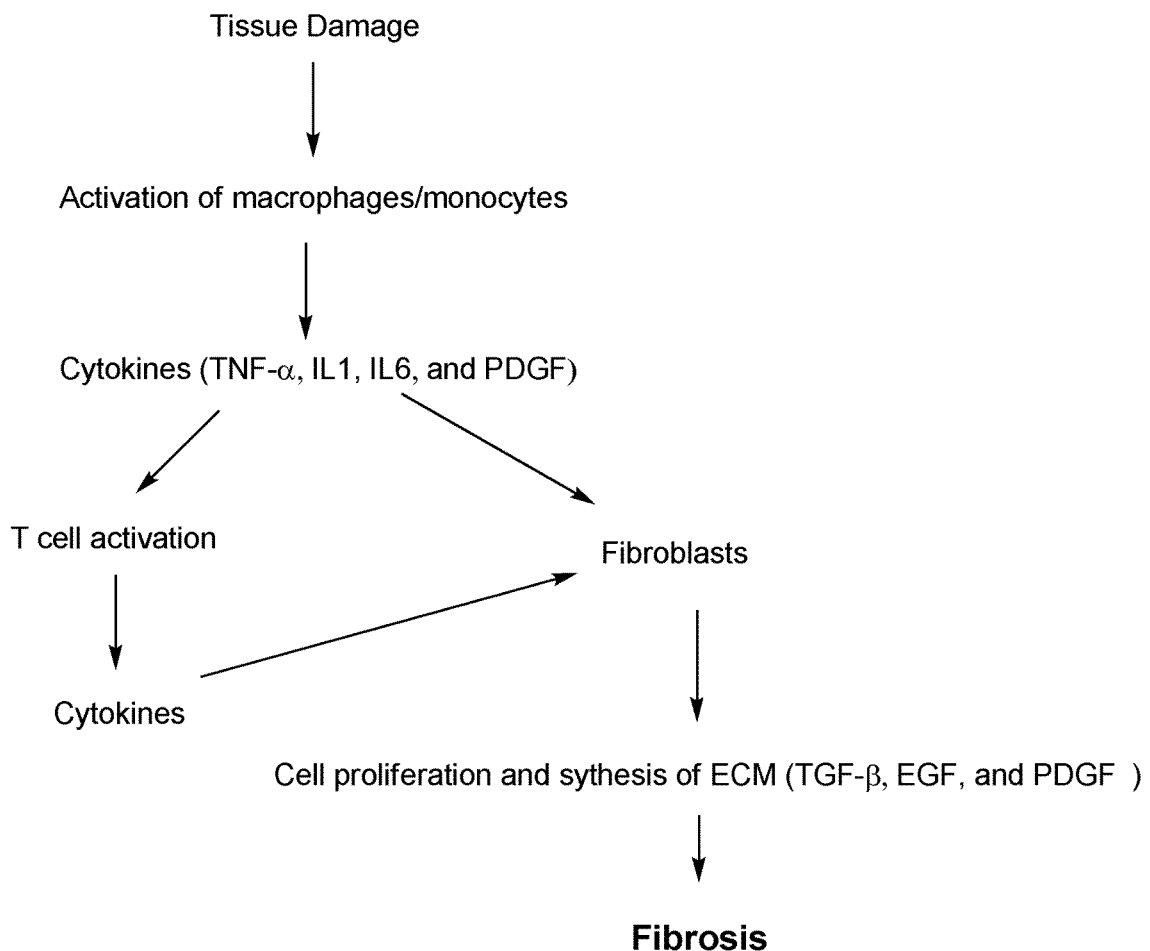


Figure 3.1. Damage to the tissue elicits a cascade immune response. The persistent cell damage causes the sequence of events that lead to the developing of fibrosis.¹¹

especially with EGF, PDGF and TGF- β .¹⁰ Eventually, the cytokines activate fibroblast cells and elicit the production of collagen. Persistent tissue damage leads to continued inflammatory response, which eventually causes the overproduction of collagen and therefore fibrosis.

Many of the fibrosis drugs being developed target the immune response with the hope of preventing the production of scar tissue. Anti-inflammatory therapy and steroids have been successful in preventing the inflammation response, causing a reduction of fibrosis.^{8,12} Steroids have had a more prolonged effect on chronic fibrosis than non-steroidal anti-inflammatory drugs.¹² The increased expression of mRNA and protein levels of TGF- β seen in rats with liver fibrosis and pulmonary fibrosis has led to an increased interest in targeting the TGF- β pathway.¹³ When TGF- β is directly injected into test subjects, fibrogenic tissues are observed.¹⁴ Experiments using antibodies to TGF- β have reduced scarring in rats without disrupting the body's wound healing response.¹⁵ However, using antibodies as a long term therapeutic agent could prove difficult due to the need to minimize their ability to stimulate an immune response.¹¹ Low molecular weight inhibitors that either block the interaction of TGF- β with its receptor or inhibit signal transduction mechanism for TGF- β could provide a safe and cost effective route to reduce fibrosis; however, the class of receptor that determines fibrogenic activity (Type I, II, or III) and which isoform of TGF- β (TGF- β 1 or TGF- β 2) is responsible for fibrogenic activity remains unclear.¹⁶ The cytokine

PDGF is also believed to be involved in fibrosis due to its location near tissue damaged sites.⁸ Inhibitors known as tyrosine kinase inhibitors inhibit PDGF-receptor tyrosine kinases.¹⁷ These drugs have been shown to be potential therapeutic agents against fibrosis and are progressing toward *in vitro* studies. All of these possible therapeutic drugs target different proteins on the pathway towards fibrosis.

3.1.3. Post-Translational Modification of Collagen by Prolyl 4-Hydroxylase: A Possible Target for Fibrosis

Many different types of collagen exist in the extracellular matrix, with types I and III being the most common, but these proteins all undergo the same post-translational modifications. The enzyme responsible for one of the key post-translational modifications is prolyl 4-hydroxylase (P4H).¹⁸ This enzyme is located in the lumen of the endoplasmic reticulum (ER) and is responsible for hydroxylation of peptidyl proline, which is crucial for the folding and stability of the collagen triple helix. Each monomer of collagen consists of a Gly-Xaa-Yaa repeat, where the Xaa residue is often proline and the Yaa residue is often trans 4-hydroxyproline (Hyp). Hyp is formed from the post-translational modification of proline by P4H and is essential for the stability of the collagen triple helix. Under-hydroxylated collagen that occurs due to inactive P4H, is not stable at room temperature and remains in the ER until either 1) activity of P4H is restored and collagen undergoes hydroxylation or 2) it is broken down within the lysosomal compartments.^{18,19} The prevention

of Hyp formation by P4H would inhibit the production of collagen, making P4H an attractive target for reducing fibrosis within the body.

3.1.4. Prolyl 4-Hydroxylase

P4H is a member of the α -ketoglutarate dependent non-heme iron oxygenases super family.¹⁹ The type I isoform of P4H found in mammals is an $\alpha_2\beta_2$ tetramer where each α subunit contains a catalytic active site responsible for the formation of Hyp as well as a peptide binding domain where collagen binds. The β subunit is protein disulfide isomerase (PDI) and is primarily responsible for enzyme solubility and the retention of the enzyme in the ER through the peptide recognition sequence of KDEL at the C terminus. The structure of human Type I P4H has yet to be solved but site-directed mutagenesis has identified important residues in the catalytic cycle (Figure 3-2).²⁰ His412, Asp414, and His483 comprise the iron binding site. These residues form a facial triad of ligands to the iron along with an 8-stranded β -helix core fold in the α subunit.^{18,19,21} The peptide-substrate binding domain is found between Gly138 through Ser244 and is unique to human type I P4H.²² The hydroxylation of peptidyl proline by P4H requires Fe^{II} , α ketoglutarate, O_2 , and ascorbate for catalysis.^{22,23} The iron in the resting state is Fe^{II} that is in six-coordinate octahedral coordination sphere with three water molecules and the His-Asp-His facial triad as ligands. Two water molecules are displaced upon the bidentate binding of α -ketoglutarate. Lys493 and His501 bind to the C-5 and C-1 carbonyl groups of α -

ketoglutarate to stabilize the cofactor. As substrate and O₂ enter the active site; O₂ binds to iron in the axial position and oxidizes Fe^{II} to Fe^{III}. Nucleophilic attack of the α-ketoglutarate by O₂ forms the Fe^{III}-peroxo bridge.

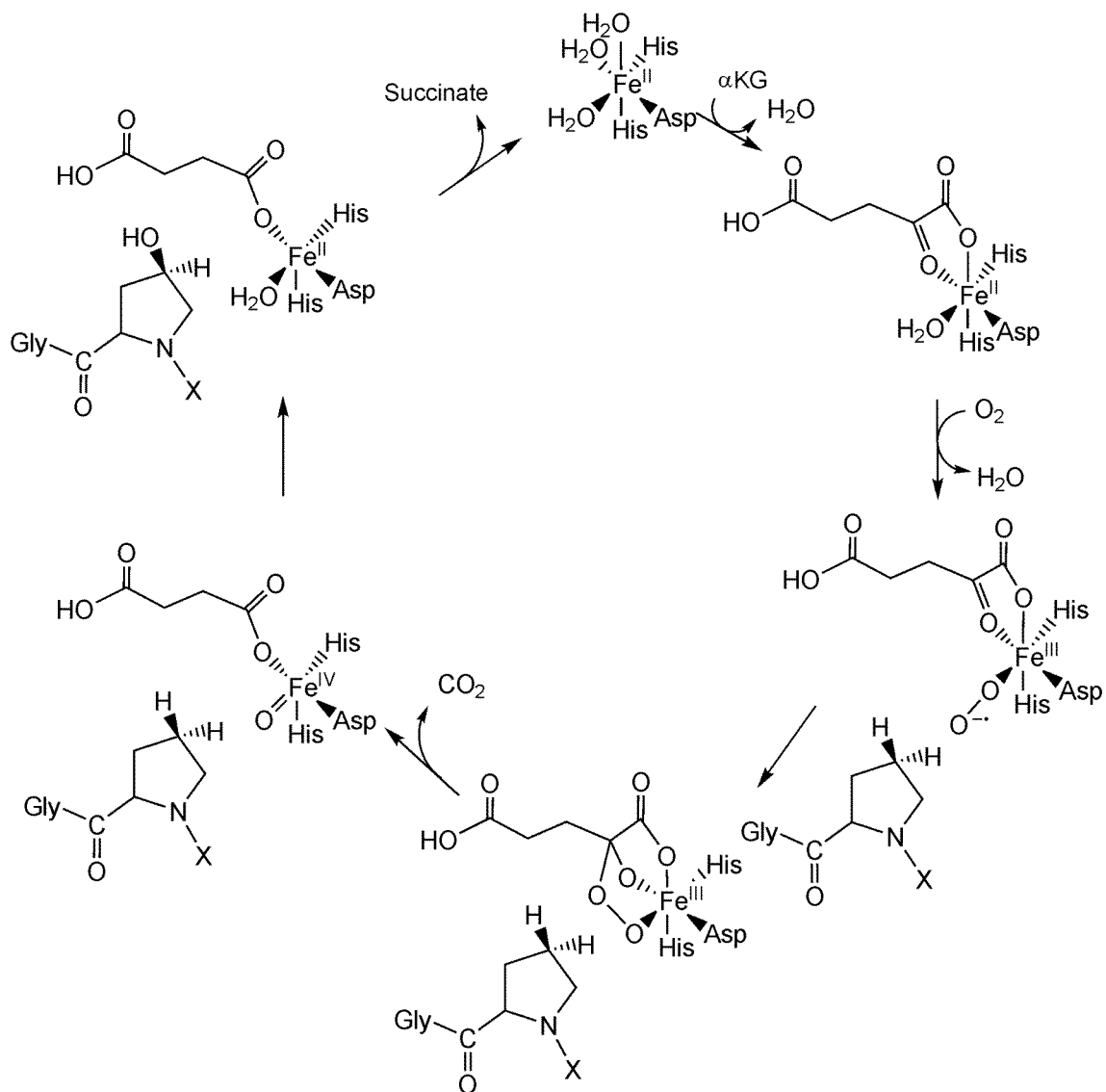


Figure 3.2. Proposed catalytic cycle of human type I prolyl 4-hydroxylase²⁰

α -ketoglutarate then undergoes oxidative decarboxylation to form succinate and reactive Fe^{IV}-oxo species. This reactive oxygen species catalyzes H-atom abstraction from the 4 position on proline, which is followed by a rebound step to form trans 4-hydroxyproline. Loss of succinate returns iron to its Fe^{II} resting state. During this process, succinate can accumulate and inactivate the enzyme unless ascorbate is present to restore the enzyme to its resting Fe^{II} state.

3.1.5. Current Iron Chelating P4H Inhibitors.

3.1.5.1. N-oxalylglycine Derivatives

Several inhibitors for P4H have been designed to mimic the binding of α -ketoglutarate to Fe^{II}. This binding prevents the decarboxylation step essential for catalytic turnover. Potential inhibitors of P4H have analogous structures to 2-oxoglutarate and mimic the bidentate binding to the Fe^{II} resting state. Franklin and coworkers designed chelators analogous to 2-oxoglutarate and tested them against both isolated avian P4H enzyme and collagen production in isolated chick-tendon cells (Table 3-2).²³ These inhibitors are proposed to bind to iron thereby preventing the oxidative decarboxylation to inhibit P4H. When tested against isolated avian P4H, N-oxalylglycine (**1**) demonstrated an IC₅₀ value of 3 μ M. A series of N-oxalylglycine derivatives were prepared and screened. Simple substitutions at the α -carbon atom of N-oxalylglycine (**2**) only raised the IC₅₀ and reduced activity of the derivatized N-oxalylglycine compounds. When the oxalyl C-

group was replaced with a heterocyclic cinnoline moiety (**3**), a 100-fold decrease in the IC₅₀ value was observed. It was proposed that the nitrogen from the heterocyclic and the nitrogen from the amide group would coordinate to the Fe^{II} complex. Methylation at the α-carbon (**4**) retained the same stereochemical restriction observed in the methylated N-oxalylglycine (**2**).

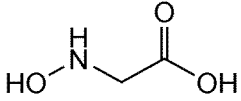
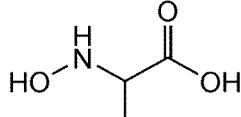
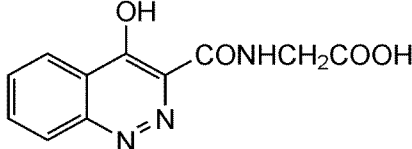
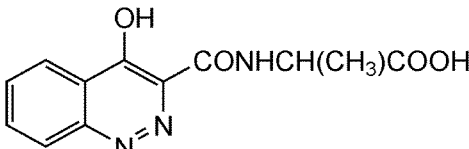
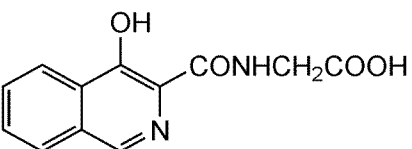
Compound	IC ₅₀ (μM)	
	Prolyl 4-Hydroxylase	Prolyl 4-Hydroxylase in isolated chick-tendon cells
(1) 	3.0	>150
(2) 	(S) 48 (R) 621	NA
(3) 	0.02	>81
(4) 	(S) 0.16 (R) 3.0	>81
(5) 	0.19	20

Table 3.2. IC₅₀ values for the inhibition of P4H by N-oxalylglycine and its derivatives against isolated P4H enzyme and in vitro with chick-tendon cells²³

One of the difficulties in drug design is delivery of the drug across the cytoplasmic membrane. N-oxalylglycine (**1**) has a 50-fold increased IC_{50} value when tested against P4H produced in chick tendon cells to compared to the isolated P4H. Similarly, the IC_{50} of the cinnoline derivative (**3**) increased from 0.02 μ M for isolated P4H to 81 μ M for the P4H produced in chick-tendon cells, which was the highest concentration tested. These data demonstrate the difficulty in drug design; an inhibitor maybe effective against isolated P4H but may prove ineffective in cellular and *in vivo* studies. In order to derive a more lipophilic inhibitor, the compound (**5**) was prepared and it resulted in a 4-fold decrease in IC_{50} value when tested against the P4H produced in chick-tendon cells. This demonstrates the importance of inhibitors with the ability to cross the intracellular membrane.

3.1.5.2. Pyridine-2,5 Dicarboxylic Acid Derivatives

Another common inhibitor of P4H is pyridine-2,5 dicarboxylic acid (**6**), which has an IC_{50} value of 5.5 μ M against isolated enzyme (Table 3-3A).²⁴ The nitrogen from the pyridine ring and the C-2 carboxylic acid group are believed to chelate iron thereby preventing the oxidative decarboxylation. Increased binding of this inhibitor to human P4H is seen because the C-5 carboxyl group can also bind to the distal carboxylate binding site, which is comprised of residues Lys493 and His501. Modifications of pyridine-2,5 dicarboxylic acid were made in order to improve P4H inhibition against isolated enzyme and investigate binding of the inhibitors (Table 3.3).²⁴ Two main modifications

were made: one involved variation of the chain lengths at the C-5 carboxylate position (Table 3.3A), while the second involved replacing the C-2 and C-5 carboxylic acid groups with acid mimics (Table 3.3B). Variations at the C-5 carboxyl position extended the length from a simple methyl group (**7**) to ethyl/ethylene (**8,9**) and to a benzyl group (**10**). Small variations in the IC₅₀ value were observed even with the large benzyl group (5-fold increase),

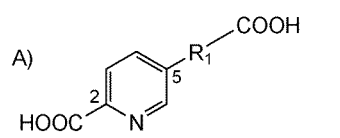
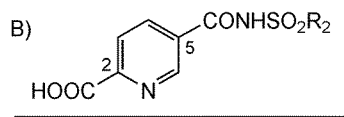
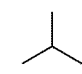
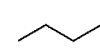
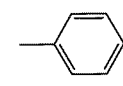
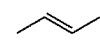
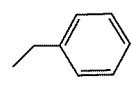
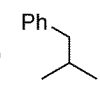
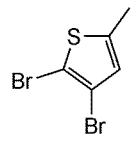
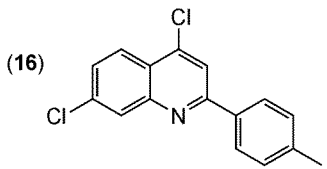
A)			B)		
					
Compound (R ₁)		IC ₅₀ (μM)	Compound (R ₂)		IC ₅₀ (μM)
(6)	None	5.5	(11)	CH ₃	1.8
(7)	CH ₂	9.6	(12)		1.6
(8)		9.6	(13)		1.1
(9)		10.6	(14)		3.0
(10)		27	(15)		8.5
			(16)		6.6

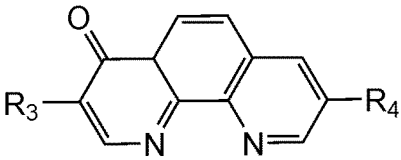
Table 3.3. Inhibition of avian P4H by pyridine-2,5-dicarboxylate and its derivatives. A) Variations of the distance between the C-5 carboxylic acid binding site and pyridine. B) The replacement of C-5 with acyl sulfonamides²⁴

suggesting the distal binding of the C-5 carboxyl group is flexible and allows various chain lengths to inhibit P4H. When the C-5 carboxyl group was replaced with several different acyl sulfonamides, an increase in potency was observed for most of the compounds tested (Figure 3.2B). The IC_{50} for the alkyl (**10,11**) or aryl (**12,13**) sulfonamide derivatives all had similar IC_{50} values; however very large substitutions of 2-(4,5-dibromothieryl) (**14**) and 4,7-dichloro-2-p-tolylquinoline (**15**) increased IC_{50} values to 8.5 and 6.6 μ M respectively. When the 2-carboxyl group was replaced with acyl sulfonamide, the IC_{50} value went up to 500 μ M. The substitution on the C-5 position of the pyridine 2,5-dicarboxylic acid is flexible and will allow for bulky phenyl groups without much effect on the inhibition; however modifications on the C-2 carboxyl group affect its ability to bind to iron. The pyridine-2,4-dicarboxylic acid compounds inhibit the activity of P4H by mimicking the binding of 2-oxoglutarate and preventing oxidative decarboxylation.²⁴ Results also suggest that the presence of carboxyl group at the 5 position effects the potency. Substituents at the 5 position do not influence the potency and suggests a large range of possible derivatives at the 5 position.²⁴

3.1.5.3. Phenanthroline Derivatives

Another type of inhibitor that mimics the binding of 2-oxoglutarate is a series of phenanthroline derivatives.²⁵ These phenanthroline compounds have been tested against isolated P4H and human foreskin fibroblast (HFF) cells for inhibition of collagen production (Table 3.4). The structures of the

positions in Table 3.3. An increased potency against isolated enzyme was observed in the phenanthroline derivatives with carboxylic acid groups at the R3 and R4 positions (**16**), as compared to derivatives with a single carboxyl group (**17**, **18**). The increase may be due to the interaction of residues Lys493 and His501 with the inhibitor, as found to stabilize 2-oxoglutarate and N-oxalylglycine. The most potent inhibitor against isolated P4H contained a nitro group at the R3 position and carboxylic acid at the R4 position (**19**). However, as seen in previous studies,^{23,24} inhibition of isolated enzyme may not translate into potency with in vitro and in vivo studies. When the dicarboxylic acid derivative (**16**) was tested against HFF cells, it had a notable increase in IC_{50} ($>20\ \mu M$), as did the nitro/carboxylic acid derivative ($R3=NO_2$, $R4=CO_2H$) (**19**) (value not determined). When the carboxyl group was replaced with a more lipophilic N-alkylamide group phenanthrolinone derivatives are given with modifications at the R3 and R4 (**20**), improved IC_{50} values were observed within HFF cells ($2.3\ \mu M$). The best phenanthrolinone derivative against cells was the $R3=NO_2$ (**21**) which had an observed IC_{50} value of $0.12\ \mu M$ against chick-tendon cells (not shown) and $1.1\ \mu M$ against HFF cells. Unfortunately, this compound was too insoluble for use for in vivo studies. Instead ($R3=CO_2H$) (**18**) and ($R3=CO_2H$, $R4=CONEtBu$) (**20**) derivatives were both tested in vivo for inhibition of collagen production in rats. Both compounds exhibited similar inhibition of collagen production, with maximal inhibition observed within the first two hours and sustained over the

		IC ₅₀ (μM)	
Compound		Isolated Prolyl 4-Hydroxylase	HFF cells
(16)	(R ₃ =CO ₂ H, R ₄ =CO ₂ H)	0.20	>20
(17)	(R ₃ =H, R ₄ =CO ₂ H)	1.3	>20
(18)	(R ₃ =CO ₂ H, R ₄ =H)	3.6	2.4
(19)	(R ₃ =NO ₂ , R ₄ =CO ₂ H)	0.038	NA
(20)	(R ₃ =CO ₂ H, R ₄ =CONEtBuH)	0.38	2.3
(21)	(R ₃ =NO ₂ , R ₄ =H)	0.12	1.1
(22)	(R ₃ =CO ₂ H, R ₄ =CONH ₂)	0.51	>20

NA, not available

Table 3.4. Inhibition of isolated P4H and HFF cells by phenanthroline derivatives.²⁵

next six hours until collagen production returned to normal after 22 hours.

This demonstrates how unprocessed collagen remaining in the ER until active P4H returns. With an oral dose (50mg/kg) given to rats, the phenanthroline derivative, collagen production was reduced, but it was not located in a specific region, as the uterus, ear and tail all experienced a similar reduction of collagen production. The low levels of toxicity and the in vivo and in vitro studies that have performed on the phenanthroline derivatives make these compounds a possible candidate for treating fibrosis.

3.1.6. Targeting the Endoplasmic Reticulum with the KDEL Receptor

Phenanthroline does not have any selectivity towards P4H, as it chelates any source of iron in the environment. One possible means of selectively targeting P4H would be drugs containing organelle-specific retention signal peptides. As mentioned previously, the hydroxylation of collagen by P4H occurs in the ER and is vital for the stability of collagen. Signal peptides are important for sorting and directing post-translational transport of proteins. The destination of proteins with a specific signal peptide can range from the nucleus, peroxisomes, ER, the trans-Golgi network, or secretion to the extracellular matrix. The human retention signal peptide for ER consists of four amino acids, lysine, aspartic acid, glutamic acid, and leucine (KDEL).^{26,27} This KDEL tag is located at the C-terminus of the β -subunit of P4H and retains the protein within the ER. The mechanism of retrieval of the KDEL-signal peptide secreted proteins is the binding of the tetrapeptide sequence to the KDEL receptor located in the Golgi apparatus (Figure 3.2).^{28,29} The KDEL receptor is a 26-kDa membrane-bound protein. Based on site-directed mutagenesis this protein has four known amino acids that are essential for the binding of substrate.^{30,31} Arg5, Asp50, Tyr162, and Asn165 are all involved in the formation of a hydrophilic binding pocket that binds KDEL ligands. Mutation of these residues demonstrated decreased binding of KDEL substrates with no difference in expression with respect to wild type.³⁰ Various sizes of substrates were used with the bulkier reagent biotin

maleimide, demonstrating a greater decrease in binding in Tyr162 and Asn165 as compared to Arg5 and Asp50.³⁰ This indicates Tyr162 and Asn165 are less accessible, and the locations of these residues are deeper inside the hydrophilic binding pocket. The binding of the KDEL-tagged proteins may also be pH-dependent. The KDEL receptor showed the highest binding affinity at pH 5.0, which suggests the importance of pH in substrate binding to the KDEL receptor.³² The ER is believed to have a pH similar to the cytosol (pH 7.4), while the cis-Golgi and the trans-Golgi have a pH of 6.4 and 5.8, respectively.³² The idea is, the KDEL tag of the secreted protein will bind

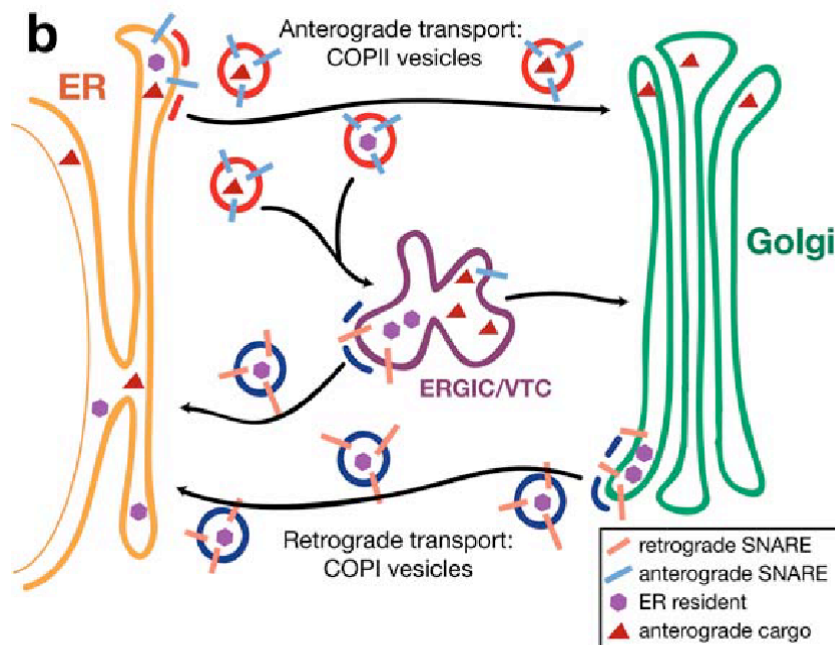


Figure 3.3. Mechanism of retrieval of the KDEL-signal peptide secreted proteins is the binding of the tetrapeptide sequence to the KDEL receptor located in the Golgi apparatus²⁸

to the receptor located on the trans-Golgi due to the low pH and be transferred to the ER, while at higher pH (7.4) the KDEL tagged protein will be released back into the ER.³² pH alone may not account for KDEL binding, but it is one factor in substrate binding, as it binds the trans-Golgi receptor under acidic conditions before transporting to the ER and releasing the substrate at pH 7.4 within the ER.^{30,32} This mode of substrate retention within a specific organelle could aid in drug design, as the retention signal will provide the ability to target enzymes located inside these organelles.

3.1.7. BODIPY^{581/591} Targeting the Endoplasmic Reticulum.

The concept of directing small molecules to organelles using a peptide retention signal was demonstrated by using signal peptide labeled BODIPY^{581/591} compound.³³ This fluorophore was covalently linked to several different retention signals and the uptake was observed through fluorescence microscopy.³³ The retention signals observed includes AKL for the peroxisome,³³ KKKRK for the nucleus,³³ and KDEL for the ER.³³ The uptake of the retention signal was very rapid, occurring in less than 1 minute, with complete localization after 16 minutes. The process of targeting the ER was confirmed with a co-localization study of the known ER marker concanavalin A. Targeting the ER with cell permeability small molecules could potentially be used in therapeutic drug delivery by targeting enzymes specific to the ER.

3.1.8. Literature Examples of Retention Signals Involved in Drug Design

3.1.8.1. HIV-1 Nuclear Import

Drug delivery based on these specific recognition signals has gained much attention. Two major advantages are as follows: a) localization of the drug at the same site as the protein it inhibits or b) blocking the protein from interacting with its specific retention signal receptor and therefore preventing the protein from reaching the proper organelle. The latter process could be very useful in anti-HIV therapy, as drugs could be designed to target the nuclear transport of mRNA.³⁴ The nucleus contains a selectively-permeable envelope for active transport of nuclear specific proteins by the nuclear localization signals (NLS). The first peptide sequence identified for the selective nuclear localization is a basic stretch of amino acids (KKKRRK).^{35,36} The search for effective HIV drugs rapidly changes due to the process of HIV-1 reverse transcriptase replication, which allows for continuous mutations within its environment. A possible solution is inhibition of the viral integration and transcription that occurs within the nucleus by drugs that target the NLS.³⁷ Arylene bis (methylketones) are small molecule inhibitors of nuclear import and have been shown to reduce HIV-1 replication in primary macrophages and peripheral blood mononuclear cell cultures.^{38,39} This has the potential to stop viral integration and transcription by inhibiting the uptake of the pre-integration complex by nuclear import. Also, simian immunodeficiency virus in macaques has been used as a model for HIV.⁴⁰ Studies show that the antibodies produced by the macaques prevent import of the virus into the nuclear membrane.^{42,43} This process is still being studied,

but it demonstrates the potential for targeting the selective nuclear import, which could be used in anti-HIV therapy.

3.1.8.2. Screening for Protease Inhibitors

Recognition signal peptides are also currently used for the identification of inhibitors of trans-Golgi network (TGN) bound proteases.⁴¹ Proteases found in the TGN are involved in proteolytic processes of recently formed protein secreted from the ER.⁴² These TGN proteases recognize and cleave specific domains of proteins before the cleaved proteins enter secretory vesicles and are sent out into the cytoplasm.⁴³ Two families of TGN proteases include prohormone convertase⁴³ and β -site amyloid precursor protein-cleaving enzyme.⁴⁴ These proteases contribute to the development of various diseases, including: Alzheimer's disease, arthritis, propagation of viruses, and proliferation of cancerous tumors.⁴⁸⁻⁵⁰ An assay to screen protease inhibitors was developed for the quantification of protease activity. The significance of this assay was the recombinant expression of a reporter containing the TGN retention signal (SDYQRL) and a protease cleavage sequence with alkaline phosphatase tag. The chimeric reporter was localized in the TGN by the retention signal, then protease activity was monitored by the cleavage of the reporter and secretion of the alkaline phosphatase tag into the extracellular media. This assay has been used to screen nearly 39,000 compounds for inhibition of the protease furin, which is involved in tumorigenesis, viral propagation of avian influenza, ebola and HIV, and

activation of anthrax. The protease involved in BACE cleavage, which leads to Alzheimer's disease, was also screened to identify potential inhibitors. The use of the TGN retention signal allows for a real-time and noninvasive assay of protease activity, which until to now has been difficult with the low pH and high Ca^{2+} environment of the TGN.

3.1.8.3. Gene Therapy

The replacement of a defective human gene or the introduction of new genes is known as gene therapy. Interest in gene therapy has increased in recent years.⁴⁶ One of the major barriers to the incorporation of exogenous DNA is transportation through the extracellular matrix, the cell membrane, and the nuclear envelope. One common solution to this problem has been using viral machinery to transfer genetic information into the nucleus. However, the linkage of a nuclear retention signal to therapeutic DNA could provide a nonviral approach to gene therapy.⁵¹ DNA entry into the cell would be enhanced by antibodies on the therapeutic gene that are specific to the cell membrane or amphiphilic peptides. The final entry step, into the nucleus, would be accomplished through utilization of the NLS. DNA injected directly into the nucleus resulted in 50-100% transfection.⁴⁵ When DNA was injected directly into the cytoplasm, however, no transfection occurred, displaying the selectively impermeable nature of the nuclear envelope. To cross the nuclear barrier, DNA was attached to synthetic NLS peptides mostly consisting of PKKKRKV retention sequence.^{46,47} The NLS could be linked to

DNA through a covalent linkage or noncovalent electrostatic interactions of the cationic residues in the NLS with the negatively charged DNA. Unnatural peptide backbones, known as peptide nucleic acids, also have advantages in a sequence-specific nuclear retention site. A 150-fold increase in expression was observed with a 3.4-kb linear fragment covalently linked to NLS-containing peptides.⁴⁷ Increased expression was also seen in plasmid DNA noncovalently linked to NLS; a 10-fold increase of β -galactosidase reporter gene expression was observed when noncovalently linked to NLS.⁵⁰ Peptide retention sequences used in assay development and in gene therapy display the emerging therapeutic possibilities of signal recognition peptides.

3.1.9. Phenanthroline Derivate Targeting the ER for the Inhibition of Collagen.

With the damaging effects of fibrosis reaching many people, an effective treatment for this disease is critical. A treatment may be possible with new techniques in drug design. Early reports describe the possible drug targets that mimic 2-oxoglutarate binding to Fe^{II} .²³⁻²⁵ Many of these drugs have IC_{50} values in the lower μM concentration, even in in vitro and in vivo studies. These inhibitors demonstrate the importance of drug design and considering cellular aspects of drug delivery; as many potent inhibitors were not lipophilic enough to cross the cell membrane. This chapter describes the synthesis and in vitro study of a phenanthroline derivative for the targeting the endoplasmic reticulum for inhibition of collagen production by P4H. The

phenanthroline derivatives were coupled to the ER retention signal KDEL with the hope of targeting within the ER. The phenanthroline derivatives were promising as potential inhibitors for several reasons:

- 1) Both in vitro and in vivo studies have been performed with no toxic effects.²⁵
- 2) Modifications to both the C2 and C5 positions are known in the literature, allowing phenanthroline to be coupled to the retention peptide signal relatively easily.⁴⁸⁻⁵⁰
- 3) Hydrophobic aromatic rings on phenanthroline increase ability to cross the cell membrane.²⁵

This chapter also describes various collagen assays performed to optimize the collagen production screening process.

3.2. Materials and Methods

Reagents involved with synthesis were purchased from Sigma-Aldrich (Milwaukee, WI) or Fisher Scientific (Pittsburgh, PA) unless otherwise stated. All amino acids and resin were purchased from Novabiochem (Gibbstown, NJ) with the exception of Fmoc-Glu-OH, which was purchased from AnaSpec (San Jose, CA).

3.2.1. Synthesis of 1,10-phenanthroline-1-oxide

Synthesis of 1,10-phenanthroline-1-oxide followed the published procedure with minor modifications.⁵¹ 1,10-phenanthroline monohydrate (25.0 g, 0.125 mol) was dissolved into 40 mL of glacial acetic acid. 15 mL of

30% hydrogen peroxide was added dropwise and stirred for 3 hours at a temperature of 72 °C. After the initial 3 hours, an additional 15 mL of 30% hydrogen peroxide was added dropwise and the reaction was stirred for 3 more hours. The solution was removed from the heat, 15 mL of 30% hydrogen peroxide was added, and the solution was allowed to stir for 18 hours. The solution was neutralized to pH ~ 10 with saturated potassium hydroxide. The product was extracted with several portions of chloroform and dried with anhydrous sodium sulfate. Solvent was removed under reduced pressure to give a tan solid of 15 g. (60% yield) ^1H NMR (δ /ppm, in CDCl_3): 7.75 (m, 2H), 7.85 (m, 2H), 7.98 (m, 1H), 8.31 (m, 2H), 8.4 (d 1H), 9.32 (m, 2H). ^{13}C NMR (δ /ppm, in CDCl_3): 117.46, 124.20, 125.77, 126.34, 129.26, 129.85, 133.51, 136.35, 137.30, 145.36, 146.77, 151.31. ESI-MS: m/z = 197.1 (MH^+).

3.2.2. Synthesis of 2-Cyano-1,10-Phenanthroline

Synthesis of 2-cyano-1,10-phenanthroline followed the published procedure with minor modifications.⁵⁶ 1,10-phenanthroline-1-oxide (2.7 g, 13.4 mmol) and potassium cyanide (2.7 g) were dissolved in 50 mL of water. Benzoyl chloride (3.76 g, 3.1 mL) was added dropwise via addition funnel, and the reaction stirred for 2 hours. During that time, a brown precipitate formed in solution. At the completion of 2 hours, the precipitate was collected by suction filtration and dried to yield brown solid (1.5 g, 56% yield). ^1H NMR (δ /ppm, in CDCl_3): 7.67 (m, 1H), 7.77 (m, 1H), 7.89 (d, 2H), 8.24 (m, 1H), 8.34

(d 1H), 9.21 (d, 1H). ^{13}C NMR (δ /ppm, in CDCl_3): 117.33, 124.16, 125.71, 126.24, 129.21, 129.86, 133.37, 136.45, 137.29, 145.18, 146.49, 151.18. ESI-MS: $m/z = 206.1$ (MH^+).

3.2.3. Synthesis of 2-Carboxy-1,10-Phenanthroline

Synthesis of 2-carboxy-1,10-phenanthroline followed the published procedure with minor modifications.⁵¹ 2-cyano-1,10-phenanthroline (2.63 g, 1.28 mmol) was dissolved in 15 mL of 95% ethanol, while sodium hydroxide (2.10 g) was dissolved in 15 mL of water. The sodium hydroxide solution was added to the 2-cyano-1,10-phenanthroline solution, and it was allowed to reflux for 2 hours. The ethanol was removed under reduced pressure, and the solution was made acidic with concentrated HCl solution, forming a brown precipitate. The brown solid was filtered and dried to yield 1.7 g of the desired product (65% yield). ^1H NMR (δ /ppm, in CDCl_3): 7.76 (m, 1H), 7.86 (m, 1H), 8.37 (m, 2H), 8.02 (t, 2H), 8.34 (d, 1H), 8.45 (d 1H), 9.31 (d, 1H). ^{13}C NMR (δ /ppm, in CDCl_3): 124.33, 124.97, 127.94, 128.30, 129.43, 130.57, 138.86, 142.55, 146.87, 147.72, 165.58. ESI-MS: $m/z = 225.1$ (MH^+).

3.2.4. Synthesis of Peptide Inhibitor 1,10-Phenanthroline-2-Glycine-Lysine-Aspartic Acid-Glutamic-Acid-Leucine (Phen-2-GKDEL)

All of the described peptide syntheses were performed with a ChemGlass peptide synthesizer (Vineland, N.J.). All peptide synthesis reactions were performed using the following procedure (Scheme 3-1). Wang resin (0.25 mmol) was added to the peptide synthesizer and swelled with 4

mL dimethylformamide (DMF) by continuously bubbling air through the fritted filter. DMF was removed and, in order to remove the Fmoc protecting group from the resin, 20% piperidine in DMF (4 mL) was added to the resin and stirred by bubbling for 30 min. Following deprotection, the solution was removed and the resin was washed by bubbling with several portions of DMF. Following DMF removal, 4 equivalents of Fmoc-protected amino acid (1 mmol) were added along with 4 equivalents of the activator O-Benzotriazole-N,N,N',N'-tetramethyl-uronium-hexafluoro-phosphate (HBTU) (1 mmol), and dissolved in 4 mL of 8% N,N-diisopropylethylamine (DIPEA) in DMF. The Fmoc-protected amino acid was stirred by bubbling air through the fritted filter for 1 hour. After the amino acid was coupled to the resin, the solution was removed, and the resin was washed and stirred with several portions of DMF. 20% Piperidine in DMF (4 mL) was added to deprotect the Fmoc group of the last amino acid coupled on the resin. The procedure was repeated until the desired peptide chain was complete. The P4H inhibitor 2-carboxyl-1,10-phenanthroline was coupled to the N-terminus of the peptide resin using the same coupling technique. The resin was dried, and peptides were cleaved from resin with 10 mL of 95/5% trifluoroacetic acid (TFA) in water. Cleavage conditions also removed protecting groups from any side chains present. The TFA solution was removed with a gentle flow of air, leaving a yellow oil product. Cold diethyl ether was added to precipitate the peptide as an off-white solid. The crude product was purified

by HPLC (Shimadzu) on a Jupiter 4-Proteo prep column (Phenomenex) with average yield of pure peptide of 30 -40 %. HPLC solvents were eluent A, 0.1 % TFA-H₂O and eluent B, 0.1 % TFA- CH₃CN with gradient conditions of 5 to 35 % B over 60 min.

The three step synthesis of the 2-carboxyl-1,10-phenanthroline from 1,10-phenanthroline was accomplished. Each step of this synthesis had moderate to good yields of 40 – 80 %, and was confirmed with NMR and ESI mass spectrometry. Standard peptide synthesis techniques allowed for easy coupling to the peptide on Wang resin. The peptide retention signal was synthesized on solid support, building from the C terminus to the N terminus (Scheme 3-1). This process began with the deprotection of the Wang resin with 20 % piperidine in DMF, followed by the addition of the first amino acid. Each amino acid was then deprotected with 20 % piperidine in DMF before the subsequent addition of the next amino acid. 2-Carboxy-phenanthroline was coupled on the N-terminus and the peptide chain and protecting groups (O^tBu and Mtt) were cleaved from the resin with 95/5 % TFA/H₂O. Dipsi 2-D NMR (δ /ppm, DMSO-d₆): glycine C-2 ¹H, 4.13, 4.27, leucine C-2 ¹H, 4.17, lysine C-2 ¹H, 4.26, glutamic acid C-2 ¹H, 4.33, aspartic acid C-2 ¹H, 4.58.

3.2.5. Fluorescence Detection of 1,10-Phenanthroline-2-Glutamic acid- γ -[2-(1-sulfonylnaphthyl)aminoethylamide]-Valine-Lysine-Aspartic Acid-Glutamic-Acid-Leucine {Phen-2-E(EDANS)VKDEL} in ER

HFF cells were grown to 60 % confluency in Nunc Lab Tek chambered cover glass 8 well plates (Fisher) with 0.3 mL of Iscove's Modified Dulbecco's Medium (IMDM) with heat-inactivated fetal bovine serum (FBS), 100 units/mL of penicillin and 50 μ g/mL of streptomycin at 37 °C in an incubator containing an atmosphere of air/CO₂ (95:5). The media was replaced with 0.3 mL of potassium buffered saline (PBS) buffer pH 7.4, at 37 °C for 30 min preceding the experiment. During the experiment, cells were placed in temperature controlled confocal microscope chamber set at 37 °C in the atmosphere of air/CO₂ (95:5). The PBS was removed, and 0.3 mL of fresh PBS containing 20 μ g/ml of phen-E(EDANS)VKDEL was added and incubated for 20 min. The fluorescence peptide probe solution was then removed, and the cells were washed with 0.3 mL of PBS and imaged on the confocal microscope. The cells were washed for a second time with 0.3 mL PBS before being treated with 1 μ M of ER Tracker Red (Invitrogen) in PBS and imaged on the confocal microscope. Fluorescence imaging was performed at the microscopy and analytical imaging lab at the University of Kansas on an inverted laser scanning microscope with Olympus/3I spinning disk confocal/TIRF inverted microscope. The two-channel fluorescence excitation/emission ratio for the fluorescence labeled inhibitor was 341 nm/471 nm, and the ER Tracker Red excitation/emission was 587 nm/615 nm. Co-localization analysis studies were performed with the fluorescence probe and the ER tracker to confirm the localization of the peptide probe into

the ER. The co-location study was performed using the Image J⁵¹ JACoP⁵² plug-in with the following equations:

$$r_P = (S_i ((A_i - a) \times (B_i - b))) / \dots (S_i (A_i - a)^2 \times S_i (B_i - b)^2)$$

Equation 3.1 Pearson's coefficient⁵²

$$r = (S_i (A_i \times B_i)) / \dots (S_i (A_i - a)^2 \times S_i (B_i - b)^2)$$

Equation 3.2 Overlap coefficient⁵²

$$r^2 = k_1 \times k_2 \text{ with } k_1 = (S_i (A_i \times B_i)) / (S_i (A_i)^2) \text{ \& } k_2 = (S_i (A_i \times B_i)) / (S_i (B_i)^2)$$

Equation 3.3 k_1 and k_2 coefficients⁵²

$$k_1 = (S_i (A_{i, \text{coloc}})) / (S_i A_i) \text{ \& } k_2 = (S_i (B_{i, \text{coloc}})) / (S_i B_i)$$

With $A_{i, \text{coloc}}$ being A_i if $B_i > 0$ and 0 if $B_i = 0$; and $B_{i, \text{coloc}}$ being B_i if $A_i > 0$ and 0 if

$$A_i = 0$$

Equation 3.4 M_1 & M_2 coefficient⁵²

3.2.6. Expression and Purification of Recombinant Human-P4H

Plasmid pBAD+ containing the human-*p4h* gene (cDNA of human P4H a(I) subunit (UltimateTM ORF clone IOH26865, Invitrogen) was transformed into origami DE3 cells (Novagen). Cells were inoculated into 1.5 L Luria-Bertani (LB) media with 150 mg ampicillin and grown to an O.D.₆₀₀ < 0.2 at 37 °C with agitation at 225 rpm. At O.D.₆₀₀ < 0.2, isopropyl-1-thio-β-D-

galactopyranoside (IPTG) was added to a final concentration of 0.1 mM for the induction of PDI. The temperature was reduced to 25 °C, and cell growth was continued to O.D.₆₀₀ = 0.6. This point, arabinose was added to a final concentration of 0.02 mM for the induction of catalytic α -subunit of P4H. Temperature was reduced to 20 °C cultures were allowed to grow overnight. The cells were harvested by centrifugation (Beckman) at 4 °C and 6 000 x g for 30 min and resuspended in a buffer (10 mM Tris, 100 mM glycine, and 100 mM sodium chloride, pH 7.8). Cell lysis was performed in an ice bath by 20 cycles of ultrasonication where each 20 cycle consists of 0.8 second pulses with 0.5 second gaps in between. The solution was allowed to cool for 5 minutes between each cycle. Cell debris was removed by centrifugation (Beckman) at 40,000 x g for 30 min. The supernatant was collected and loaded on poly-L-proline affinity column⁵³ and washed with 3 column volumes of buffer (10 mM Tris, 100 mM glycine, 100 mM sodium chloride pH 7.8). Protein was eluted from the column with the elution buffer (5 mg/mL poly –L-proline, 10 mM Tris, 100 mM glycine, 100 mM sodium chloride, pH 7.8). Fractions were collected and dialyzed with 3 batches of 4 L buffer (25 mM sodium phosphate, 10 mM glycine, 50 mM sodium chloride, pH 7.8) first every 2 hours and then overnight. Protein was loaded on a HiTrap QFF anion exchange column (Amersham Biosciences), and washed three column volumes of binding buffer (25 mM sodium phosphate, 10 mM glycine, 50 mM sodium chloride, pH 7.8) then eluted with a linear gradient (50 mM NaCl to

430 mM NaCl) on an FLPC (Amersham Biosciences) . Fractions were collected, concentrated to 1 mL and loaded on the FPLC size exclusion column Hiload 16/60 Superdex 200 pg (Amersham Biosciences) and eluted with buffer (10 mM Tris, 100 glycine, 100 mM NaCl, pH 7.8). Protein purity was confirmed with SDS-PAGE, and concentration was determined using bicinchoninic acid (BCA) assay.⁵⁴

3.2.7. Preparation of (GPP)₁₀

(GPP)₁₀ was prepared using a thioredoxin fusion protein previously expressed in the Limburg lab. Cleavage of thioredoxin from the fusion protein was performed by adding 1 μ L of enterokinase (Invitrogen) to 1 mL of 12 mg/mL of protein and incubating at 37°C (overnight). The cleaved protein was purified by size exclusion chromatography Hiload 16/60 Superdex 200 pg in 6 M urea. Urea was removed using a HiTrap desalting column (Amersham Biosciences). Fractions were collected and protein concentration was determined by the absorbance at 280 nm ($\epsilon = 5.5 \text{ mM}^{-1}\text{cm}^{-1}$).

3.2.8. Enzyme Activity Assay with Oxygen Electrode

The activity of the recombinant P4H was assayed with an Oxygraph oxygen electrode (Hansatech Instruments). The electrode is a Clark type polarographic oxygen sensor. The electrode is fitted at the bottom of the reaction vesicle, which was covered with a thin oxygen permeable polytetrafluoroethylene (PTFE) membrane. A polarizing voltage is applied

between the central platinum cathode and silver anode electrode. A small current is generated as oxygen diffuses across the membrane.

The inhibitors were dissolved in dimethylsulfoxide (DMSO), and when inhibitor was added to the enzyme/substrate mixture, the final DMSO concentration was ~ 0.2 %. Reaction conditions are 50 mM Tris, 750 μ M ascorbate, 10 μ M of Fe^{II}, 20 μ M of GPP₁₀, and 0.2 μ M of P4H, to a final volume of 500 μ L. Concentration ranging from 5 - 60 μ M phenanthroline and 100 – 5000 μ M phen-2-GKDEL were added. Reaction rate was determined by the consumption of O₂, and plotted as rate of O₂ consumption versus the log of inhibitor concentration. The IC₅₀ was determined with the following equation:

$$y = V_{\min} + (V_{\max} - V_{\min}) / (1 + 10^{(x - IC_{50})})$$

with x being inhibitor concentration

Equation 3-5 IC₅₀ curve⁵⁵

3.2.9. Quantification of Collagen Production from Soluble Collagen in Media

The hydroxylation of collagen was measured by the production of soluble collagen in the media of HFF cells. HFF cells (ATCC) were grown to confluency in 15 cm² flasks in IMDM media (ATCC) with 10% FBS (Gibco), 100 units/mL of penicillin and 50 μ g/mL of streptomycin, at 37 °C in an incubator containing an atmosphere of air/CO₂ (95:5). At the point of full confluency, the media was removed and cells were incubated for 24 hours

with serum free medium (1 mL), 30 µg/mL ascorbate, penicillin, and streptomycin. Following incubation, the medium was again removed and replaced with fresh serum free media with ascorbate, penicillin, streptomycin for another 24 hour incubation. At this point, inhibitors, which were dissolved in DMSO, were added to the media. After 48 hours, the media was removed and diluted with binding buffer (0.1 M NaHCO₃, pH 10.0) and 100 µL of this solution was incubated in an ELISA plate (4 HBX Immunlon Plates, Thermo Scientific) overnight at 4 °C. Solution was removed, and the wells were washed three times with PBS buffer. 200 µL of 2% Blocker BSA (Pierce) in PBS buffer, pH 7.2, was added and incubated at room temperature for 1 hour. The wells were washed three times with 200 µL PBS. 100 µL of a 1:5000 dilution of mouse anti-collagen type I monoclonal primary antibody, unconjugated (abcam) was added to each well and incubated at room temperature for 30 minutes. The antibody was then removed and washed three times with 200 µL of PBS. Secondary antibody, donkey anti-mouse conjugated horseradish-peroxidase (Jackson ImmunoResearch), was added in a 1:1000 dilution in PBS, and 100 µL was added to each well and incubated for 30 minutes at room temperature. The secondary antibody was removed and the wells were washed with 200 µL PBS. The plate was developed with 100 µL of 1 mM 2,2'-azino-bis(3-ethylbenzthiazoline-6-sulphonic acid (ABTS) in citrate-phosphate buffer, pH 4.2, with 0.03% H₂O₂

monitoring at 415 nm absorbance on SpectraMax Plus plate reader (Molecular Devices).

3.2.10. Sircol Detection of Collagen Production

Detection of collagen by Sircol (Biocolor) followed the same cellular preparation procedure as the detection of collagen production with pepsin digest. After centrifugation of the 2M NaCl precipitated collagen, the supernatant discarded and 1 mL of sirius red dye was added to each tube. The tubes were capped and gently mixed at room temperature for 30 min. The tubes were centrifuged at 10,000 x g for 10 minutes to form a collagen-dyed pellet. After centrifugation, the supernatant was discarded, and the pellet was washed with 500 μ L of 200 proof ethanol. Bound dye was recovered with the addition of 1.0 mL of the Alkali reagent (Sircol). Samples were capped and mixed by vortex until all of the dye was solublized. 100 μ L samples were plated on a 96 well plate and observed on SpectraMax Plus plate reader (Molecular Devices) at 540 nm.

3.2.11. Detection of Collagen in Extracellular Matrix of HFF cells with Polyclonal Antibodies Against Human Collagen Type I

The hydroxylation of collagen was measured by the production of collagen in the extracellular matrix of HFF cells. HFF cells were grown to 95% confluency in a 6 well plate in IMDM media with 10% fetal-bovine serum, 100 units/mL of penicillin and 50 μ g/mL of streptomycin, at 37 °C in an incubator at the atmosphere of air/CO₂ (95:5). At the point of full confluency,

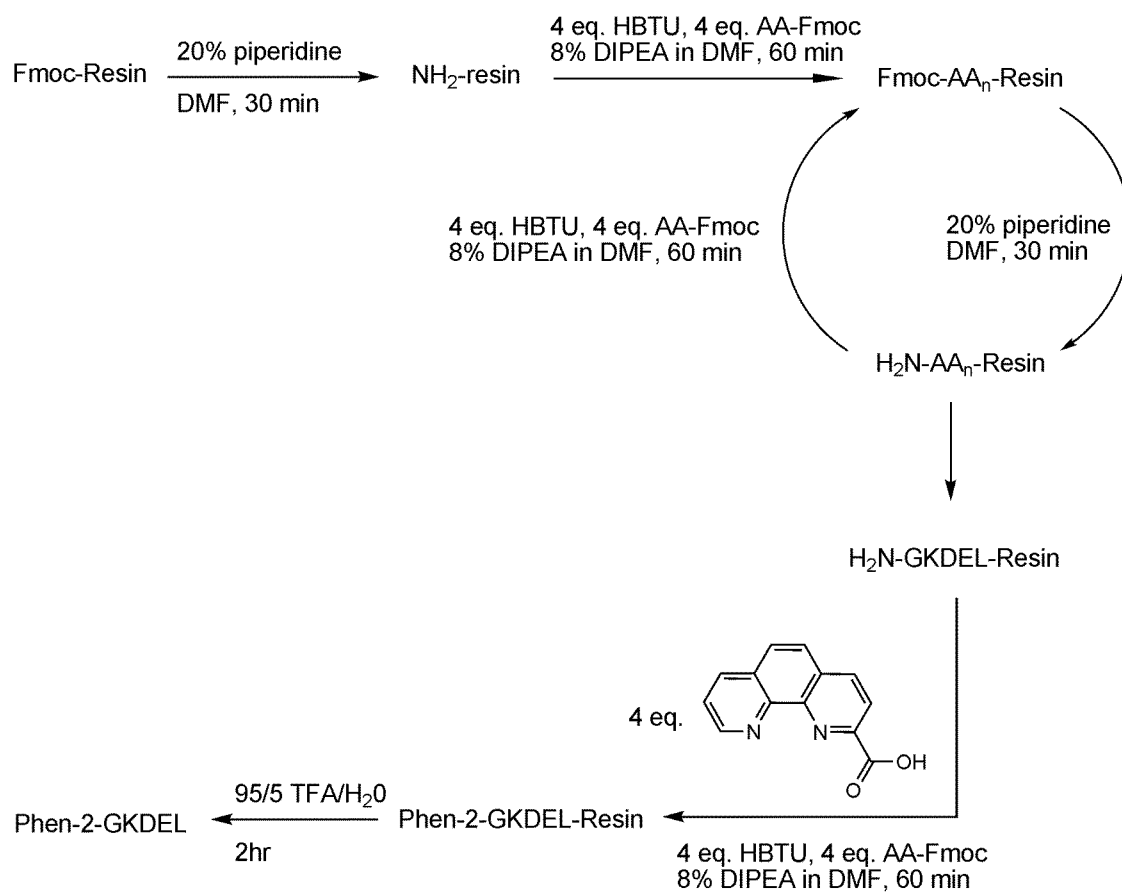
the media was removed, and cells were incubated for 24 hours in serum free medium (1 mL), 30 μ g/mL ascorbate, penicillin, and streptomycin. Following incubation, the medium was again removed and replaced with fresh serum free media with ascorbate, penicillin, and streptomycin for another 24 hour incubation. At this point, inhibitors dissolved in DMSO were added to the media. After 48 hours, the media was removed and replaced with 5 mg/mL pepsin from porcine gastric mucosa (Fisher) in 0.05 M acetic acid, pH 2.8. The cells were harvested by scraping cells and transferred into 1 mL eppendorf tubes with the pepsin solution and rocked overnight at 4 °C. The eppendorf tubes were centrifuged at 10,000 x g for 10 minutes (Eppendorf Centrifuge) to remove insoluble cell debris, and the supernatant was isolated. The soluble collagen in the supernatant was precipitated with 2 M NaCl and centrifuged at 10,000 x g for 10 min. The supernatant was discarded and the soluble collagen was redissolved in 100 μ L of 0.05 M acetic acid and coated in ELISA plate (4 HBX Immulon Plates, Thermo Scientific) and incubated overnight at 4 °C. Solution was removed and washed three times with PBS solution before 200 μ L of 2% Blocker BSA (Pierce) in PBS buffer, pH 7.2, was added and incubated at room temperature for 1 hour. The wells were washed three times with 200 μ l PBS. 100 μ L of a 1:5000 dilution of mouse anti-collagen type I monoclonal primary antibody, unconjugated (abcam) was added to each well and incubated at room temperature for 30 minutes. The antibody was then removed and the wells were washed three times with 200

μL PBS. 100 μL of the secondary antibody, donkey anti-mouse conjugated horseradish-peroxidase (Jackson ImmunoResearch), in a 1:1000 dilution in PBS, was added to each well and incubated for 30 minutes at room temperature. The secondary antibody was removed and the wells were washed with 200 μL PBS. The plate was developed with 100 μL of 1 mM 2,2'-azino-bis(3-ethylbenzthiazoline-6-sulphonic acid (ABTS) in citrate-phosphate buffer, pH 4.2, with 0.03% H_2O_2 at 415 nm on SpectraMax Plus plate reader (Molecular Devices).

3.3. Results

3.3.1 Synthesis of Inhibitors Containing the Fe-chelator Coupled to an ER-Retention Signal Peptide as Potential in vivo P4H Inhibitors

Two agents useful in exploration of selective in vivo inhibition of human-P4H were prepared by the method of Scheme 3.1. Their structures are shown in Figure 3.4A (phen-2-GKDEL) and Figure 3.4B (The fluorescent agent phen-2-E(EDANS)VKDEL). Each agent combines a chelating moiety, capable of inhibiting P4H by removal of essential Fe^{II} , combined with a signal-peptide moiety, capable of localizing the agents (and thus the inhibition) to the ER where P4H is located. In addition phen-2-E(EDANS)VKDEL contains a fluorescent moiety capable of visualization of the intracellular localization of the agents. Both were obtained in 99 % pure form with a final yield of 30 %. The peptide sequences in both inhibitors were confirmed with 2-D NMR and ESI mass spectrometry (Figure 3.5,6).



Scheme 3.1. The solid phase synthesis of the GKDEL retention signal. Each amino acid is coupled onto the Wang resin, building C-terminus to N-terminus.

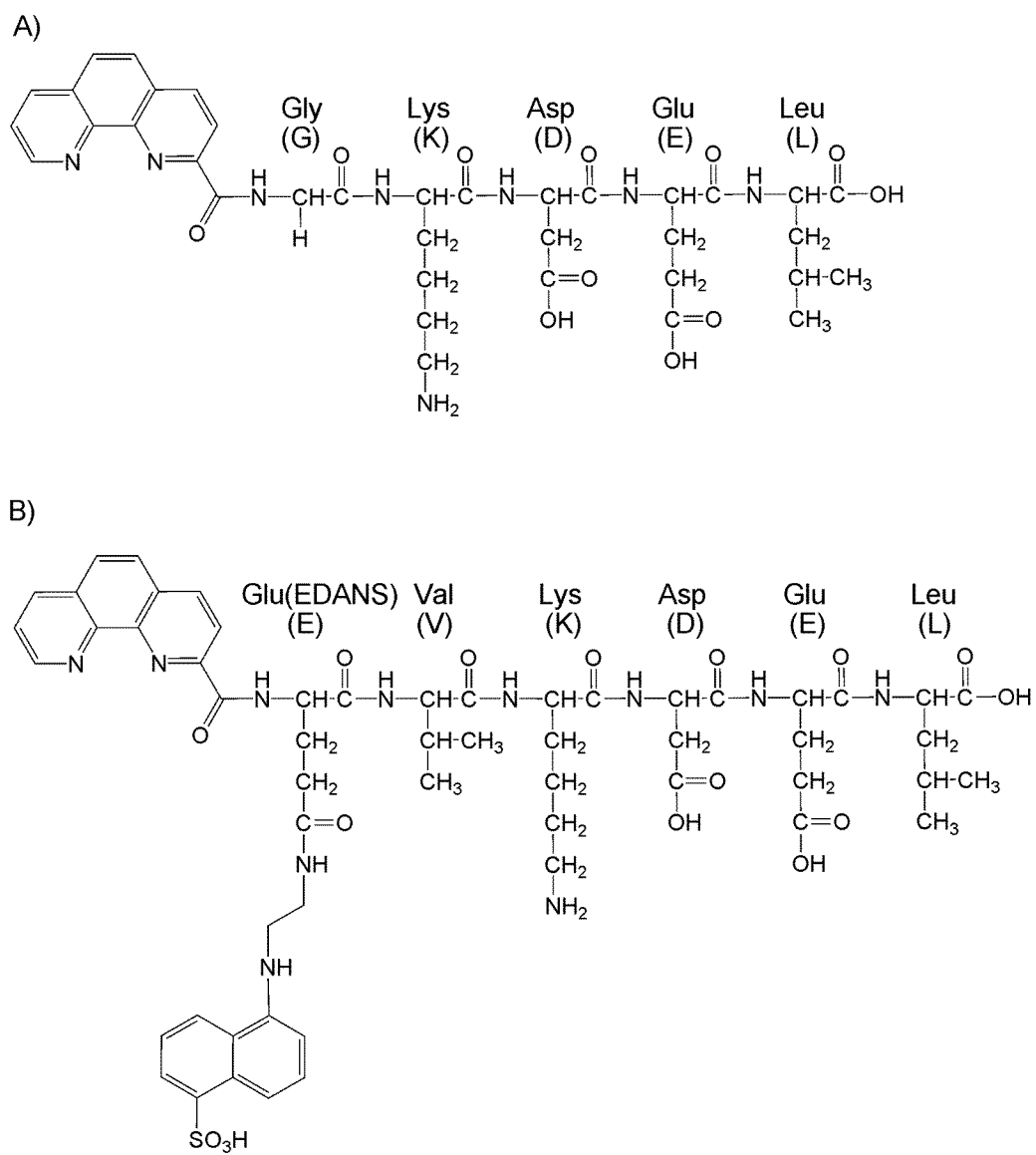


Figure 3.4. A) Phen-2-GKDEL B)Phen-2-E(EDANS)VKDEL

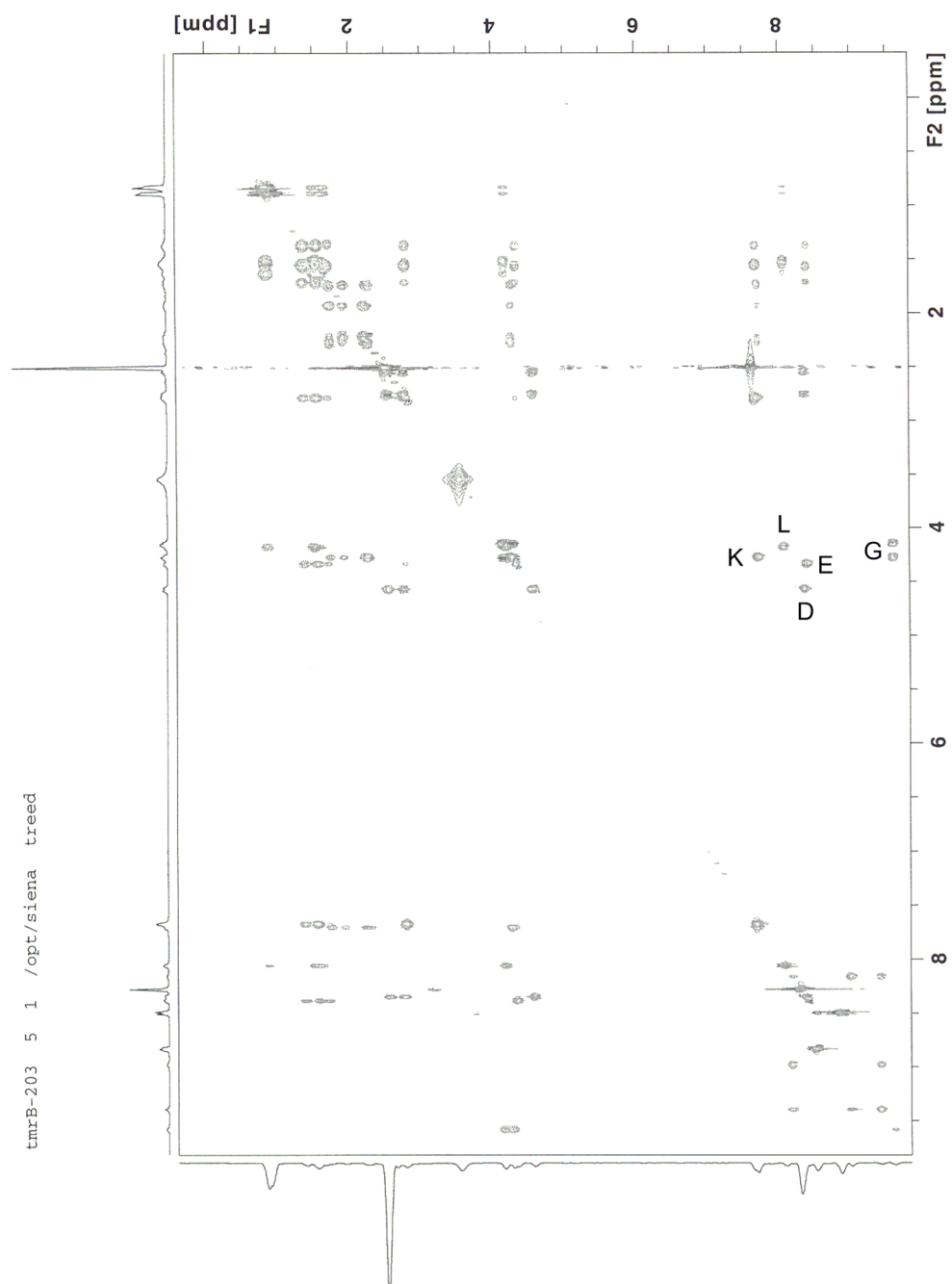


Figure 3.5. Dipsi spectrum of phen-2-GKDEL on Bruker 500 MHz NMR

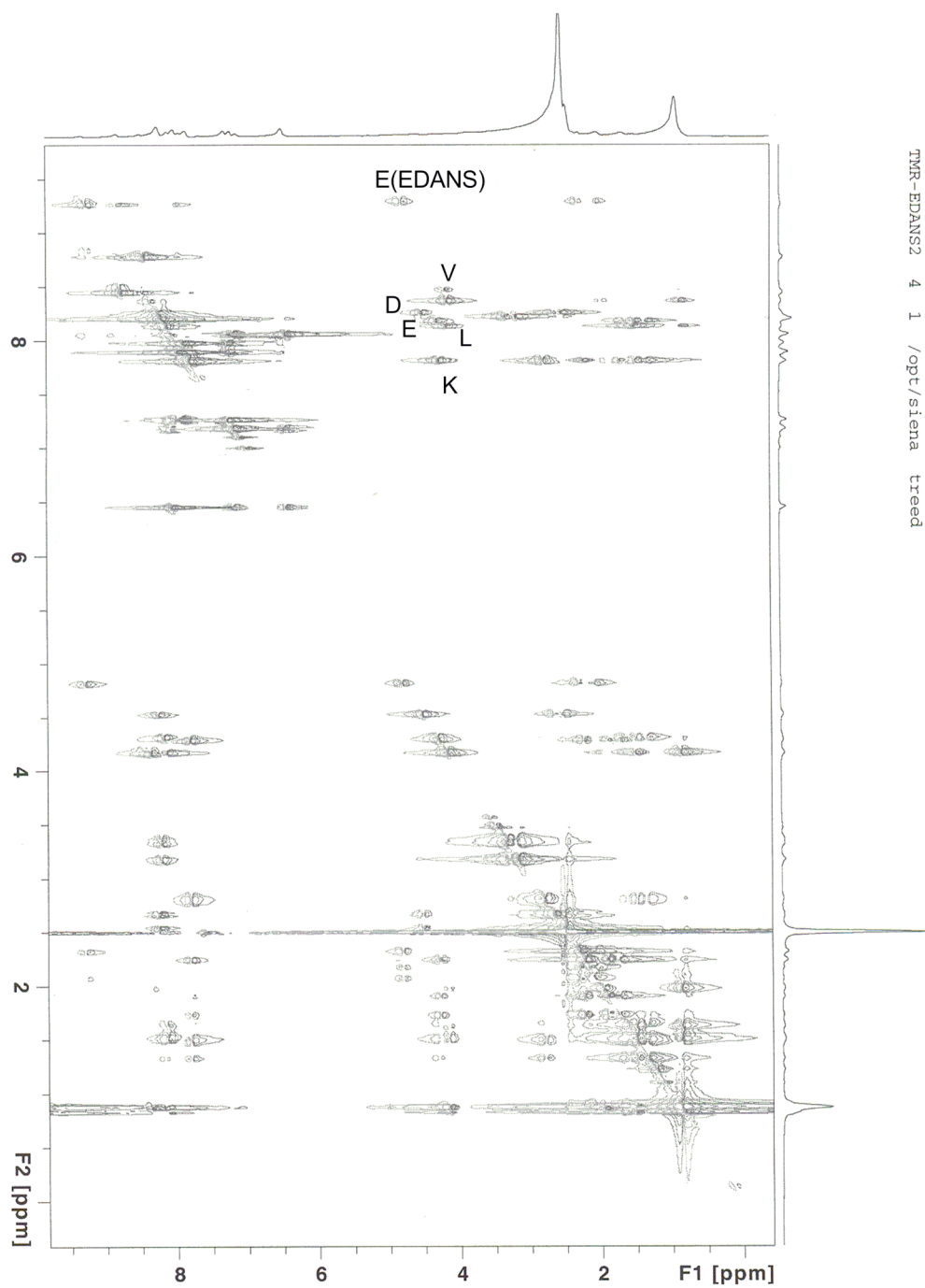


Figure 3.6. Dipsi spectrum of phen-2-E(EDANS)VKDEL on Bruker 500 MHz NMR

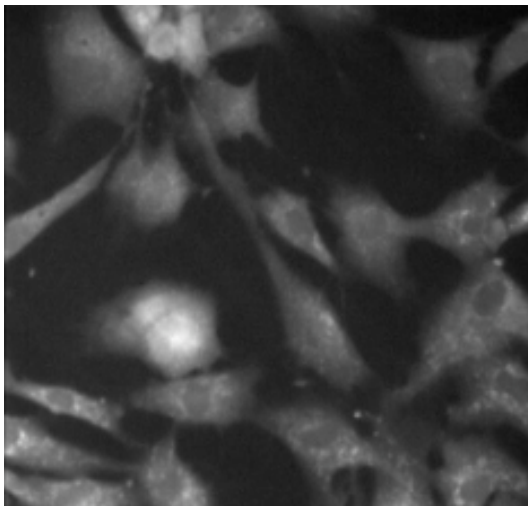
3.3.2. Phen-2-VD(EDANS)KDEL Localizes in the ER of HFF Cells

To observe the localization of the KDEL-labelled inhibitor into the ER of HFF cells, the EDANS fluorophore (AnaSpec)⁵⁶ was coupled on to the peptide chain, phen-2-E(EDANS)VKDEL. Localization of the KDEL fluorophore was confirmed with commercially available ER tracker. This cell-permeable agent utilizes two components, BODIPY fluorescent dye and glibenclamide. The agent is visualized by BODIPY fluorescent dye and localizes in the ER by glibenclamide. Glibenclamide is known to bind to the sulphonylurea receptors of ATP-sensitive K⁺ channels which are prominent on ER.⁵⁷ Careful consideration was taken towards the overlap of excitation and emission spectra to avoid bleed through. The excitation and emission for E(EDANS) is $\lambda_{\text{ex}} = 341$ and $\lambda_{\text{em}} = 471$,⁵⁸ while the excitation and emission for ER tracker red (Molecular Probes) is $\lambda_{\text{ex}} = 587$ and $\lambda_{\text{em}} = 615$.

At first, the fluorescence labelled inhibitor was distributed throughout the cell, but after 20 minute incubation and wash with PBS, the inhibitor was localized within the ER (Figure 3.7A). The co-localization and compartmentalization within the ER were confirmed with ER tracker Red (Figure 3.7B). ER tracker Red was immediately taken up within the ER. Analysis of subcellular co-localization was performed with Image J⁵¹ plug-in JACoP⁵² to confirm the import of fluorescence-labelled inhibitor into the ER (Table 3.5). Pearson's coefficient measures the dependency of pixels in a linear expression of the intensities of two images on each other.⁵² The range

of this value is centralized from 1 to -1, with complete positive correlation at 1, negative correlation is at -1 and no correlation at 0.⁵² The linear approximation of the two fluorophores and the goodness of fit were determined by JACoP with a Pearson's coefficient of 0.85.⁵² The Pearson's coefficient demonstrates good co-localization of the inhibitor fluorophore and the ER tracker. The overlap coefficient is calculated with Pearson's coefficient and the average intensities of both fluorophores. The overlap coefficient of 0.944 confirms good co-localization

A)



B)

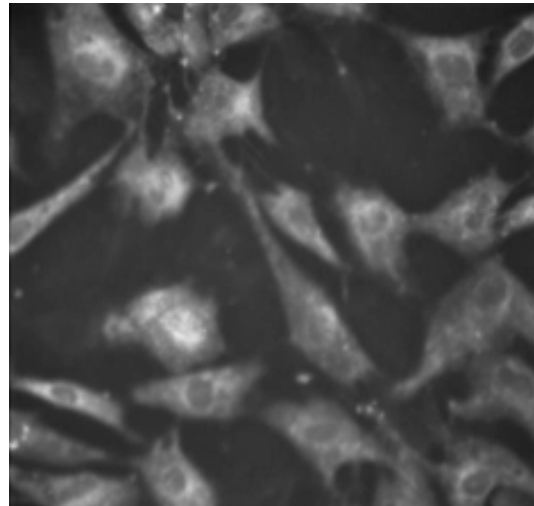


Figure 3.7. Fluorescence imaging of HFF incubated with A) phen-E(EDANS)VKDEL B) ER tracker.

Pearson's coefficient	85%
overlap coefficient	94.4%
k1 intensity of ER tracker Red	4.337
K2 intensity of phen-2-E(EDANS)VKDEL	0.228

Table 3.5. Quantitative analysis of the co-localization of ER tracker Red and phen-2-E(EDANS)VKDEL as performed with Image J⁵¹ plugin JACoP⁵²

of both fluorophores. k1 and k2 are two components that are included in the overlap coefficient and are related to the total intensity of each fluorophore.⁵² The intensity of ER tracker was approximately 20 times more intense than the inhibitor, with a k1 value of 4.337 versus a k2 value of 0.228. Co-localization and intensity correlation analysis (ICA) was performed (Figure 3.8) which helps for an interpretable representation of co-localization to determined coincidental events with two different dyes.⁵² The x-value of the graph is dependent on covariance of both fluorophores, while the y-value signifies the intensities of the independent channel.⁵² The spread of the dots on the left side of the are due to non-colocalization while the pixel clouds on the right side of the graph indicate partial co-localization. The “c” shape curves of both graphs indicate good co-localization of each fluorophore.⁵² Phen-2-

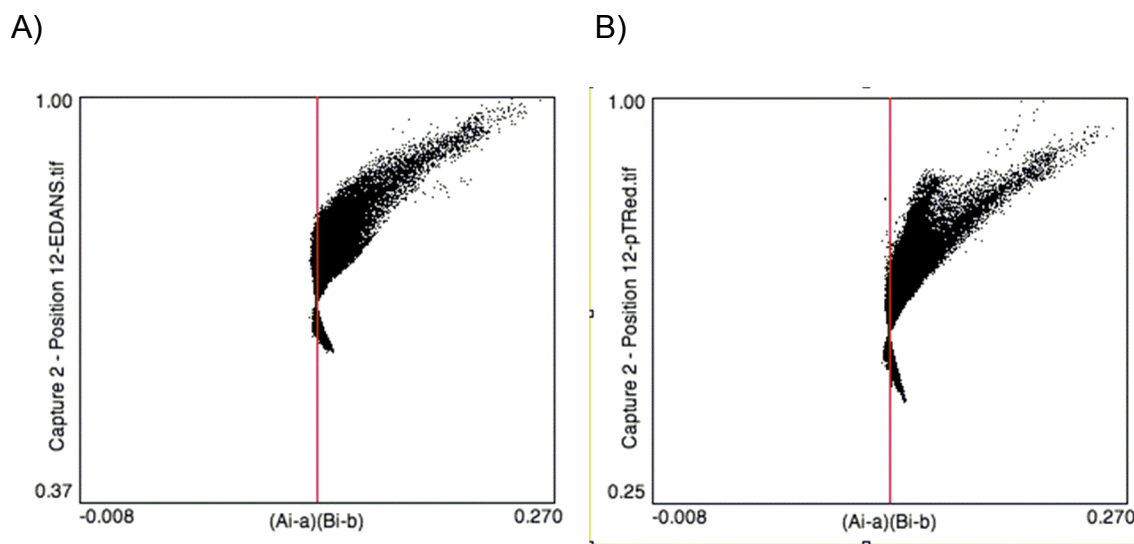


Figure 3.8. Co-localization and intensity correlation analysis of A) phen-E(EDANS)VKDEL and B) ER Tracker

E(EDANS)VKDEL and ER tracker colocalization studies were performed to prove that the inhibitor with the KDEL tag was being localized within the ER.

3.3.3. Phen-2-GKDEL demonstrates an IC_{50} value of 3.5 mM Inhibition Against Recombinant Human-P4H

IC_{50} values for phen-2-GKDEL were measured against our recombinant human-P4H. The recombinant P4H was produced to a yield of 1.0 mg/L, and its activity was determined to be the same as native P4H with a Clark oxygen electrode. SDS-PAGE confirmed the purity with a band at 77 kDa as is seen and the IC_{50} was determined by the following Equation 3.5.

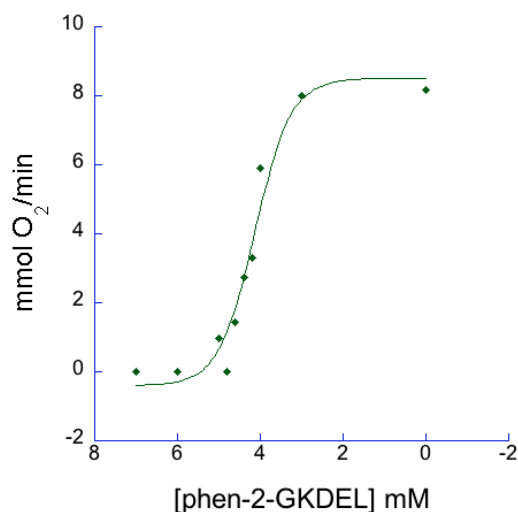


Figure 3.9. IC₅₀ curve of phen-GKDEL inhibition of the recombinant human-P4H.

Phen-2-GKDEL was tested from 100 – 8000 μ M with an IC₅₀ value of 3500 μ M (Figure 3.9).

3.3.4. Phen-2-GKDEL Demonstrates 250 μ M Inhibition in vitro with HFF Cells

Soluble collagen excreted into the media and collagen in the ECM were assayed to determine the inhibition of collagen by phen-2-GKDEL. Soluble collagen excreted into the media and collagen within the ECM were assayed with polyclonal antibodies towards human collagen type I or dye which covalently adheres to collagen type I to type V.

The first attempt to probe the effect of phen-KDEL towards inhibiting the collagen production was performed with ELISA to detect the soluble collagen that is secreted into the media. The media with the soluble collagen was removed after 48 hours of incubation with the inhibitor. The ELISA was performed on samples with phen-2-GKDEL (2 μ M) and control experiment was performed on samples with no inhibitor. The media of both the control and phen-2-GKDEL samples were diluted with a range of 80 % to 50 % media/ binding buffer (0.1 M NaHCO₃, pH 10.0) to determine the optimal concentration of antigen. In the graph of diluted collagen versus absorbance (Figure 3.10), both the control and the 2 μ M phen-2-GKDEL samples follow a linear expression. The control has approximately 1.5 –fold higher absorbance than phen-2-GKDEL, which suggests that collagen production is inhibited by phen-2-GKDEL.

Other method for collagen detection was employed to obtain higher concentration of collagen. The Sircol Assay utilizes Sirius red, which is an anionic dye with a sulphonic acid side chain (Figure 3.11), reacts with the basic amino acid side chains present in collagen. The advantage with this method is that mammalian collagen type I to type V can be all measured while the previous assay used a primary polyclonal antibody for type I collagen. Collagen was extracted from the extracellular matrix (ECM) and was digested with pepsin. Pepsin cleaves collagen into soluble proteins, but allows it to retain native triple helical structure that is necessary for detection.

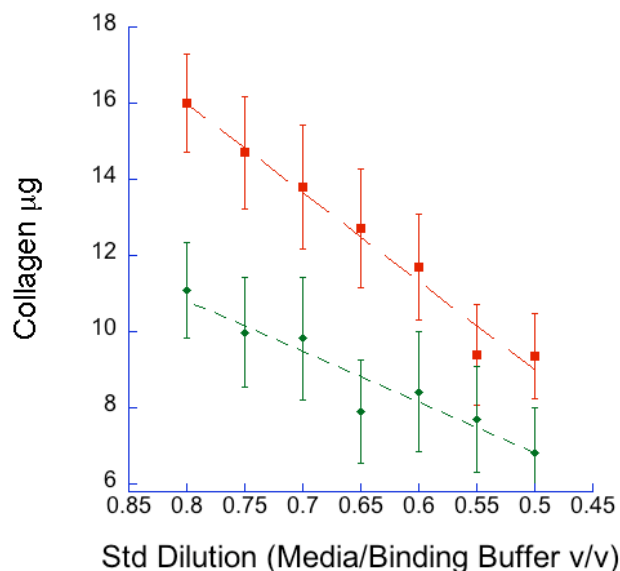


Figure 3.10. Collagen production by HFF cells with no inhibitor (red boxes) and phen-GKDEL (green diamonds). Media samples were diluted with binding buffer (0.1 M NaHCO₃, pH 10.0)

Once the collagen was solublized and isolated, the dye was added and placed on rocker to allow for binding. The dye-collagen complex was pelleted by centrifugation, and the dye was extracted with the Alkali reagent from the Sircol kit. Absorbance readings were taken on 96-well plate reader Spectra Max plus (Molecular Devices). We found that phen-2-GKDEL (20 µM) inhibits collagen production, as compared to the cells without inhibitor (Figure 2.12). IC₅₀ curves for phen-2-GKDEL were obtained with inhibitor concentrations ranging from 0.01-1000 µM. The collagen from the ECM was extracted and pepsin digested in the similar manner as the Sircol Assay as described in the

previous paragraph. After the soluble collagen was isolated, it was redissolved in 100 μL of 0.05 M acetic acid (pH 4.2), and the concentration of collagen was determined using an indirect ELISA method. As shown in Figure 3.13, IC_{50} values for phen-2-GKDEL were determined to be 250 μM .

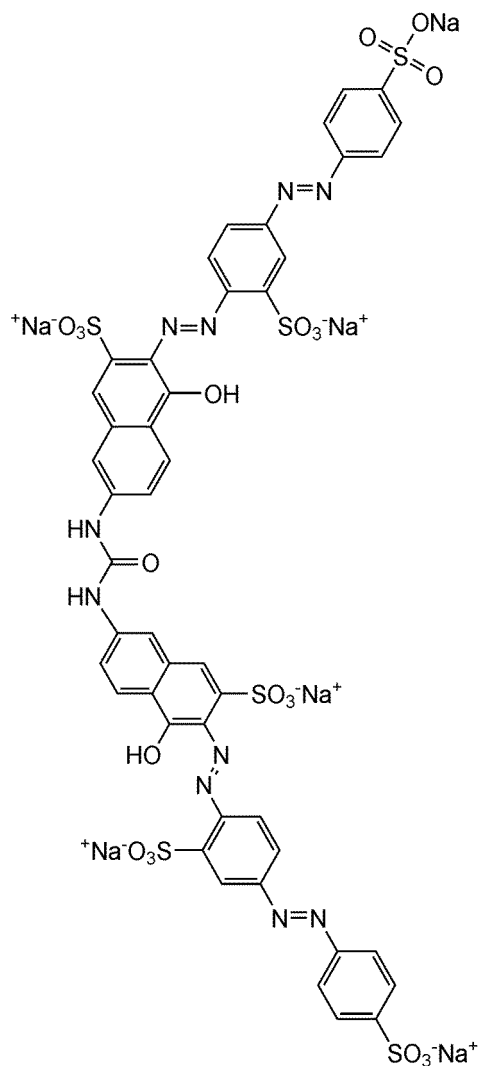


Figure 3.11. The chemical structure of the dye that covalently links to collagen types I through V in the Sircol Assay.

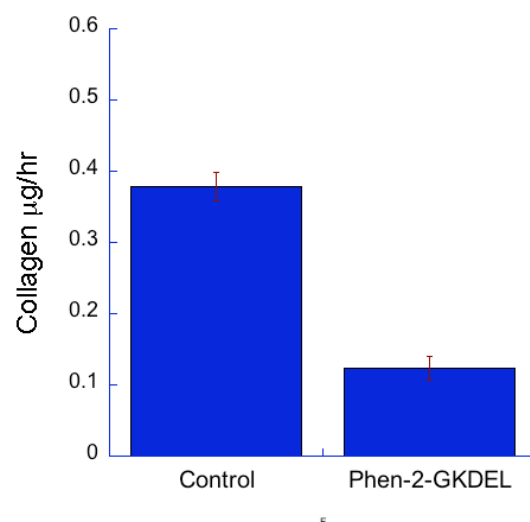


Figure 3.12. Sircol assay of pepsin digested collagen from HFF cells. (The standards are displayed on the left of the graph.) 20 mM phen-GKDEL was incubated with HFF cells for 48 hours.

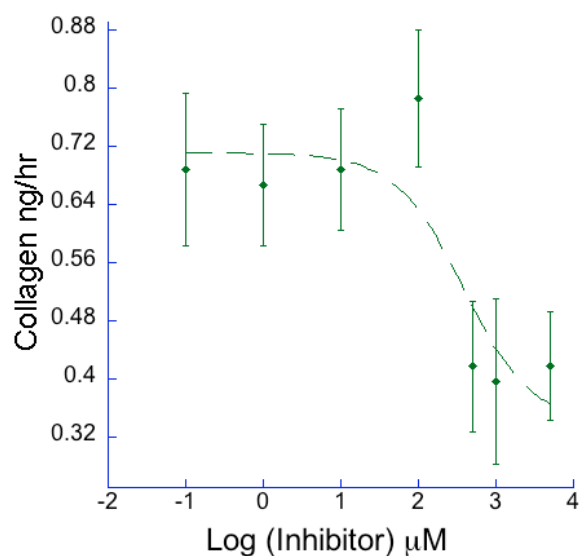


Figure 3.13. IC_{50} curve of phen-2-GKDEL (green diamonds) with pepsin digested collagen.

The control experiments using untagged 1,10-phenanthroline (phen) gave IC_{50} value of 160 μM . These results clearly show that the production of soluble and insoluble collagens are both inhibited by phen-2-GKDEL.

3.3.5. Phen is 100 Times More Potent than Phen-2-GKDEL for recombinant P4H enzyme

IC_{50} values for phen were also measured against recombinant P4H in comparison with Phen-2-GKDEL. Phen inhibition of recombinant P4H was assayed at a concentration range of 5 – 60 μM (Figure 3.14). The IC_{50} for phen was

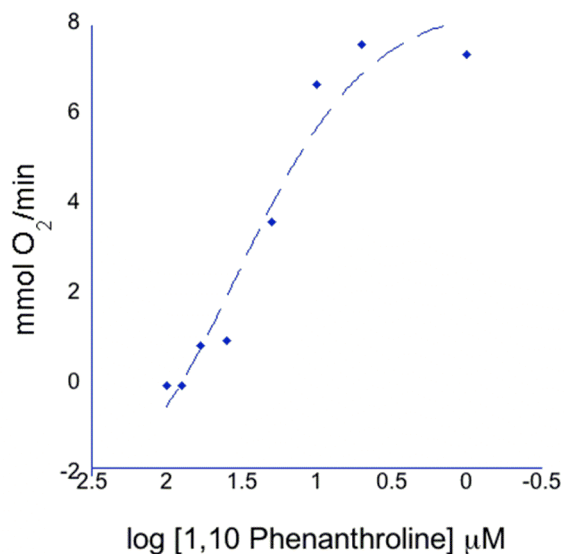


Figure 3.14. IC_{50} curve of inhibition of recombinant human-P4H with phen.

calculated at 35 μM . At high concentrations of phen, a reddish precipitate was present in the reaction mixture. This precipitate is likely an Fe^{III} adduct that was insoluble in the buffer solution. The comparison of phen with phen-2-GKDEL demonstrated a 100 times more potency against isolated P4H enzyme. Further experiments were performed to test the potency of phen against phen-2-GKDEL with collagen production in HFF cells.

3.3.6. Phen-2-GKDEL IC_{50} Value of 250 μM is Similar to Phen IC_{50} value of 160 μM in vitro with HFF cells

To evaluate the effect of phen-2-GKDEL for inhibiting the collagen production in HFF cells, collagen production was compared to the unmodified phenanthroline. Both soluble collagen excreted to the media and collagen in the ECM were assayed.

Both phen-2-GKDEL and phen for soluble collagen excreted into the media by HFF cells at a fixed concentration of 2 μM . Figure 3.15 shows the linear slope for detecting the secreted soluble collagen in the media upon dilution with a range of 80 % to 50 % media/ binding buffer (0.1 M NaHCO_3 pH 10.0). The graph suggests that both phen and phen-2-GKDEL inhibit collagen production where that latter is more effective to achieve ~ 30 % inhibition (~ 25 % inhibition using phen).

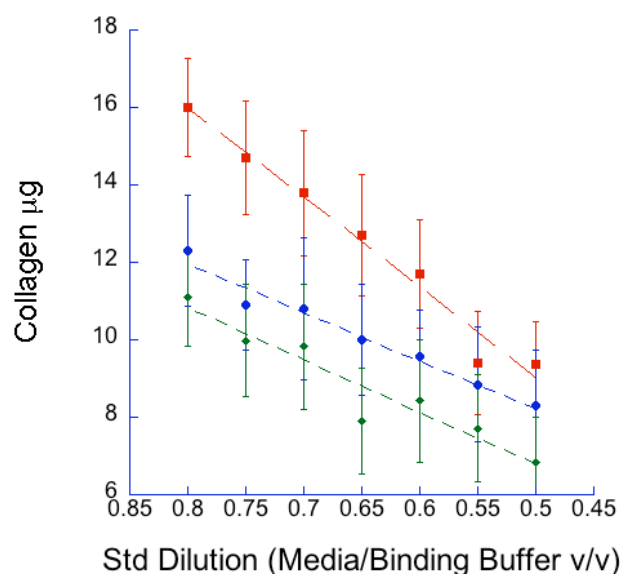


Figure 3.14. Inhibition of collagen with 0.2 mM phen-GKDEL (green diamonds), 0.2 mM phen (blue circles), and no inhibitor control (red boxes).

Assay of collagen in the ECM was performed by pepsin digest followed by indirect ELISA to determine collagen concentration. The IC_{50} value for phen was determined with inhibitor concentrations ranging from 0.01-1000 μ M. The IC_{50} value for phen-2-GKDEL was determined to be 250 μ M (Figure 3.16) that is very similar to the IC_{50} value of phen (160 μ M).

In both the soluble collagen secreted and collagen in the extracellular matrix showed similar inhibition of collagen production in HFF cells. This is in sharp contrast to the inhibition of P4H activity in which phen demonstrates 100 times more potency than phen-2-GKDEL

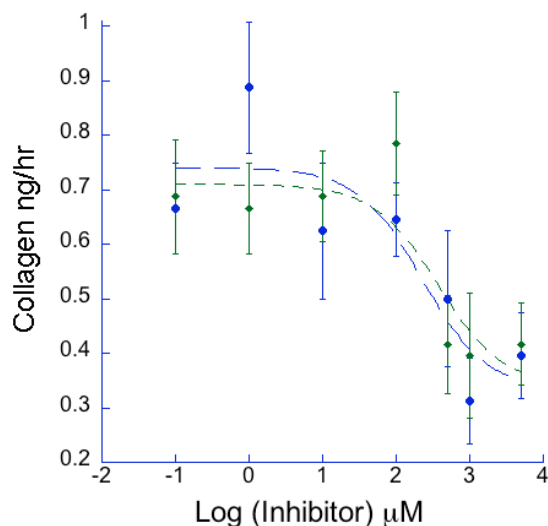


Figure 3.16. IC_{50} curve of phen (blue circles) and phen-GKDEL (green diamonds) with pepsin digested collagen.

3.4. Discussion

3.4.1. Synthesis of P4H Inhibitor Containing the Fe-chelator Coupled to an ER-Retention Signal Peptide as Potential *in vivo* Inhibitors

2-Carboxyl 1,10 phenanthroline was coupled with the KDEL tagged and designed to inhibit the production of collagen in the ER. The presence of amino acid peptide was confirmed by dispi 2-D NMR (Figure 3.16). The ability of phen derivatives to chelate to iron and inhibit production of collagen in P4H has already been reported.²⁵ The synthesis of the 2-carboxyl-phen is well established, but the novelty is the coupling of the KDEL retention tag. This will direct the iron chelation by phen to the ER for inhibition of P4H. As

there are other iron containing enzymes in the ER, addition of the sequence for peptide binding domain for P4H could be implemented to select for P4H. The sequence for the peptide binding domain is known and is specific for P4H.²² The synthesis of phen-5-GKDEL also has the potential to reduce the large IC₅₀ value observed in phen-2-GKDEL when tested with isolated enzyme. The steric interference of the KDEL tag next to the iron chelation could be reduced by moving it on the opposite side of the iron chelation. The phen-2-GKDEL synthesis was pursued due to the ease of synthesis of the 2-carboxy-phen. The synthesis of the 5-carboxy-phen is also reported^{59,60} and is currently undertaken in the lab.

3.4.2. Phen-2-VD(EDANS)KDEL Localizes in the ER of HFF Cells

Phen-2-E(EDANS)VKDEL was successfully synthesized, and addition of this agent with HFF cells demonstrated localization in the ER. Both have good co-localization (85%) as determined by Pearson's coefficient measured by the dependency of pixels in a linear expression of the intensities of two images on each other. The ER tracker demonstrated a more intense signal than the inhibitor. The weaker intensity could be in part due to the quick photobleaching of the phen-E(EDANS)VKDEL group observed when collecting data or coupling on to the receptor may have shifted the excitation/emission band. The subcellular co-localization analysis of both the fluorescently labelled inhibitor and the ER tracker indicate transport into the

ER. This reflects the ability of the inhibitor to reach and localize in the ER where P4H is known to reside.

3.4.3. Phen-2-GKDEL Demonstrates IC₅₀ value of 3.5 mM Against Isolated P4H Enzyme

The effect of phen-2-GKDEL inhibitor was tested against the recombinant P4H. The phen-2-GKDEL inhibitor exhibited an unexpected high IC₅₀ value (3.5 mM). This could potentially be caused by steric hindrance of the peptide chain at the C2 position on the phen next to the iron binding site. The steric interaction could possibly be avoided by moving the KDEL to the C5 position on the 1,10 phenanthroline ring and possibly lowering the IC₅₀ value to μ M range.

3.4.4. Phen-2-GKDEL Demonstrates IC₅₀ value of 250 μ M Inhibition in vitro with HFF Cells

Indirect ELISA was employed for the detection of collagen in the ECM. The IC₅₀ value for phen-2-GKDEL was prepared with inhibitor concentrations ranging from 0.01-1000 μ M, with an IC₅₀ value of 250 μ M. The scattering of the plot points may be caused by many sample transfers during the assay. Isolation of collagen underwent many steps, in which each step had the potential for losing some sample. The scattering of the plot points could be minimized by assay of procollagen, RIA, or the extraction of cellular proteins.^{23,25}

3.4.5. Phen is 100 Times More Potent than Phen-2-GKDEL in Isolated P4H Enzyme

Both phen and phen-2-GKDEL were tested with isolated P4H enzyme, in which phen demonstrated a 100 fold potency than phen-2-GKDEL. The reasoning behind the large difference in IC_{50} value could be attributed to the addition of the GKDEL signal peptide to phen. The signal peptide might sterically hinder the chelating capacity of phen. Future experiments are in progress to synthesize the phen with a reactive coupling carboxyl group at the C5 position away from the iron chelator motif (Figure 3.17). The signal peptide will have an advantage at the five position, as it will interfere less with iron chelation and could possibly interact with Lys493 and His501 of human P4H known to bind to the C-5 and C-1 carbonyls of α -ketoglutarate.

3.4.6. Collagen Inhibition by Phen-2-GKDEL and Phen Demonstrate Similar IC_{50} values in cultured HFF Cells

Phen and phen-2-GKDEL were also tested in vitro for inhibiting collagen production in HFF cells. The indirect ELISA results suggest that both phen and phen-2-GKDEL inhibit collagen production with the similar dose dependence manner. The IC_{50} values for both inhibitors are determined to be in the range of 10 - 50 μ M. For phen, this value is very similar to the IC_{50} value obtained with the isolated enzyme. However, phen-2-GKDEL demonstrates a 100-fold increase in potency in cultured HFF cells as compared with isolated enzyme. These results show that having the KDEL

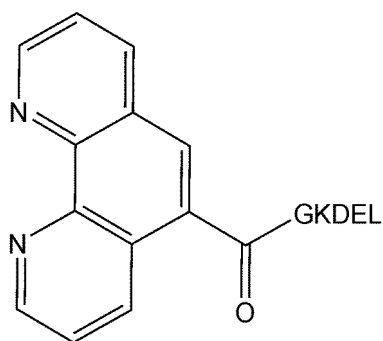


Figure 3.17. phen-5-GKDEL inhibitor, with the phenanthroline couple to the N terminus at the 5 position

retention tag is 100-fold effective than phen itself to support the idea of targeting P4H in the ER. The IC_{50} value for inhibiting the collagen production in the ECM was also similar between phen and phen-2-GKDEL. This demonstrates the inhibition of the collagen production in the ECM by both phen and phen-2-GKDEL and correlates with the results for the soluble collagen extracted in the media.

5. Conclusion

The use of signal peptide for drug delivery is a powerful tool that is quickly gaining interest. Phen-2-GKDEL discussed here is designed to specifically target P4H in the ER to inhibit collagen production. Fluorescence detection of the EDANS group coupled to the signal peptide demonstrates the localization of the phen-E(EDANS)VKDEL into the ER within 20 min. Detection with antibodies raised against collagen demonstrates the inhibition of collagen production in cultured HFF cells by phen-2-GKDEL. Phen was

also tested with phen-2-GKDEL as a positive control against isolated P4H and in vitro studies. Both have similar IC_{50} values in HFF cells. The difference in the two inhibitors was observed against isolated P4H. Phen-2-GKDEL had a 100-fold increase in the observed IC_{50} value as compared to phen. The data suggest the peptide signal at the 2 position of phen is interfering with iron chelation.

The GKDEL signal peptide could have a significant effect on the IC_{50} value in vitro and in vivo of phen derivatives if the observed IC_{50} value of phen-2-GKDEL decrease by 100-fold from isolated enzyme to HFF cells. To conclusively prove the effects of the signal peptide on decreasing the IC_{50} , more derivatives with the KDEL tag need to be synthesized. Currently, a new inhibitor where the KDEL tag at the 5 position of phen to avoid steric effects are undertaken. Other inhibitors are also being synthesized to target both the peptide binding domain as well as the iron active site.

References:

- (1) *Fibrosis*; Pitman: London, 1985.
- (2) Gunzler, E. H. a. V. *J. Hepatol.* **1991**, 13 (Supl 13), S1.
- (3) Pinheiro, G. A.; Antao, V. C.; Wood, J. M.; Wassell, J. T. *Int J Occup Environ Health* **2008**, 14, 117-123.
- (4) *Tenth special report to the U.S. Congress on alcohol and health. Highlights from current research: From the Secretary of Health and Human Services*, 2000.
- (5) Majithia, V.; Geraci Stephen, A. *Am. J. Med.* **2007**, 120, 936-9.
- (6) Strieter, R. M. *Proceedings of the American Thoracic Society* **2008**, 5, 305-310.
- (7) Anthony, P. P.; Ishak, K. G.; Nayak, N. C.; Poulsen, H. E.; Scheuer, P. J.; Sobin, L. H. *J. Clin. Pathol.* **1978**, 31, 395-414.
- (8) Friedman, S. L. *N. Engl. J. Med.* **1993**, 328, 1828-35.
- (9) Sporn, M. B.; Harris, E. D., Jr. *Am. J. Med.* **1981**, 70, 1231-6.
- (10) Kovacs, E. J. *Immunol. Today* **1991**, 12, 17-23.
- (11) Franklin, T. J. *Biochem. Pharmacol.* **1995**, 49, 267-73.
- (12) Crystal, R. G.; Bitterman, P. B.; Rennard, S. I.; Hance, A. J.; Keogh, B. A. *N. Engl. J. Med.* **1984**, 310, 235-44.
- (13) Border, W. A.; Noble, N. A. *Am. J. Kidney Dis.* **1993**, 22, 105-13.
- (14) Roberts, A. B.; Sporn, M. B.; Assoian, R. K.; Smith, J. M.; Roche, N. S.; Wakefield, L. M.; Heine, U. I.; Liotta, L. A.; Falanga, V.; et al. *Proc. Natl. Acad. Sci. USA* **1986**, 83, 4167-71.
- (15) Shah, M.; Foreman, D. M.; Ferguson, M. W. *Lancet* **1992**, 339, 213-4.
- (16) Segarini, P. R. *Biochim. Biophys. Acta* **1993**, 1155, 269-75.
- (17) Levitzki, A. *FASEB Journal* **1992**, 6, 3275-82.
- (18) Myllyharju, J. *Matrix Biology* **2003**, 22, 15-24.
- (19) Guzman, N. A.; Editor *Prolyl Hydroxylase, Protein Disulfide Isomerase, and Other Structurally Related Proteins*, 1998.
- (20) Hanauske-Abel, H. M. G., V. *J. Theor. Biol.* **1982**, 94, 421-455.
- (21) Lamberg, A.; Pihlajaniemi, T.; Kivirikko, K. I. *Journal of Biological Chemistry* **1995**, 270, 9926-31.
- (22) Myllyharju, J.; Kivirikko, K. I. *EMBO Journal* **1999**, 18, 306-312.
- (23) Franklin, T. J.; Hales, N. J.; Johnstone, D.; Morris, W. B.; Cunliffe, C. J.; Millest, A. J.; Hill, G. B. *Biochemical Society Transactions* **1991**, 19, 812-15.
- (24) Dowell, R. I.; Hadley, E. M. *J. Med. Chem.* **1992**, 35, 800-4.
- (25) Franklin, T. J.; Morris, W. P.; Edwards, P. N.; Large, M. S.; Stephenson, R. *Biochemical Journal* **2001**, 353, 333-338.

- (26) Pelham, H. R. B.; Hardwick, K. G.; Lewis, M. J. *EMBO Journal* **1988**, *7*, 1757-62.
- (27) Pelham, H. R. B. *EMBO Journal* **1988**, *7*, 913-18.
- (28) Lee, M. C. S.; Miller, E. A.; Goldberg, J.; Orci, L.; Schekman, R. *Annual Review of Cell and Developmental Biology* **2004**, *20*, 87-123.
- (29) Yamamoto, K.; Fujii, R.; Toyofuku, Y.; Saito, T.; Koseki, H.; Hsu, V. W.; Aoe, T. *EMBO Journal* **2001**, *20*, 3082-3091.
- (30) Scheel, A. A.; Pelham, H. R. B. *Journal of Biological Chemistry* **1998**, *273*, 2467-2472.
- (31) Scheel, A. A.; Pelham, H. R. *Biochemistry* **1996**, *35*, 10203-9.
- (32) Wilson, D. W.; Lewis, M. J.; Pelham, H. R. B. *Journal of Biological Chemistry* **1993**, *268*, 7465-8.
- (33) Pap, E. H. W.; Dansen, T. B.; van Summeren, R.; Wirtz, K. W. *A. Exp. Cell Res.* **2001**, *265*, 288-293.
- (34) Gasiorowski, J. Z.; Dean, D. A. *Adv. Drug. Deliv. Rev.* **2003**, *55*, 703-716.
- (35) Lanford, R. E.; Butel, J. S. *Cell* **1984**, *37*, 801-13.
- (36) Kalderon, D.; Richardson, W. D.; Markham, A. F.; Smith, A. E. *Nature* **1984**, *311*, 33-8.
- (37) Dubrovsky, L.; Ulrich, P.; Nuovo, G. J.; Manogue, K. R.; Cerami, A.; Bukrinsky, M. *Mol. Med.* **1995**, *1*, 217-30.
- (38) Haffar, O. K.; Smithgall, M. D.; Popov, S.; Ulrich, P.; Bruce, A. G.; Nadler, S. G.; Cerami, A.; Bukrinsky, M. I. *Antimicrobial Agents and Chemotherapy* **1998**, *42*, 1133-1138.
- (39) Popov, S.; Dubrovsky, L.; Lee, M.-A.; Pennathur, S.; Haffar, O.; Al-Abed, Y.; Tonge, P.; Ulrich, P.; Rexach, M.; et al. *Proc. Natl Acad. Sci. USA* **1996**, *93*, 11859-11864.
- (40) Kestler, H.; Kodama, T.; Ringler, D.; Marthas, M.; Pedersen, N.; Lackner, A.; Regier, D.; Sehgal, P.; Daniel, M.; King, N. *Science* **1990**, *248*, 1109-12.
- (41) Coppola, J. M.; Hamilton, C. A.; Bhojani, M. S.; Larsen, M. J.; Ross, B. D.; Rehemtulla, A. *Analytical Biochemistry* **2007**, *364*, 19-29.
- (42) Neurath, H.; Walsh, K. A. *Proc. Natl. Acad. Sci. USA* **1976**, *73*, 3825-32.
- (43) Halban, P. A.; Irminger, J. C. *Biochemical Journal* **1994**, *299*, 1-18.
- (44) Vassar, R. *Adv. Drug Deliv. Rev.* **2002**, *54*, 1589-1602.
- (45) Capecchi, M. R. *Cell* **1980**, *22*, 479-88.
- (46) Ludtke, J. J.; Zhang, G.; Sebestyen, M. G.; Wolff, J. A. *Journal of Cell Science* **1999**, *112*, 2033-2041.
- (47) Zanta, M. A.; Belguise-Valladier, P.; Behr, J.-P. *Proc. Natl. Acad. Sci. USA* **1999**, *96*, 91-96.

- (48) Sun, W.-H.; Jie, S.; Zhang, S.; Zhang, W.; Song, Y.; Ma, H.; Chen, J.; Wedeking, K.; Froehlich, R. *Organometallics* **2006**, 25, 666-677.
- (49) Shen, Y.; Sullivan, B. P. *Inorganic Chemistry* **1995**, 34, 6235-6.
- (50) Higgins, B.; DeGraff, B. A.; Demas, J. N. *Inorganic Chemistry* **2005**, 44, 6662-6669.
- (51) Rasband, W. S., ImageJ, U. S. National Institutes of Health, Bethesda, ; Maryland, U., <http://rsb.info.nih.gov/ij/>, 1997-2007.
- (52) Bolte, S.; Cordelieres, F. P. *Journal of Microscopy* **2006**, 224, 213-232.
- (53) Lindberg, U., Schutt, C.E., Hellsten, E., Tjäder, A., and Hult T. *Biochimi. Biophys. Acta* **1988**, 967, 391-400.
- (54) P. K. Smith, R. I. K., G. T. Hermanson, A. K. Mallia, F. H. Gartner, M. D. Provenzano, E. K. Fujimoto, N. M. Goeke, B. J. Olson and D. C. Klenk. *Analytical Biochemistry* **1985**, 150, 76-85.
- (55) Lui, B., Li, S., Hu, J., *Am. J. Pharmacogenomics* **2004**, 4, 263-276.
- (56) ED Matayoshi, G. W., GA Krafft, and J Erickson *Science* **1990**, 247, 954-958.
- (57) Zunkler, B., Wos-Maganga, M., Panten, U., *Biochem Pharmacol* **2004**, 67, 1437-1444.
- (58) Matayoshi, E., Wang, G., Krafft, G., Erickson, J., *Science* **1990**, 247, 954-958.

Chapter 4

Photolytic Release of Nitric Oxide from an Immobilized Ruthenium Complex

4.1. Background

In the 1980's, nitric oxide (NO) was found to cause vascular smooth muscle relaxation by the activation of cGMP.¹ Since then, NO has been established as a critical mediator in various bioregulatory processes of the cardiovascular, nervous, genitourinary, immune, and gastrointestinal systems.^{1,2} Several diseases are related directly to over or underproduction of NO, creating great interest in the design and development of NO donors for NO delivery.³⁻⁵ These NO donors have potential for the treatment of heart attacks, thrombosis, cancer, and restenosis.

4.1.1. Nitric Oxide

NO is a colorless gas with one unpaired electron, which causes it to be highly reactive with other species within the body.¹ Nitric oxide synthase (NOS) is responsible for the production of nitric oxide within the body. This dimeric enzyme contains both flavin adenine dinucleotide and flavin mononucleotide cofactors. In a five electron process containing both oxidation and reduction cycles, L-Arginine is converted to citrulline, producing one equivalent of NO. The enzymes location and effect on the body distinguish the three isoforms of NOS; they include neuronal (nNOS),

inducible (iNOS), and endothelial (eNOS).^{1,2} Neuronal NOS is located in nervous system and is involved in cell communication.⁶ Inducible NOS fights pathogenic infections in the immune and cardiovascular systems.¹ Endothelial NOS is found in the endothelial layer of blood vessels and produces NO that causes vasodilatation of smooth muscles. As these examples illustrate, NO is ubiquitous throughout the body, causing the need to develop synthetic systems to deliver NO. Because of the diversity of NO function, it is now recognized that a variety of systems are necessary.³

4.1.2. Current NO Donors in Medical Practices

Several NO donors are currently employed in the medical practice, but complications can arise from toxic byproducts or to tolerance to the drug.^{1,2,4} Nitrate esters, such as nitroglycerin, that release NO are known to relax blood vessels and relieve chest pain due to angina (Figure 4.1a). Three electron

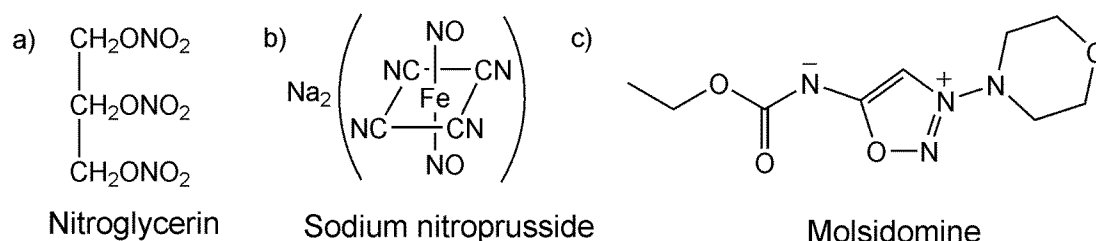


Figure 4.1. NO donors drugs approved for medical use a) Nitroglycerin - relief of angina and chronic heart failure. b) Sodium nitroprusside - lowering of blood pressure during hypertensive emergency. c) Molsidomine - treatment of hypertension.

reduction of nitrate ester generates NO, causing vasodilatation. Doctors have found, though, that a patient's body can develop a tolerance to nitroglycerin and may require increasingly high dosages to elicit the same response.⁷ Sodium nitroprusside (SNP) is another NO donor that rapidly lowers blood pressure (Figure 4.1b). SNP is administered during surgery when blood pressure is fluctuating dangerously; however the byproducts of SNP are problematic.⁸ Both free cyanide ion and iron center are generated during the one-electron reduction of SNP. Molsidomine is used in Europe for the treatment of hypertension (Figure 4.1c). Through ring opening metabolism, Molsidomine releases one equivalent of NO along with peroxynitrite, which is a highly toxic nitrogen species.⁹ All of these NO donors are currently used in the medical field, but harmful byproducts or dose-related tolerance have prompted the design of safer and more reliable NO donors for medical treatments.

4.1.3. Controlled Release of NO by Diazeniumdiolates

The leading research on NO drug delivery has been the design of diazeniumdiolates (NONOates), pioneered by Keefer and co-workers at the National Cancer Institutes Laboratory of Comparative Carcinogenesis.^{3-5,10} NONOates are a possible treatment for medical disorders caused by NO deprivation as they provide controlled delivery of NO without harmful byproducts. NONOates have a chemical formulation of $R^1R^2NN(O)=NOR^3$ and can be designed to target and control the release of NO (Figure 4.2).

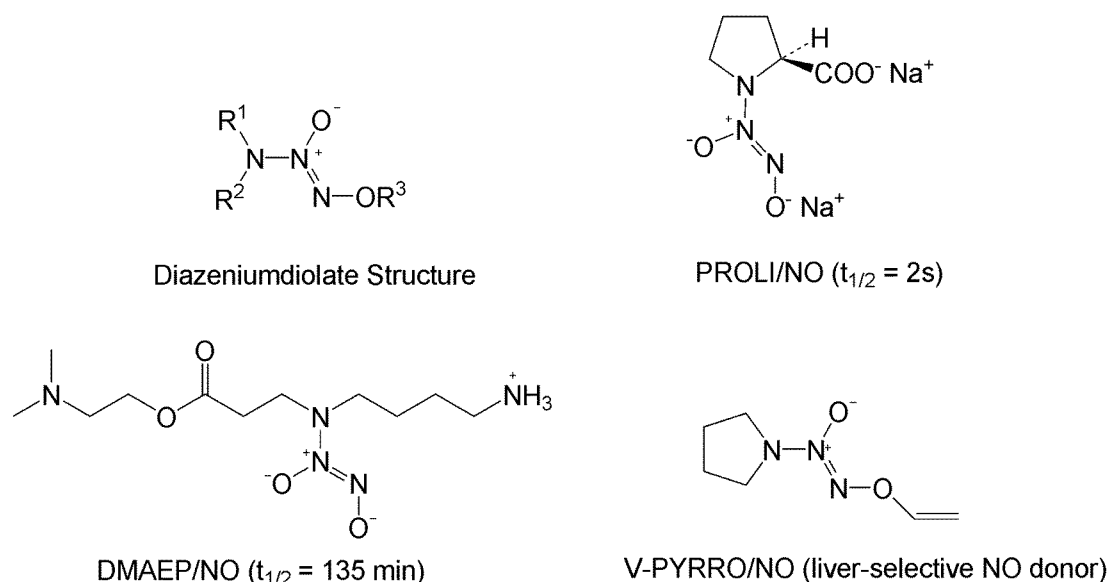


Figure 4.2. Structures and time release of selective diazeniumdiolates

These prodrugs control the release of nitric oxide based on their structure. The three R groups can be modified to control the location of delivery and rate of release. R^1 and modifications of R^2 are usually associated with control the release rate of NO, while R^3 serves as a site to bind a cation. For instance, when R^1 and R^2 were modified to the amino acid L-proline, the initial reaction under basic condition yielded PROLI/NO. PROLI/NO is stable under basic conditions, but at physiological pH has a half-life of 1.8 s, converting to L-proline and two equivalents of NO with a half-life of 1.8s. PROLI/NO has been shown to reduce platelet aggregation in baboon's blood.¹¹ When infused into the right atrium of sheep, PROLI/NO proved to reduce the pulmonary arterial pressure. When R^1 and R^2 are changed from proline to

longer alkyl chains, longer half lives are generally observed. One example of a NONOate with a longer time release is DMAEP/NO, which has an observed half-life of 135 min.¹² The above examples involve R³ site ionically bound as a cation; however, when R³ is covalently linked to the NONOate release of NO is inhibited until the R³ group is cleaved off. Covalent linkers to the R³ group are specific to certain enzymes and could potentially control both the release of NO as well as the desired location. For example, the NO group of V-PYRRO/NO is specifically cleaved by cytochrome p450 and delivers NO to the liver.¹³

Further modifications made for NO release comes from various polymer support biomaterials that could potentially release NO from site-specific locations and avoid the release of harmful byproducts into the body. NONOates have demonstrated the ability to release NO from a solid support. The need for a material that releases NO has been made evident by restenosis after angioplasty. The buildup of atheromatous plaque in the coronary artery can restrict blood flow, leading to heart attack and possibly death. A process known as angioplasty can clear the blocked artery and restore blood flow. In this process, a balloon is inflated at the site of plaque build up, expanding the artery to allow blood flow. Complications include overstretching the artery, leading to an overproduction of vascular smooth muscle cells and the thickening of the vessel wall. Stents may be employed to prevent the re-constriction of the blood vessels, but buildup of smooth

muscles is still observed. Kaul and coworkers designed a NO releasing gel containing the NONOate SPER/NO to be placed at the site of restenosis; this would inhibit smooth muscle accumulation and further thickening of the vessel wall.¹⁴ When treated with the SPER/NO gels, the damaged artery had similar appearance to normal and healthy arteries while the untreated artery still appeared injured and damaged with the build up of smooth muscle.

Addition of foreign objects to the body causes excessive platelet aggregation.¹⁵ NO is known to inhibit platelet aggregation. Smith and coworkers demonstrated that objects implanted into the body that have been coated with NONOate releasing material inhibit platelet aggregation.¹⁶ Biosensors coated with NONOates have improved accuracy due to the inhibition of platelet aggregation. Blood oxygen sensing measurements were taken with electrode with and without NONOate releasing material.¹⁷ The accuracy of the sensor coated with NONOate was very close to standard clinical chemistry methods while the non-coated sensor had diminished readings. Materials with the ability to release NO at site specific locations have proven useful in angioplasty procedures as well as in their ability to inhibit platelet aggregation with reduced complications towards the biosensor.

4.1.4. Ruthenium Salen Nitrosyl Complex Release of Nitric Oxide

Another approach to NO delivery to site specific a location is the photochemical release of NO. The photorelease of NO from metal- N,N'-ethylenebis(salicylideneimine) (salen) complex could be applied to treating

thrombosis as seen previously. In addition site, delivery of NO could potentially be an effective mediator of cytotoxic action of macrophages toward tumor cells.^{18,19} The synthesis and characteristics of light activated ruthenium salen nitrosyl complex (Ru(salen)(Cl)(NO)) have been described recently by Ford and co-workers (Figure 4.3).²⁰ These complexes are thermally stable but photochemically release NO. Spectroscopic analysis of the Ru(salen)(Cl)(NO) displayed a strong ligand-localized $\pi-\pi^*$ UV absorbance band at 376 nm. The FTIR spectrum shows the nitrosyl stretching frequency at 1844 cm^{-1} . The photochemistry of Ru(salen)(Cl)(NO) was monitored by the spectral changes that occur when an acetonitrile solution of the complex was irradiated at $\lambda_{\text{irr}} = 365\text{ nm}$. Photolysis leads to the increased absorbance at 348 nm, and new bands were displayed at $\lambda = 494$ and 724 nm. Isosbestic points were also seen at $\lambda_i = 313, 392,$ and 448 nm . The absorbance at $\lambda = 724\text{ nm}$ was assigned as a ligand (phen) to metal (Ru^{III}) charge transfer band. Disappearance of FTIR ν_{NO} band at 1844 cm^{-1} was also observed upon

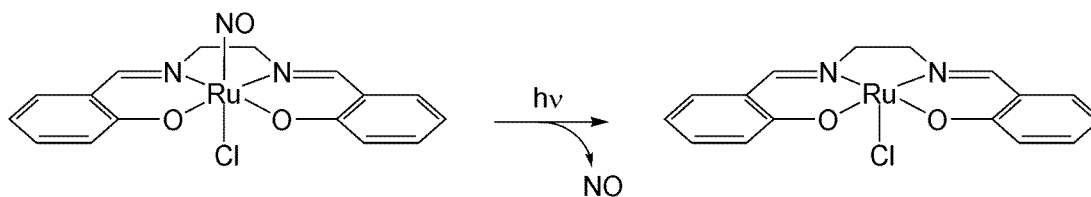


Figure 4.3. Photochemical release of NO from ruthenium salen complex

photolysis of the complex at $\lambda_{\text{irr}} = 365 \text{ nm}$. When photolysis was carried out in aerated solutions, the observed spectral changes were permanent; however, in deaerated solutions, the spectral characteristic went back to those of the starting complex due to the absence of O_2 unable to react with NO. In nonpolar, deaerated solutions, the $\text{Ru}(\text{salen})(\text{Cl})(\text{NO})$ complex displayed no spectral changes as the rate towards reformation of starting complexes was solvent dependent, since solvent coordinates to the axial position after NO leaves. Quantum yield for this complex was determined based on spectral changes and calculated product extinction coefficients: $\Phi_{\text{NO}} = 0.13$ at $\lambda_{\text{irr}} = 365 \text{ nm}$, $\Phi_{\text{NO}} = 0.09$ at $\lambda_{\text{irr}} = 436 \text{ nm}$, $\Phi_{\text{NO}} = 0.07$ at $\lambda_{\text{irr}} = 546 \text{ nm}$. The photoefficiency decreases at longer wavelengths but still continues to release NO. A low barrier for NO dissociation could explain this observed. It was anticipated that modification to the salen ligand would make it possible to covalently link a Ru-NO complex to a polymeric support for the controlled release of NO.

4.1.5. Immobilized Metal Salen Complexes for the Storage and Release of NO

Borovik and co-workers have developed methods for the immobilization of metal salen complexes into polymer material.²¹⁻²³ In their template copolymerization with metal complexes, the metal complex is substitutionally inert to ensure that the various ligands remain coordinated. These ligands contain a polymerizable vinyl group that will ultimately be

covalently link into a polymer host. The schematic representation of this process is seen in Figure 4.4. The use of template copolymerization for the storage and release of NO was first demonstrated by Padden and

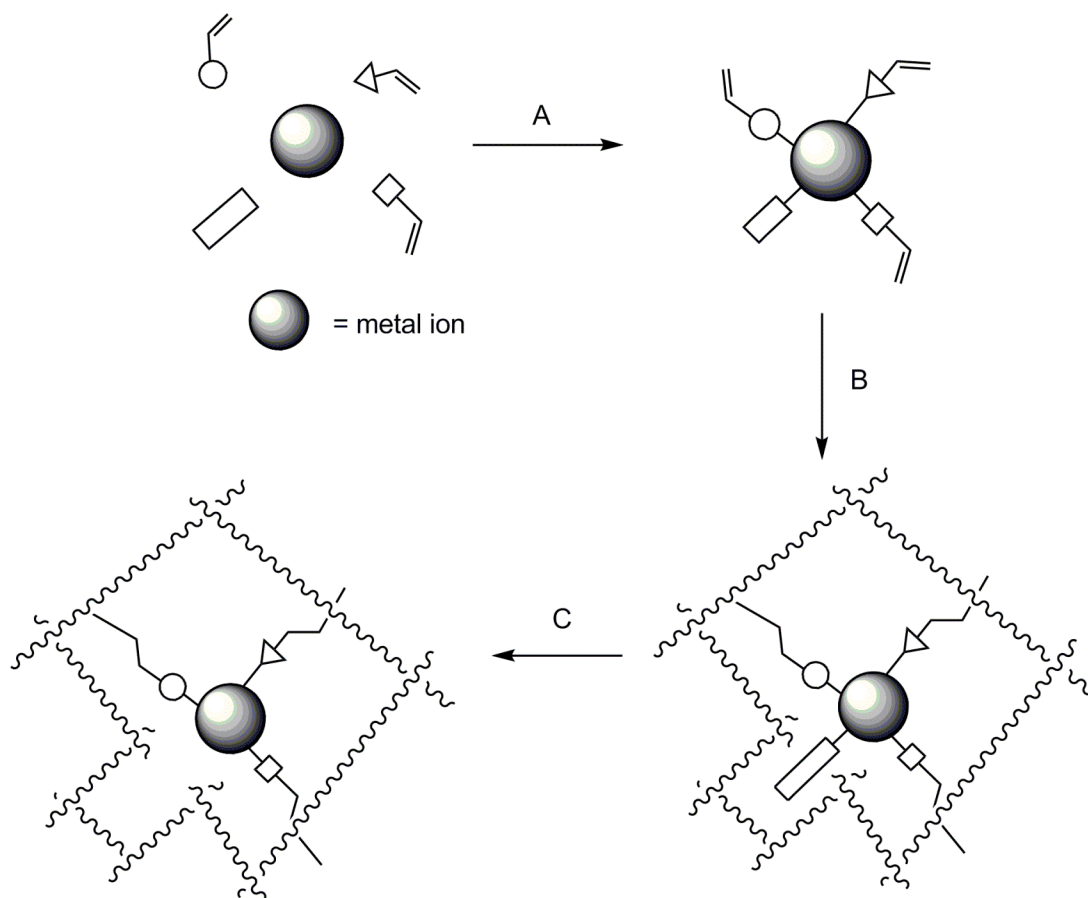


Figure 4.4. In the process of template copolymerization, A) the metal ions are stabilized by ligands for a substitutionally inert complex. B) Crosslinking agents react with the vinyl groups and polymerize the metal complex. C) Ligands without vinyl groups are removed to provide space for reactivity.

co-workers.²¹ This process involved the polymerization of a Co^{II} salen complex into porous solids, having site-isolated cavities with channels that connect the cavities to the polymer surface. This is a bio-inspired design, in which site-isolation and channel structures are common structural features in metalloproteins.²⁴⁻²⁶ In order to construct the desired environment around the metal center, the metal complexes were prepared before insertion into the organic polymer. A styrene-modified salen ligand allows covalent-incorporation of polymerizable functional groups of the ligand into the organic host. This material was one of few with the ability to bind and release NO (Figure 4.5). Upon binding of NO, P-1[Co^{II}] changes from an orange color to a brown-green color characteristic of P-1[Co(NO)]. The release of NO and conversion to the unbound orange polymer P-1[Co^{II}] form was accomplished in approximately one hour upon heating and under vacuum. Reversible binding of NO was observed through EPR spectroscopy. Solid P-1[Co^{II}] exhibits an axial spectrum signal at $g = 3.83$ and $g = 1.98$, which is

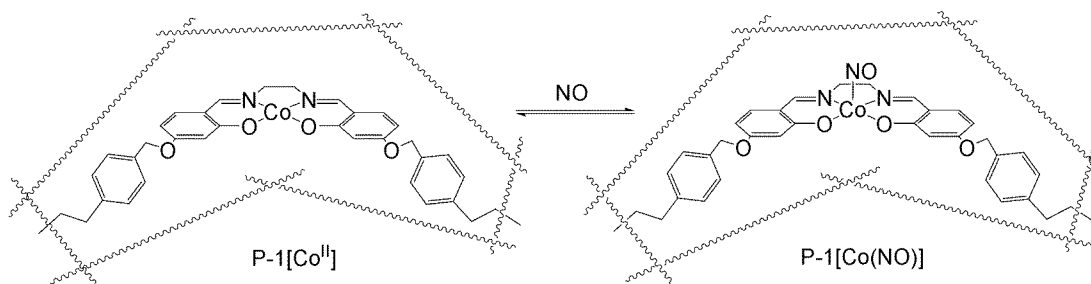


Figure 4.5. The storage and release of NO from P-1[Co^{II}].

characteristic of a Co^{II} square planar geometry. Binding of NO to $\text{P-1}[\text{Co}^{\text{II}}]$ quenches the EPR signal as a result of antiferromagnetic coupling of the Co^{II} center and the unpaired electron of the NO. The signal for $\text{P-1}[\text{Co}^{\text{II}}]$ was observed when $\text{P-1}[\text{Co}(\text{NO})]$ was placed under vacuum; however, the signal was again disappeared when additional NO was added to the system. Slow, passive release of NO was also observed under conditions of ambient temperature and pressure: 40% of the NO was release after 14 days. The $\text{P-1}[\text{Co}(\text{NO})]$ demonstrates the possibility of NO release from a porous polymer support.

The controlled release of NO through photolysis can potentially be applied by immobilizing ruthenium nitrosyl (Ru-NO) complexes within a similar material as used with $\text{P-1}[\text{Co}(\text{NO})]$. This chapter describes the synthesis and controlled release study of NO from a polymer support using a Ru-NO complex. Providing polymerizable vinyl groups to salen $\text{Ru}(\text{NO})$ complex allowed for covalent linkage to the solid support.^{20,27} The release of NO is triggered by light, which allows the controlled transfer of NO from the polymer to biologically relevant compounds. This material illustrates the controlled release of NO without the formation of toxic and unwanted byproducts. The potential medical applications of this system maybe treatment of angina pectoris, myocardial infarction, congestive heart failure, and treatment for different cancers.

4.2. Materials and Methods

Unless otherwise stated, all materials and solvents were obtained from Aldrich (Milwaukee, WI) or Fisher (Pittsburgh, PA). All inert conditions were performed with either Vacuum Atmospheres (Hawthorne, CA) drybox under or a Schlenk-line under argon atmospheres.

4.2.1. Synthesis of Bis[2-hydroxy-4-(4-

vinylbenzyloxy)benzaldehyde]ethylenediimine. (H₂1) Synthesis was performed as described by Borovik and co workers.²⁸ 2-Hydroxy-4-(4-vinylbenzyloxy)benzaldehyde (2.00 g, 7.86 mmol), was suspended in 100 mL of dry methanol and placed under an argon atmosphere. Ethylenediamine (0.24 g, 3.90 mmol, 0.16 ml) was added with a syringe and the resulting yellow solution was stirred for 4 hours, during which time a yellow precipitated formed. The yellow product was isolated by suction filtration with a fritted-glass filter and washed with 30 mL of chloroform to yield 1.83 g of product (88% yield). ¹H NMR (CDCl₃): δ 3.86 (s, 4H), 5.05 (s, 4H), 5.26 (d, 2H), 5.75 (d, 2H), 6.46 (dd, 2H), 6.51 (d, 2H), 6.70 (dd, 2H), 7.08 (d, 2H), 7.11 (d, 2H), 7.41 (m, 4H), 8.21 (s, 2H), 13.62 (s, 2H).

4.2.2. Ru(NO)Cl₃ Ru(NO)Cl₃ was synthesized following published procedures.^{29,30} RuCl₃ x H₂O (0.450 g, 2.17 mmol) was dissolved in 25 mL of 1 M HCl and the solution was degassed with N₂ for 15 min. As the solution was refluxing at 100°C, an aqueous solution (10 mL) of NaNO₂ (0.452 g, 2.17 mmol) was added dropwise by addition funnel and allowed to reflux for 3 h. At the completion of the reaction, solvent was removed under reduced

pressure. The resulting red compound was then washed in 5 mL of 100% ethanol, 5 mL of 6 M HCl, and then washed three times with 3-5 mL aliquots of H₂O, removing solvent after each addition. The reddish product was then dried under reduced pressure to yield 0.536 g (91%). FTIR (nujol, cm⁻¹) 1897 (ν NO).

4.2.3. Ru1(NO)(Cl) Synthesis of ruthenium complexes followed the procedure published by Ford and coworkers.³⁰ Under inert atmosphere, a 30 mL DMF solution of H₂1 (0.250 g, 0.468 mmol) in DMF was treated with 2 equiv of solid KH (0.0375 g, 0.936 mmol). After gas release (H₂) was completed (~30 min) Ru(NO)Cl₃ (0.113 g, 0.479 mmol) was added and the mixture was refluxed for 2 h. Solvent was removed by rotoevaporation to give a brown solid, which was purified using silica gel flash chromatography with a mobile phase of 2% methanol/98% methylene chloride. Fractions containing the desired Ru1(NO)(Cl) complex were collected and solvent was removed under reduced pressure to yield 0.24 g of brown solid (45%). ¹H NMR (CDCl₃): δ 3.92 (d, 2H), 4.30 (d, 2H), 5.07 (s, 4H), 5.28 (d, 2H), 5.30 (d, 2H), 5.77 (d, 2H), 6.40 (d, 2H), 6.73 (m, 2H), 6.88 (s, 2H), 7.15 (d, 2H), 7.42 (dd, 8H), 8.11 (s, 2H).

4.2.4. P-1[Ru(NO)(Cl)] Under an argon atmosphere, Ru1(NO)(Cl) (0.100 g, 0.144 mmol, 5 mol %), ethylene glycol dimethacrylate (EGDMA) (0.53 g, 2.7 mmol, 94 mol %), and azodiisobutyronitril (AIBN) (5 mg, 0.03 mmol, 1 mol %) were added to a thick-wall polymerization tube (Ace Glass). Porogen DCB

(1.5 g) was added and the tube was sealed and wrapped in foil to prevent the release of NO. The solution was heated at 60 °C for 24 h, after which the polymer underwent continuous extraction, using a Soxhlet extractor, with CH₂Cl₂ for another 24 h. The polymer was dried under reduced pressure to yield 0.642 grams of product. The polymer was crushed and separated with particle size smaller than 75 μm and between 0.5 and 1.0 mm with molecular sieves.

4.2.5. NO Release Studies Particles of P-1[Ru(NO)(Cl)] (20mg) were suspended with 2 mL of phosphate buffer solution (50 mM, pH 7.2) in Pyrex test tubes. Samples were covered with parafilm and stored in the dark in a Rayonet photochemical reactor. During five minutes intervals, the samples were irradiated with light at $\lambda_{\text{irr}} = 350 \text{ nm}$ (~24 W) and then a 50 μL sample was removed and added to 96-well microtiter plate. NO was detected by nitrite concentration in water using the Griess reagent system (Promega), and colorimetric absorbance at $\lambda = 520 \text{ nm}$ was determined with a SpectraMax 190 plate reader.^{31,32}

4.2.6. NO Transfer Studies A solution of 100 mg of metmyoglobin (metMb) and known concentration of P-1[Ru(NO)(Cl)], in a typical experiment, was prepared in a 1.00 cm Suprasil quartz cuvette and sealed under an inert atmosphere with a rubber septum. Reduction of equine skeletal muscle metMb was performed with 1.2 equiv of dithionite to obtain the reduced form of myoglobin (Mb). The sample was irradiated with a Hg arc lamp, equipped

with a $\lambda_{\text{irr}} = 370$ nm wavelength bandpass filter (Omega Optical). Spectra were collected on a Varian Cary 50 spectrophotometer at room temperature.

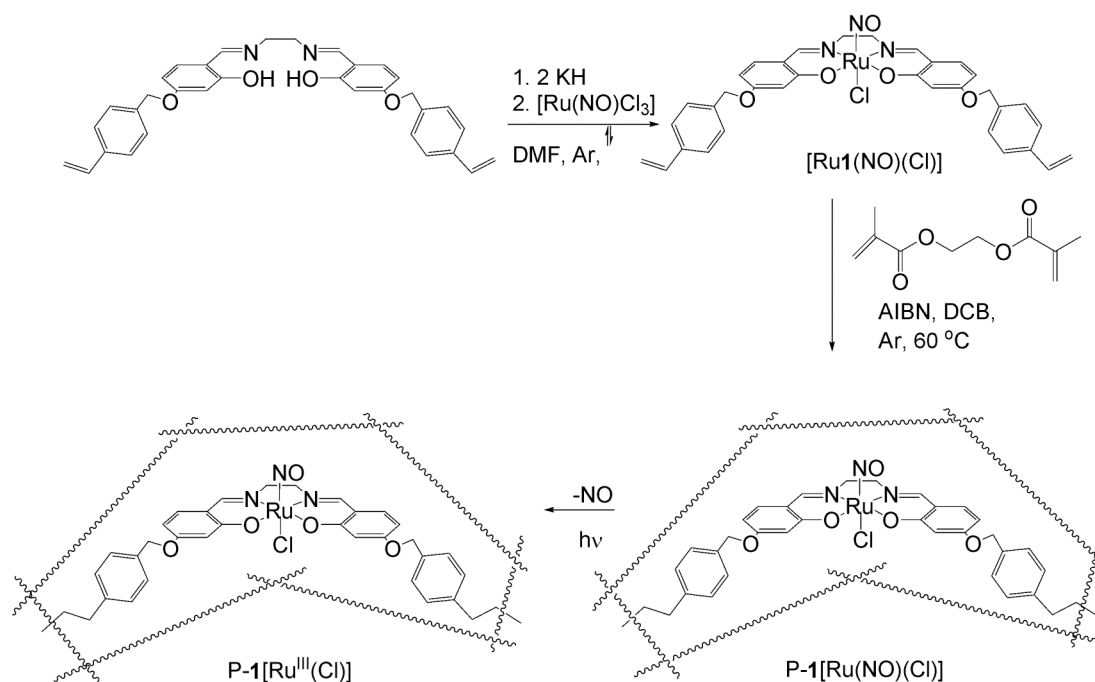
4.2.7. Physical Methods Proton nuclear magnetic resonance spectra were collected on a 400 MHz Bruker spectrometer. UV/Visible spectra of all samples were collected on a Varian Cary 50 spectrophotometer. Fourier transform infrared spectra were collected on a Mattson Genesis Series FT-IR spectrometer. Time release studies with the Griess reaction were performed on SpectraMax 190 96-well plate reader. EPR spectra were collected on a Bruker EMX spectrometer.

4.3. Results and Discussion

4.3.1. Synthesis of Ru1(NO)(Cl) and P-1[Ru(NO)(Cl)] Ru1(NO)(Cl) was obtained in 45% yield and characterized with UV/vis, FT-IR and EPR spectroscopies and compared to literature values.³⁰ The absorbance spectrum showed a band at $\lambda = 367$ nm for the monomeric complex, which was assigned as a metal-to-ligand charge transfer (MLCT) band. The silent EPR spectrum was observed presumably due to antiferromagnetic coupling of the unpaired electron of the NO and unpaired electron of the low-spin d^5 Ru^{III} center.³³ The FT-IR stretching at 1830 cm^{-1} was assigned to the nitrosyl group.

The Ru(NO)(Cl)₃ monomer complex was stable under all the reaction conditions, including polymerization, as long as light exposure was avoided. The styryloxy groups provided polymerizable sites for immobilization within a

porous polymer. Scheme 4-1 illustrates the preparation of P-1[Ru(NO)Cl], including the monomer Ru1(NO)(Cl), EGDMA for the crosslinking agent, AIBN as the radical initiator and 1,2-dichlorobenzene as the porogen. The polymer was collected, dried, crushed and sieved to isolate the material as particle, ranging in size from smaller than 75 μM to 1 mM. Several spectroscopic analyses were performed to ensure P-1[Ru(NO)(Cl)] was undisturbed during the synthesis and compared to [Ru1(NO)(Cl)] monomer. EPR spectroscopy was silent at 77 K and 4 K due



Scheme 4.1. Synthesis of [Ru(1)(NO)(Cl)], P-1[Ru(1)(NO)(Cl)], and P-1[Ru(1)(Cl)]. AIBN = azobisisobutyronitrile, DCB = 1,2-dichlorobenzene

to the antiferromagnetic coupling between the unpaired electron of NO and the unpaired electron of the low-spin d^5 Ru^{III} complex. The FT-IR (KBr plates) stretching frequency spectrum of P-1[Ru(NO)(Cl)] exhibited a band at 1824 cm^{-1} that is characteristic of the NO stretching frequency. The UV/Vis spectrum of the polymer suspended in toluene reveals a λ_{max} of 373 nm. These spectroscopic features are in agreement with the [Ru1(NO)(Cl)] monomer.³³

4.3.2. Photorelease of Nitric Oxide from P-1[Ru(NO)(Cl)] Photolytic release of NO from [Ru1(NO)(Cl)] and P-1[Ru(NO)(Cl)] was performed by broad-band irradiation with a Hg arc lamp. Upon photolysis, P-1[Ru(NO)(Cl)] is converted to P-1[Ru^{III}(Cl)], a process that was observed spectroscopically. The EPR spectrum after photolysis of P-1[Ru(NO)(Cl)] showed a rhombic signal with g value at 2.3, 2.1, and 1.8, which is characteristic of immobilized ruthenium(III) complexes with $S = \frac{1}{2}$ ground state (Figure 4.6). The unpaired electron on the ruthenium that was antiferromagnetically coupled to radical NO is observed after the release of NO. P-1[Ru(NO)(Cl)] was suspended in CH_2Cl_2 and irradiated to obtain the electronic absorbance spectra revealing the peak absorbances at $\lambda_{\text{max}} = 400$ and 660 nm. Both of these values are characteristic of other monomeric Ru complexes after the release of NO.

4.3.3. NO Transfer to Metalloporphyrin Previous efforts by Koch and coworkers demonstrated the transfer of NO from P-1[Ru(NO)(Cl)] to cobalt(II) tetraphenylporphyrin ([Co^{II}(TPP)]).³³ Irradiation of the suspended polymer

and $[\text{Co}^{\text{II}}(\text{TPP})]$ at 370 nm demonstrated the transfer of NO from the polymer to the metalloporphyrin. NO transfer appears to occur cleanly as shown by the sharp isosbestic points at $\lambda_{\text{max}} = 397, 420$ and 425 nm for the conversion of $[\text{Co}^{\text{II}}(\text{TPP})]$ to $[\text{Co}^{\text{II}}(\text{TPP})(\text{NO})]$. Moreover, the transfer was complete in less than 20 minutes. Transfer of NO to a biological metalloporphyrin were performed with myoglobin (Mb), which has been shown to bind NO.³⁴ Mb has also been known to act as a NO scavenger, and has a high concentration in cardiac cells and muscles.³⁵ In a typical in vitro experiment, $\text{P-1}[\text{Ru}(\text{NO})(\text{Cl})]$

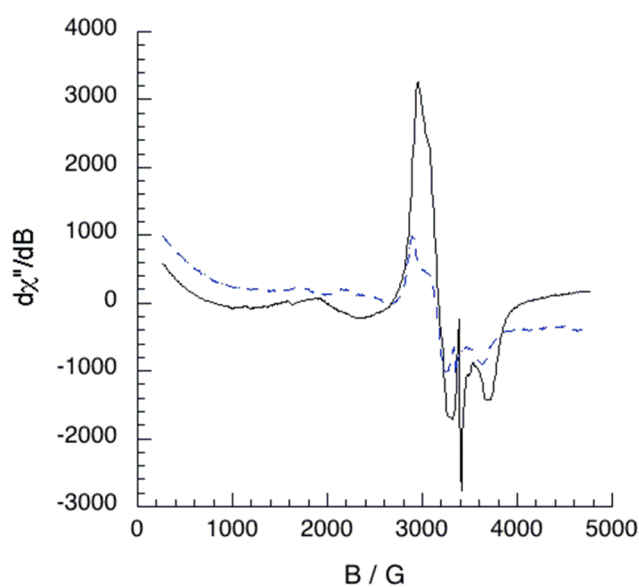


Figure 4.6. EPR spectra (77K) for $\text{P-1}[\text{Ru}(\text{NO})(\text{Cl})]$ (dashed line) and $\text{P-1}[\text{Ru}^{\text{III}}\mathbf{1}(\text{Cl})]$ (solid line).

was suspended in PBS buffer pH 7.2 and irradiated with $\lambda_{\text{max}} = 370$ nm light. Reduced Mb was converted to Mb(NO) within 20 minutes. NO transfer was observed spectroscopically with the shift in the Mb band from $\lambda_{\text{max}} = 435$ to 420 nm (Figure 4.7). The literature reports the same spectral shift for Mb and Mb(NO). This transfer process has a first-order rate constant of $5.0 \times 10^{-4} \text{ s}^{-1}$.

4.3.4. Photorelease of NO The release of NO under physiological conditions was investigated for potential medical applications. A suspension of P-1[Ru(NO)Cl] in PBS buffer pH 7.2 was irradiated with $\lambda_{\text{max}} = \sim 350$ nm light, and aliquots of sample were removed at various time intervals.

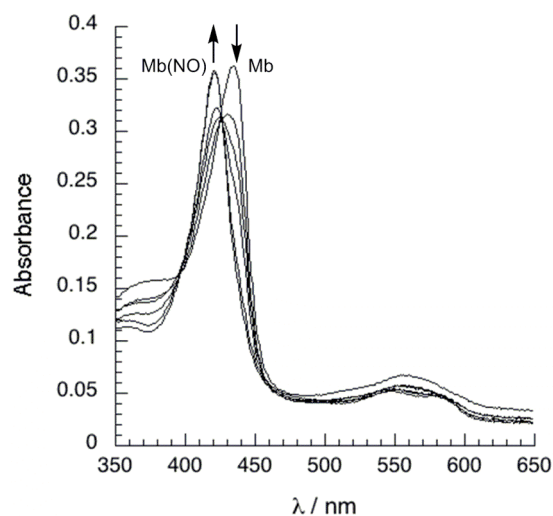


Figure 4.7. Mb peak at 435 nm shifts to 420 nm upon the binding of NO from P-1 [Ru(NO)Cl]. Mb concentration 3.0 mM in 50 mM phosphate buffer, pH 7.2.

Samples of this solution were also collected for time periods in which no irradiation occurred (denoted dark phase). The purpose of the latter experiments was to demonstrate NO release was not observed during the dark phase and thus light was the triggering mechanism for release. Figure 4.8 illustrates the release curve of NO from P-1[Ru(NO)Cl)], showing that 0.027 μmol NO were released after 45 min, corresponding to 2.7 μmol of NO/g of polymer. Figure 4.9 also illustrates the time release with light and

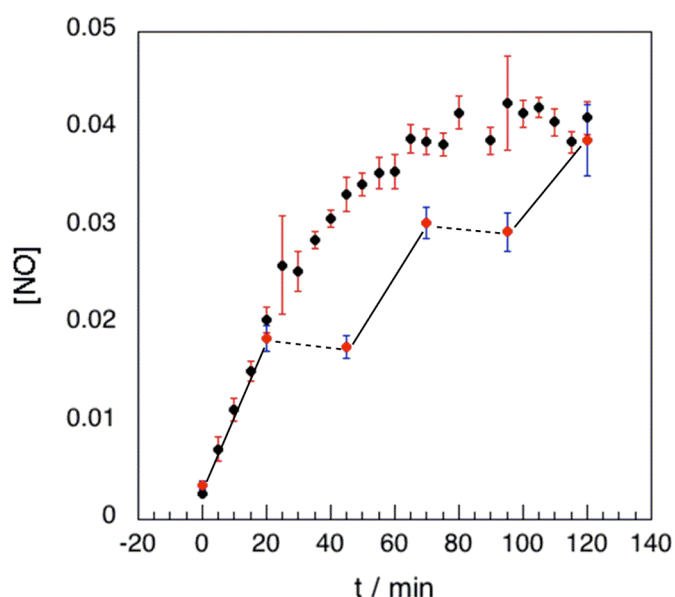


Figure 4.8. Time release curve of P-1[Ru(NO)Cl)] with continuous release (black dots) and stop time release (red dots). Stop time release is demonstrated with continuous irradiation (solid line) and no irradiation (dashed line).

dark phases. The polymer was irradiated with light for 15 min with subsequent 10 min time period with no irradiated. Photolysis proceeded for

another 10 minutes followed by no irradiation for another 10 min. No release of NO was observed during the dark phase, indicating the NO release is controlled by photolysis alone. NO release was monitored indirectly by Griess reaction,^{31,32} which analyzes the nitrite concentration by coupling nitrite to sulfanilamide and NEDA for detection of azo complex at 520 nm (Figure 4.9).

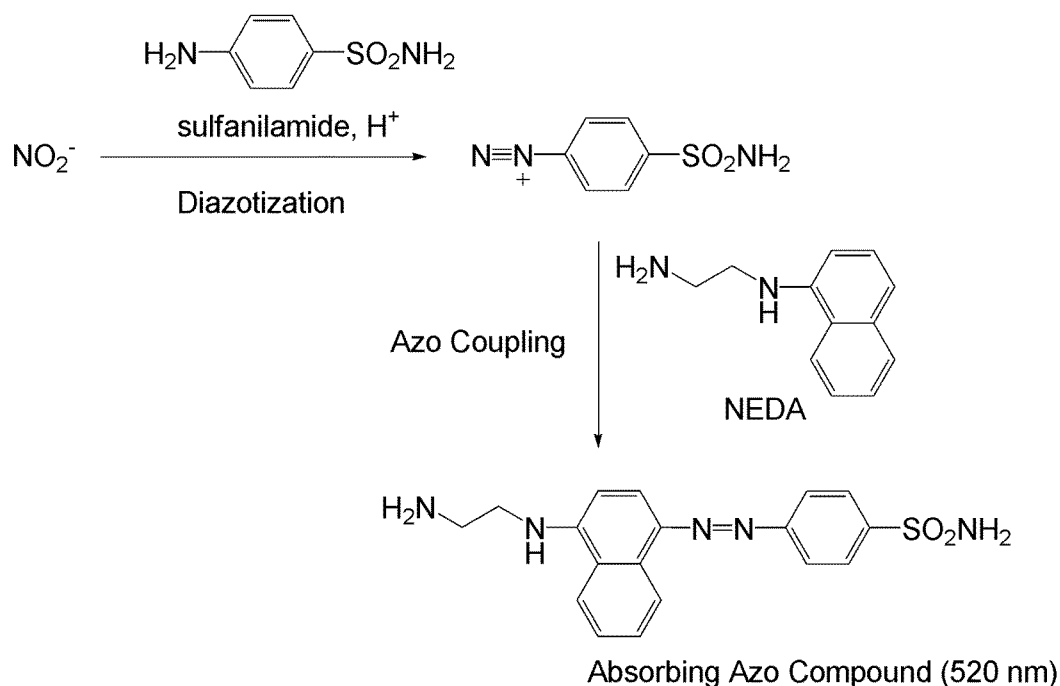


Figure 4.9. Detection of NO through nitrite concentration by the Griess Reaction.

4.4. Conclusion

The chapter described the synthesis and transfer of NO from a porous material. This is the first reported NO donor in polymer material where the release of NO was controlled by light. As described in the introduction, compounds and materials that release NO have been proven to elevate restenosis after angioplasty, inhibit platelet aggregation (thrombus) on implanted medical devices, and relieve hypertension.^{3,4,10,14,16,36,37} NO is involved in numerous processes within the body, thus the release of highly reactive NO would need to be controlled and site specific. P-1[Ru(NO)(Cl)] provides both of these advantages with controlled release of NO with light and site-directed release because NO is attached to the polymer support. This chapter has illustrated the ability of P-1[Ru(NO)(Cl)] to release NO only when it was irradiated with light, and no leaching of NO from the material has been observed. A potential application of this materials is to attach the Ru1(NO)(Cl) complex to a fiber optic to provide release of NO at site specific locations. This could also potentially be useful in cancer treatment, as NO is known to be involved in apoptosis. Materials coated with P-1[Ru(NO)(Cl)] that are implanted in the body, such as stent medical devices, would not prove useful as 380 nm irradiation will not penetrate the skin. Ford and coworkers has developed a complex for the release of NO by single and two photon excitation.³⁸ The near-infrared wavelengths are optimal for tissue transmission. Designing modification to P-1[Ru(NO)(Cl)] for release at single

and two photon excitations would allow the release of NO from the material at desired materials implanted locations with the use of tissue penetrating wavelengths. Medical stents, implanted devices, or other possible areas of atherosclerosis would be coated with this material, and the scheduled release of NO could be performed with one and two photon light excitation.

References

- (1) *Nitric Oxide: Biology and Pathology*; Academic Press: New York, 2000.
- (2) J. Lincoln, C. H. V. H., G. Burnstock *Nitric Oxide in Health and Disease*; Cambridge University Press: New York, 1997.
- (3) Keefer, L. K. *Nature Materials* **2003**, 2, 357-358.
- (4) Keefer, L. K. *Pharm. News* **2000**, 7, 27-32.
- (5) Keefer Larry, K. *Annu. Rev. Pharmacol. Toxicol.* **2003**, 43, 585-607.
- (6) *Nitric oxide in the nervous system*; Academic Press: London, 1995.
- (7) Fung, H. L.; Bauer, J. A. *Cardiovasc. Drugs. Ther.* **1994**, 8, 489-99.
- (8) Wink, D. A.; Cook, J. A.; Pacelli, R.; DeGraff, W.; Gamson, J.; Liebmann, J.; Krishna, M. C.; Mitchell, J. B. *Arch. of Biochem. Biophys.* **1996**, 331, 241-248.
- (9) Schonafinger, K. *Farmaco.* **1999**, 54, 316-320.
- (10) Keefer, L. K. *Annual Review of Pharmacology and Toxicology* **2003**, 43, 585-607, 2 plates.
- (11) Saavedra, J. E.; Southan, G. J.; Davies, K. M.; Lundell, A.; Markou, C.; Hanson, S. R.; Adrie, C.; Hurford, W. E.; Zapol, W. M.; Keefer, L. K. *J Med Chem FIELD Full Journal Title:Journal of medicinal chemistry* **1996**, 39, 4361-5.
- (12) Davies, K. M.; Wink, D. A.; Saavedra, J. E.; Keefer, L. K. *J. Am. Chem. Soc.* **2001**, 123, 5473-81.
- (13) Inami, K.; Nims, R. W.; Srinivasan, A.; Citro, M. L.; Saavedra, J. E.; Cederbaum, A. I.; Keefer, L. K. *Nitric Oxide* **2006**, 14, 309-315.
- (14) Kaul, S.; Cercek, B.; Rengstrom, J.; Xu, X. P.; Molloy, M. D.; Dimayuga, P.; Parikh, A. K.; Fishbein, M. C.; Nilsson, J.; Rajavashisth, T. B.; Shah, P. K. *J. Am. Coll. Cardiol.* **2000**, 35, 493-501.
- (15) Vural, K. M.; Bayazit, M. *Eur. J. Vasc. Endovasc. Surg.* **2001**, 22, 285-93.
- (16) Smith, D. J.; Chakravarthy, D.; Pulfer, S.; Simmons, M. L.; Hrabie, J. A.; Citro, M. L.; Saavedra, J. E.; Davies, K. M.; Hutsell, T. C.; Mooradian, D. L.; Hanson, S. R.; Keefer, L. K. *J. Med. Chem.* **1996**, 39, 1148-56.
- (17) Zhang, H.; Annich, G. M.; Miskulin, J.; Osterholzer, K.; Merz, S. I.; Bartlett, R. H.; Meyerhoff, M. E. *Biomaterials* **2002**, 23, 1485-1494.
- (18) Fukumura, D.; Kashiwagi, S.; Jain, R. K. *Nat. Rev. Cancer* **2006**, 6, 521-534.
- (19) Mitchell, J. B.; Wink, D. A.; DeGraff, W.; Gamson, J.; Keefer, L. K.; Krishna, M. C. *Cancer. Res.* **1993**, 53, 5845-8.

- (20) Ford, P. C.; Bourassa, J.; Lee, B.; Lorkovic, I.; Miranda, K.; Laverman, L. *Coord. Chem. Rev.* **1998**, *171*, 185-202.
- (21) Padden, K. M.; Krebs, J. F.; MacBeth, C. E.; Scarrow, R. C.; Borovik, A. S. *J. Am. Chem. Soc.* **2001**, *123*, 1072-1079.
- (22) Padden, K. M.; Krebs, J. F.; Trafford, K. T.; Yap, G. P. A.; Rheingold, A. H.; Borovik, A. S.; Scarrow, R. C. *Chem. Mater.* **2001**, *13*, 4305-4313.
- (23) Sharma, A. C.; Borovik, A. S. *J. Am. Chem. Soc.* **2000**, *122*, 8946-8955.
- (24) Lu, Y.; Valentine, J. S. *Curr. Opin. Struct. Biol.* **1997**, *7*, 495-500.
- (25) Regan, L. *Trends Biochem. Sci* **1995**, *20*, 280-5.
- (26) Armstrong, W. H., Metal Clusters in Proteins, ACS Symposium Series 372.
- (27) Works, C. F.; Ford, P. C. *J. Am. Chem. Soc.* **2000**, *122*, 7592-7593.
- (28) Krebs, J. F.; Borovik, A. S. *Chem. Comm.* **1998**, 553-554.
- (29) Muller, J. G.; Takeuchi, K. J. *Inorg. Chem.* **1990**, *29*, 2185-8.
- (30) Works, C. F.; Jocher, C. J.; Bart, G. D.; Bu, X.; Ford, P. C. *Inorg. Chem.* **2002**, *41*, 3728-3739.
- (31) Ignarro, L. J.; Fukuto, J. M.; Griscavage, J. M.; Rogers, N. E.; Byrns, R. E. *Proc. Natl Acad Sci. USA* **1993**, *90*, 8103-7.
- (32) H. H. W. Schmidt, M. K. *Methods in Nitric Oxide Research*; Wiley & Sons: New York, 1996.
- (33) Mitchell-Koch, J. T.; Reed, T. M.; Borovik, A. S. *Angew. Chem. Int. Ed.* **2004**, *43*, 2806-2809.
- (34) Moller, J. K. S.; Skibsted, L. H. *Chem. Rev.* **2002**, *102*, 1167-1178.
- (35) Garry, D. J.; Ordway, G. A.; Lorenz, J. N.; Radford, N. B.; Chin, E. R.; Grange, R. W.; Bassel-Duby, R.; Williams, R. S. *Nature* **1998**, *395*, 905-8.
- (36) Chakrapani, H.; Showalter, B. M.; Kong, L.; Keefer, L. K.; Saavedra, J. E. *Org. Lett.* **2007**, *9*, 3409-3412.
- (37) DeRosa, F.; Kibbe, M. R.; Najjar, S. F.; Citro, M. L.; Keefer, L. K.; Hrabie, J. A. *J. Am. Chem. Soc.* **2007**, *129*, 3786-3787.
- (38) Ford, P. C. *Acc. Chem. Res.* **2008**, *41*, 190-200.

Conclusion

The expression system of rHADH has been optimized and purification procedure yields ~ 20 mg/L of >99% pure, fully flavinylated protein. The physical properties (molecular weight and sequence analysis) are in good agreement with the native enzyme. The kinetic properties (specific activity, K_m) of rHADH are also in good agreement with the native enzyme. The recombinant system of HADH behaves identical as native expression. Crystal conditions of rHADH were optimized with screening conditions: 2.0 M $(\text{NH}_4)_2\text{SO}_4$, 0.1 M Hepes, pH 7.5, 2% PEG, 4% glycerol. Addition of glycerol was needed for proper cryofreezing of the crystal. The crystal structure of HADH was defined to 2.7 Å with data collection obtained at the SSRL. The structure validated the presence of 6-S-Cys-FMN and [4Fe-4S] redox active cofactors. The presence of a bound ADP was also determined, but the function of this prosthetic group is unknown. Continual refinement of the 6-S-Cys-FMN suggested the presence of a bend in the isoalloxazine ring, which modulates its redox potential. Docking studies of histamine demonstrate interactions of Glu79 and Asp358 with the protonated amino group of histamine. The imidazole ring of histamine is stabilized by π - π interaction of Tyr181 and Phe77. Asn115 as provides hydrogen bonding to the nitrogen on the imidazole ring. The binding motif demonstrated by the model is found in other histamine binding proteins. Histamine transferase and histamine

binding proteins show a carboxylate residue stabilizing the amino group and π - π interaction of either Phe or Tyr holding the imidazole group. The binding motif of HADH is also similar to the human histamine receptor. This could provide further understanding of the human histamine receptor along with potential drug design.

Continued studies and mutant HADH studies would provide further understanding of this enzyme. Arg230 is believed to stabilize intermediates in the biogenesis of the 6-S-Cys-FMN. Mutations to R230V to observe the formation of 6-S-Cys-FMN could confirm the role of Arginine in the 6-S-Cys-FMN biogenesis. Further probing of the redox active [4Fe-4S] and discovery the physiological external electron acceptor would provide understanding of electron transport of the 6-S-Cys-FMN to outside the enzyme. The implications of understanding the electron pathway would be useful in the design of histamine biosensor.

The synthesis of the two agents of the iron-chelating phenanthroline inhibitor was coupled to a retention signal (KDEL) to target the endoplasmic reticulum to inhibitor prollyl 4-hydroxylase. Colocalization studies of the fluorophore labeled phen-2-KDEL inhibitor with ER tracker demonstrated that the inhibitor is localized in the ER. Good collocation (85%) and overlap (94%) were shown with the fluorophore and the ER tracker. Phen-2-GKDEL demonstrates an IC_{50} value of 3.8 mM against isolated human P4H. This value is around 100-fold increase in IC_{50} value as compared to phen without

the KDEL tag. The peptide chain at the 2 position next to the iron chelation, could be affecting the ability of the phenanthroline to chelate to the metal. Synthesis of the KDEL at the 5 position could elevate this and provide better iron chelation. Similarities in IC_{50} for phen-2-GKDEL (165 μ M) and phen (160 μ M) were observed in HFF cells. Experimental evidence suggests that phen-2-GKDEL and phen are demonstrating similar potency in HFF cells. The optimal design of a potent inhibitor with the KDEL tag would provide efficient selectivity and inhibition of P4H

The controlled release of nitric oxide by P-1[Ru(NO)(Cl)] was designed with a porous material. Slight isolated ruthenium salen complex allowed for the storage and photolytic release of nitric oxide. Release of nitric oxide was demonstrated spectroscopically by EPR. The bound Ru(NO) complex demonstrates a slight EPR sign, but upon release of NO, the electron on the Ru^{III} complex is observed at $g = 2.0$. The transfer NO to biologically relevant myoglobin within 20 minutes was observed with a spectroscopic shift of the unbound Mb (435 nm) to the Mb(NO) form (420). The controlled release of NO from the porous material was also shown. No is released from this material in the presence of light; however, during periods of darkness, the release of NO was not observed. This is the first system where NO is photoreleased from an immobilized polymer support. Continued design of Ru salen complex covalently linked to a fiber optic would provide the site specific delivery of nitric oxide to a desired location. The release of NO by

two photon excitation from the polymer material could provide penetration wavelengths through tissues for the release of NO.

Appendix

Soluble collagen secreted in the media was also assayed by varying the concentration of phen-2-GKDEL from 0.01 μM to 100 μM in a dose dependent experiment. Based on the pervious experiment, the media was diluted to a concentration of 20 % binding buffer and 80 % media, as these condition provided the highest absorbance. Figure A.1 exhibits the curve for phen-2-GKDEL suggesting a dose dependence manner for this inhibitor.

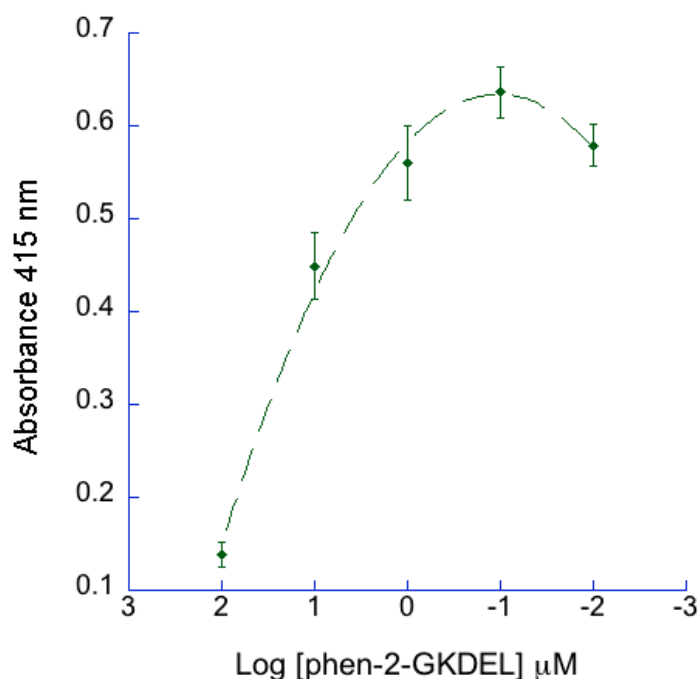


Figure A.1. Dosage dependent indirect ELISA detecting collagen production with a concentration range of 100 mM to 0.01 mM in the presence of phen (blue circles) and in the presence of phen-GKDEL (green diamonds)

Phen and phen-2-GKDEL were both assayed for secreted soluble collagen by varying the concentration of each inhibitor from 0.01 μM to 100 μM in a dose dependent experiment. The media was diluted to a concentration of 20 % binding buffer and 80 % media, as these condition provided the highest absorbance in previous experiments. Figure A.2 exhibits the curve for each inhibitor, suggesting a similar dose dependence value for both of these inhibitors. These results show that both phen and phen-2-GKDEL are inhibiting collagen production with the similar dose dependence.

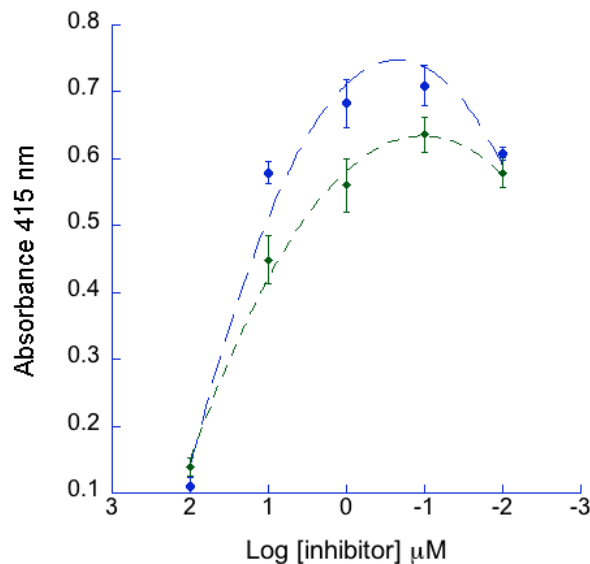


Figure A.2. Dosage dependent indirect ELISA of collagen production with a concentration range of 100 mM to 0.01 mM for phen (blue circles) and phen-2-GKDEL (green diamonds)

A dose dependent behaviour for the inhibition of collagen production was also performed with phen-2-GKDEL. At lower concentration of inhibitor the inhibition of collagen production was observed as very minimal, but at higher concentration of inhibitor the collagen production was substantially inhibited. The dose dependent curve exhibits a lower absorbance at 0.01 μM as compared to 0.1 μM , which is not expected. This could be an artefact of the ELISA. At the outer edge of the plate the heat transfer of the outer samples is not the same as the samples within the middle of the ELISA. This conclusion may be validated as both samples were at the out edge and exhibited an unusual decline in absorbance. Indirect ELISA assayed soluble collagen secreted in the media and demonstrated inhibition is a dose dependent behaviour.